A Continuum Constitutive Model for Amorphous Metallic Materials

by

Cheng Su

Submitted to the Department of Mechanical Engineering
in partial fulfillment of the requirements for the degree of

Doctor of Philosophy

at the

MASSACHUSETTS INSTITUTE OF TECHNOLOGY

February 2007

Author .....
Department of Mechanical Engineering
October 13, 2006

Certified by .....
Lallit Anand
Professor of Mechanical Engineering
Thesis Supervisor

Accepted by .....
Lallit Anand
Chairman, Department Committee on Graduate Students

A Continuum Constitutive Model for Amorphous Metallic Materials

by

Cheng Su

Submitted to the Department of Mechanical Engineering
on October 13, 2006, in partial fulfillment of the
requirements for the degree of
Doctor of Philosophy

Abstract

A finite-deformation, Coulomb-Mohr type constitutive theory for the elastic-viscoplastic response of pressure-sensitive and plastically-dilatant isotropic materials has been developed. The constitutive model has been implemented in a finite element program, and the numerical capability is used to study the deformation response of amorphous metallic glasses. Specifically, the response of an amorphous metallic glass in tension, compression, strip-bending, and indentation is studied, and it is shown that results from the numerical simulations qualitatively capture major features of corresponding results from physical experiments available in the literature.

The response of a Zr-based glass in instrumented plane strain indentation with a cylindrical indenter tip is also studied experimentally. The constitutive model and simulation capability is used to numerically calculate the indentation load versus depth curves, and the evolution of corresponding shear-band patterns under the indenter. The numerical simulations are shown to compare very favorably with the corresponding experimental results.

The constitutive model is subsequently extended to the high homologous temperature regime, and the response of a representative Pd-based metallic glass in tension at various strain rates and temperatures with different pre-annealing histories is studied. The model is shown to capture the major features of the stress-strain response and free volume evolution of this metallic glass. In particular, the phenomena of stress overshoot and strain softening in monotonic experiments at a given strain rate and temperature, as well as strain rate history effects in experiments involving strain rate increments and decrements are shown to be nicely reproduced by the model.

Finally, a cavitation mechanism is incorporated in the constitutive model to simulate the failure phenomenon caused by the principal and hydro-static stresses. With the revised theory, the response of a prototypical amorphous grain-boundary is investigated, and the result is later applied to study the deformation and failure behavior of nanocrystalline fcc metals by coupling with appropriate crystal-plasticity constitutive model to represent the grain interior.

Thesis Supervisor: Lallit Anand
Title: Professor of Mechanical Engineering

Acknowledgments

First and foremost, I would like to express my sincere gratitude to Professor Lallit Anand for his support and guidance over the last six years. His demand of impeccable standards and fastidiousness for detail will continue to inspire me. I would also like to thank Professor Mary Boyce, Professor Christopher Schuh, and Professor Subra Suresh for serving on my thesis committee.

To the Mechanics and Materials group i.e. Jin Yi, Yu Qiao, Hang Qi, Nicoli Ames, Regina Huang, Christopher Gething, Suvrat Lele, Nuo Sheng, Yin Yuan, Theodora Tzianetopoulou, Rajdeep Sharma, Ethan Parsons and others, and to my lunch group, Yuetao Zhang, Yong Li, Gang Tan, Ronggui Yang, thank you very much for all the great time we have had. I wish all of you the best luck in your future endeavors.

To Ray Hardin and Leslie Regan, thank you very much for taking care of all the administrative details and providing me with your unerring advice.

To Yujie Wei, my colleague and most of all buddy for the last five years, thank you very much for all that you have done for me.

To Meimei, my kind and caring girlfriend, thank you very much for bringing me so much sweet memories and constantly encouraging me.

To my parents and my sister, thank you very much for your boundless love.

The financial support for this work was provided by the ONR Contract N00014-01-1-0808 with MIT.

Contents

List of Figures

Chapter 1

Introduction

This project focuses on modelling the finite deformation and failure behavior of amorphous metallic materials. Amorphous metals is of immense fundamental scientific and technical interest at the present time.

Under slow to moderate cooling rates most metallic materials solidify in a polycrystalline form; however, under high cooling rates, certain metallic alloys solidify in a disordered form, and such disordered metals are referred to as *amorphous metals* or *metallic glasses*; they are metastable liquids that cannot find their equilibrium crystalline state. The first amorphous Au-Si metallic glass was developed in thin ribbon form using a very high cooling rate of $\approx 10^5 - 10^6$ K/s by Klement et al. (1960), but by the late 1980s and early 1990s it was discovered that metallic glasses could be processed at relatively slow cooling rates ($1 - 100$ K/s) in *bulk* form in certain multicomponent alloy systems due to sluggish crystallization kinetics (e.g., Inoue, 2000; Johnson, 1999, 2002). The current generation of bulk metallic glasses is believed to have many potential applications resulting from their unique properties: superior tensile strength ($\approx 2.0\,\mathrm{GPa}$), high yield strain ($\approx$2%), relatively high fracture toughness $\approx 15 - 25\,\mathrm{MPa}\sqrt{\mathrm{m}}$, and good corrosion resistance.

When a metallic glass is deformed at ambient temperatures, well below its glass transition temperature, its inelastic deformation is characterized by strain-softening which results in the formation of intense localized shear bands; fracture typically occurs after very small inelastic strain in tension, but substantial inelastic strain levels

can be achieved under states of confined compression, such as in indentation experiments (cf., e.g., Argon, 1979, 1993; Spaepen, 1977; Donovan, 1988, 1989; Hays et al., 2000; Vaidyanathan et al., 2001; Mukai et al., 2002). The micro-mechanisms of inelastic deformation in bulk metallic glasses are not related to dislocation-based mechanisms that characterize the plastic deformation of crystalline metals. The plastic deformation of amorphous metallic glasses is fundamentally different from that in crystalline solids because of the lack of long-range order in the atomic structure of these materials. The computer simulations of Argon and co-workers (cf., e.g., Deng et al., 1989; Argon, 1993) show that at a micromechanical level inelastic deformation in metallic glasses occurs by local shear transformations in clusters of atoms ($\approx$ 30 to 50 atoms), and topologically such shear transformations require a local inelastic *dilatation* that produces an elastic strain field in the surrounding material, that auto-catalytically then initiates similar shear transformations in neighboring volume elements, leading to the formation of shear bands.

An important consequence of the micro-mechanism of inelastic deformation in amorphous metals is that at the macroscopic level, experimentally-determined yield criteria for inelastic deformation are found not to obey the classical pressure-insensitive Mises or Tresca forms, but show a strong pressure sensitivity of plastic flow (cf., e.g., Donovan, 1988, 1989; Bruck et al., 1993; Lewandowski and Lowhaphandu, 2002). Although the experimental studies mentioned above all suggest a failure of the applicability of the classical Mises or Tresca yield criteria for metallic glasses, they do not conclusively identify the form of the pressure-sensitivity. Recently, Lund and Schuh (2003) have reported on their molecular-dynamic simulations of multiaxial deformation in a model metallic glass. They found that there was a pronounced asymmetry between the magnitudes of the yield strengths in tension and compression. By exploring a variety of biaxial stress states, they numerically probed a plane-stress yield surface for their model metallic glass and found that it was not well-described by traditional pressure-insensitive yield criteria. However, the pressure-sensitive Coulomb-Mohr yield criterion was found to describe the data from their numerical simulations quite well.

The Coulomb-Mohr yield condition is widely used in soil mechanics to determine

the stress required for flow of a granular material; however, the *flow rule*, that is, the equation which governs the flow behavior for this class of materials, is generally not agreed upon. An attractive *two-dimensional* (plane-strain) *rate-independent* flow rule for Coulomb-Mohr materials is the "double-shearing" flow rule (e.g., Spencer, 1964, 1982; Mehrabadi and Cowin, 1978; Nemat-Nasser et al., 1981; Anand, 1983). Recently, Anand and Gu (2000) have generalized this model to three-dimensions; their model includes the effects of elastic deformation, and the typical pressure-sensitive and dilatant, hardening/softening response observed in granular materials.

In Chapter 2 we further generalize the rate-independent elastic-plastic constitutive model of Anand and Gu (2000) to formulate a *thermodynamically consistent*, finite-deformation macroscopic theory for the *rate-dependent* elastic-viscoplastic deformation of pressure-sensitive, and plastically-dilatant materials, and apply it to model the deformation of amorphous metallic glasses under isothermal conditions.

We have implemented our new constitutive model in the finite element program ABAQUS/Explicit (2004) by writing a user material subroutine. Using this numerical implementation of our model, in Chapter 3 we study the response of a metallic glass in tension, compression, strip bending, and indentation, and show that results from our numerical simulations capture major features of corresponding results from physical experiments available in the literature (Anand and Su, 2005).

In Chapter 4 we report our own plane strain indentation experiments on a Zr-based bulk metallic glass. We have measured the corresponding macroscopic load (P) versus indentation depth (h) curves, and studied the evolution of the shear band patterns under the indenter. We shall show that the constitutive model and numerical simulation capability developed previously is capable of producing simulations that *quantitatively* compare very favorably against the corresponding experimental results (Su and Anand, 2006).

The relative low ductility of metallic glasses at ambient temperature makes it difficult to efficiently machine metallic glass raw materials into complex shapes at the ambient temperature. However, like silica glasses, metallic glasses have low viscosities at higher homologous temperatures. Also they can endure a significant amount of plastic strain without failure at this temperature regime. Therefore it is easier to

forge a metallic glass into desirable shapes at high temperatures. We envision precision forging/embossing will be an important process in manufacturing metallic glass components for applications requiring feature size in the micron range. To make this process more time and cost efficient it is necessary to understand and to be able to simulate the response of a metallic glass at high homologous temperatures.

In Chapter 5 we extend the model developed in Chapter 2 to the high homologous temperature regime and use the numerical capability to study the response of a representative Pd-based metallic glass. Specifically, the response of metallic glass $Pd_{40}Ni_{40}P_{20}$ in tension at various strain rates and temperatures with different pre-annealing histories is studied. It is shown that results from the numerical simulations compare favorably against corresponding experimental results. The response of this representative metallic glass in a few possible manufacturing processes such as strip bending, indentation and forging is also simulated, which shows the potential capability of this constitutive model in facilitating the design and manufacture of metallic glass components

It is well known that in polycrystalline metals, a substantial increase in strength and hardness can be obtained by reducing the grain size to the nanometer scale (cf., e.g., Gleiter, 1989; Suryanarayana, 1995; McFadden et al., 1999; Jeong et al., 2001; Schuh et al., 2002; Lu et al., 2000). These attributes have generated considerable interest in the use of nanocrystalline (nc) metallic materials (grain sizes less than $\approx$ 100 nm), for a wide variety of structural applications. The hardness, stiffness, strength and ductility of some nc-fcc metals (e.g., Cu, Ni), as measured by microindentation and simple tension experiments, have been reported in the recent literature (e.g., Nieman et al., 1991; Sanders et al., 1997; Ebrahami et al., 1998, 1999; Legros et al., 2000; Lu et al., 2001; Torre et al., 2002).

Both physical experiments and atomistic simulations show that for nanocrystalline materials, plasticity induced by dislocation motion inside the grain interiors becomes less significant, whereas separation and sliding of grain boundaries starts to play an important role in the overall inelastic deformation and failure response of these materials (Kumar et al., 2003).

Motivated by the fact that amorphous metals are the ultimate limit for nanocrys-

talline metals, as the crystal grain size decreases to zero, in Chapter 6 we extend our amorphous constitutive theory by adding in a cavitation mechanism to model the failure phenomenon caused by the principal and hydro-static stresses. With the revised theory we studied the response of a prototypical amorphous grain-boundary. Coupled with appropriate crystal-plasticity constitutive model to represent the grain interior, the result obtained in this chapter is applied to study the deformation and failure behavior of nanocrystalline fcc metals (Wei, Su, and Anand, 2006).

Chapter 2

A theory for amorphous viscoplastic materials undergoing finite deformations

2.1 Kinematics

With minor modifications for plastic compressibility, the development of the theory in §2.1–§2.4 closely follows the work of Gurtin (2002) and Anand and Gurtin (2003).

2.1.1 Basic kinematics

We consider a homogeneous body $\mathrm{B_R}$ identified with the region of space it occupies in a fixed *reference configuration*, and denote by $\mathbf{X}$ an arbitrary material point of $\mathrm{B_R}$. A *motion* of $\mathrm{B_R}$ is then a smooth one-to-one mapping $\mathbf{x} = \mathbf{y}(\mathbf{X}, t)$ with *deformation gradient*, *velocity*, and *velocity gradient* given by[1]

$$\mathbf{F} = \nabla \mathbf{y}, \qquad \mathbf{v} = \dot{\mathbf{y}}, \qquad \mathbf{L} = \operatorname{grad} \mathbf{v} = \dot{\mathbf{F}}\mathbf{F}^{-1}. \tag{2.1}$$

[1] *Notation*: ∇ and Div denote the gradient and divergence with respect to the material point $\mathbf{X}$ in the *reference configuration*; grad and div denote these operators with respect to the point $\mathbf{x}$ in the deformed configuration; a superposed dot denotes the material time-derivative. Throughout, we write $\mathbf{F}^{e-1} = (\mathbf{F}^e)^{-1}$, $\mathbf{F}^{p-\top} = (\mathbf{F}^p)^{-\top}$, etc. We write $\operatorname{tr}\mathbf{A}$, $\operatorname{sym}\mathbf{A}$, $\operatorname{skw}\mathbf{A}$, $\mathbf{A}_0$, and $\operatorname{sym}_0\mathbf{A}$ respectively, for the trace, symmetric, skew, deviatoric, and symmetric-deviatoric parts of a tensor $\mathbf{A}$. Also, the inner product of tensors $\mathbf{A}$ and $\mathbf{B}$ is denoted by $\mathbf{A} \cdot \mathbf{B}$, and the magnitude of $\mathbf{A}$ by $|\mathbf{A}| = \sqrt{\mathbf{A} \cdot \mathbf{A}}$.

We base our theory on the Kröner (1960)-Lee (1969) decomposition

$$\mathbf{F} = \mathbf{F}^e\mathbf{F}^p. \tag{2.2}$$

Here, suppressing the argument t:

- $\mathbf{F}^p(\mathbf{X})$ represents a *local* plastic deformation of the *material* at $\mathbf{X}$ due to "plastic mechanisms" such as the cumulative effects of inelastic transformations resulting from the cooperative action of atomic clusters in metallic glasses in a microscopic neighborhood of $\mathbf{X}$; this local deformation carries the material into — and ultimately "pins" the material to — a *coherent structure* that resides in the *relaxed space* at $\mathbf{X}$ (as represented by the range of $\mathbf{F}^p(\mathbf{X})$);

- $\mathbf{F}^e(\mathbf{X})$ represents the subsequent stretching and rotation of this coherent structure, and thereby represents the "elastic mechanisms" such as stretching and rotation of the interatomic structure in metallic glasses.

We refer to $\mathbf{F}^p$ and $\mathbf{F}^e$ as the *plastic and elastic parts* of $\mathbf{F}$.

By $(2.1)_3$ and (2.2),

$$\mathbf{L} = \mathbf{L}^e + \mathbf{F}^e\mathbf{L}^p\mathbf{F}^{e-1}, \tag{2.3}$$

with

$$\mathbf{L}^e = \dot{\mathbf{F}}^e\mathbf{F}^{e-1}, \qquad \mathbf{L}^p = \dot{\mathbf{F}}^p\mathbf{F}^{p-1}. \tag{2.4}$$

As is standard, we define the elastic and plastic stretching and spin tensors through

$$\left.\begin{aligned} \mathbf{D}^e &= \mathrm{sym}\mathbf{L}^e, \qquad \mathbf{W}^e = \mathrm{skw}\mathbf{L}^e, \\ \mathbf{D}^p &= \mathrm{sym}\mathbf{L}^p, \qquad \mathbf{W}^p = \mathrm{skw}\mathbf{L}^p, \end{aligned}\right\} \tag{2.5}$$

so that $\mathbf{L}^e = \mathbf{D}^e + \mathbf{W}^e$ and $\mathbf{L}^p = \mathbf{D}^p + \mathbf{W}^p$.

With the use of (2.1), equation (2.3) may be written as

$$\mathrm{grad}\,\mathbf{v} = \mathbf{L}^e + \mathbf{F}^e\,\mathbf{L}^p\,\mathbf{F}^{e-1}. \tag{2.6}$$

The right polar decomposition of $\mathbf{F}^e$ is given by

$$\mathbf{F}^e = \mathbf{R}^e \mathbf{U}^e, \tag{2.7}$$

where $\mathbf{R}^e$ is a rotation, while $\mathbf{U}^e$ is a symmetric, positive-definite tensor with

$$\mathbf{U}^e = \sqrt{\mathbf{F}^{e\top} \mathbf{F}^e}. \tag{2.8}$$

Also, the right elastic Cauchy-Green strain tensor is given by

$$\mathbf{C}^e = \mathbf{U}^{e2} = \mathbf{F}^{e\top} \mathbf{F}^e. \tag{2.9}$$

We write

$$J \stackrel{\text{def}}{=} \det \mathbf{F}, \tag{2.10}$$

and hence, using (2.2),

$$J = J^e J^p, \qquad \text{where} \qquad J^e \stackrel{\text{def}}{=} \det \mathbf{F}^e, \qquad \text{and} \qquad J^p \stackrel{\text{def}}{=} \det \mathbf{F}^p. \tag{2.11}$$

We refer to

$$\operatorname{tr} \mathbf{L}^p = \operatorname{tr} \mathbf{D}^p \quad \text{as the } \textit{plastic dilatation-rate},$$

and note that

$$\dot{J}^p = J^p \operatorname{tr} \mathbf{L}^p. \tag{2.12}$$

For later use, we define the *plastic volumetric strain* by

$$\eta \stackrel{\text{def}}{=} \ln J^p; \tag{2.13}$$

then

$$\dot{\eta} = \operatorname{tr} \mathbf{L}^p. \tag{2.14}$$

2.1.2 Frame-indifference

Changes in frame (observer) are smooth time-dependent rigid transformations of the Euclidean space through which the body moves. We require that the theory be invariant under such transformations, and hence under transformations of the form

$$\mathbf{y}(\mathbf{X},t) \to \mathbf{Q}(t)\mathbf{y}(\mathbf{X},t) + \mathbf{q}(t) \tag{2.15}$$

with $\mathbf{Q}(t)$ a rotation (proper-orthogonal tensor) and $\mathbf{q}(t)$ a vector at each t. Then, under a change in observer, the deformation gradient transforms according to

$$\mathbf{F} \to \mathbf{QF}. \tag{2.16}$$

Thus, $\dot{\mathbf{F}} \to \mathbf{Q}\dot{\mathbf{F}} + \dot{\mathbf{Q}}\mathbf{F}$, and by $(2.1)_3$,

$$\mathbf{L} \to \mathbf{QLQ}^\top + \dot{\mathbf{Q}}\mathbf{Q}^\top. \tag{2.17}$$

Moreover, $\mathbf{F}^e\mathbf{F}^p \to \mathbf{QF}^e\mathbf{F}^p$, and hence since *observers view only the deformed configurations*[2]

$$\mathbf{F}^e \to \mathbf{QF}^e, \qquad \text{and} \qquad \mathbf{F}^p \text{ is invariant,} \tag{2.18}$$

and, by $(2.4)_2$

$$\mathbf{L}^p \text{ is invariant.} \tag{2.19}$$

Also, by $(2.4)_1$, $\mathbf{L}^e \to \mathbf{QL}^e\mathbf{Q}^\top + \dot{\mathbf{Q}}\mathbf{Q}^\top$ and hence

$$\mathbf{D}^e \to \mathbf{QD}^e\mathbf{Q}^\top, \qquad \mathbf{W}^e \to \mathbf{QW}^e\mathbf{Q}^\top + \dot{\mathbf{Q}}\mathbf{Q}^\top. \tag{2.20}$$

Further, by (2.7),

$$\mathbf{QF}^e \to \mathbf{QR}^e\mathbf{U}^e = \mathbf{QV}^e\mathbf{Q}^\top\mathbf{QR}^e,$$

[2]That is, the reference configuration and relaxed spaces are independent of the choice of such changes in frame.

and we may conclude from the uniqueness of the polar decomposition that

$$\mathbf{R}^e \to \mathbf{Q}\mathbf{R}^e, \qquad \mathbf{V}^e \to \mathbf{Q}\mathbf{V}^e\mathbf{Q}^\top, \qquad \mathbf{U}^e \text{ is invariant.} \tag{2.21}$$

2.2 Internal and external expenditures of power

We write $B(t) = \mathbf{y}(\mathrm{B_R}, t)$ for the *deformed body*. We use the term *part* to denote an arbitrary time-dependent subregion $P(t)$ of $B(t)$ that *deforms* with the body, so that

$$P(t) = \mathbf{y}(\mathrm{P_R}, t) \tag{2.22}$$

for some *fixed* subregion $\mathrm{P_R}$ of $\mathrm{B_R}$. The outward unit normal on the boundary ∂P of P is denoted by $\mathbf{n}$.

We assume that power is expended internally by a *stress* $\mathbf{T}$ power-conjugate to $\mathbf{L}^e$, and a *microstress* $\mathbf{T}^p$ power-conjugate to $\mathbf{L}^p$, and we write the *internal power* as

$$\mathcal{W}_{\text{int}}(P) = \int_P \left(\mathbf{T}\cdot\mathbf{L}^e + J^{e-1}\mathbf{T}^p\cdot\mathbf{L}^p\right) dv. \tag{2.23}$$

Here $\mathbf{T}$ and $\mathbf{T}^p$ are defined over the body for all time. The term J^{e-1} arises because $\mathbf{T}^p\cdot\mathbf{L}^p$ is measured per unit volume in the relaxed space, but the integration is carried out within the deformed body.

The power expended on P by material or bodies exterior to P results from a *macroscopic surface traction* $\mathbf{t}(\mathbf{n})$, measured per unit area in the deformed configuration, and a *macroscopic body force* $\mathbf{b}$, measured per unit volume in the deformed configuration, each of whose working accompanies the macroscopic motion of the body. The body force $\mathbf{b}$ is assumed to include inertial forces.[3] We therefore write the *external power* as

$$\mathcal{W}_{\text{ext}}(P) = \int_{\partial P} \mathbf{t}(\mathbf{n})\cdot\mathbf{v}\, da + \int_P \mathbf{b}\cdot\mathbf{v}\, dv, \tag{2.24}$$

with $\mathbf{t}(\mathbf{n})$ (for each unit vector $\mathbf{n}$) and $\mathbf{b}$ defined over the body for all time.

[3]Inertial forces result in specific class of external body forces. Granted an inertial frame, inertial body forces have the form $\mathbf{b}_{\text{in}} = -\rho\dot{\mathbf{v}}$, with $\rho(\mathbf{x}, t) > 0$ the mass density in the deformed configuration.

2.2.1 Consequences of frame-indifference

Consider the internal power $\mathcal{W}_{\text{int}}(P)$ under an arbitrary change in frame. In the new frame P transforms rigidly to a region P^*, $\mathbf{T}$ to $\mathbf{T}^*$ and $\mathbf{T}^p$ to $\mathbf{T}^{p*}$. If we transform the integral over P^* to an integral over P and use the transformation laws in §2.1.2, we find that the internal power transforms as

$$\mathcal{W}^*_{\text{int}}(P^*) = \int_P \left\{ \mathbf{T}^* \cdot (\mathbf{Q}\mathbf{L}^e\mathbf{Q}^\top + \dot{\mathbf{Q}}\mathbf{Q}^\top) + J^{e-1}\mathbf{T}^{p*} \cdot \mathbf{L}^p \right\} dv.$$

We require that the internal power be invariant under a change in frame: $\mathcal{W}^*_{\text{int}}(P^*) = \mathcal{W}_{\text{int}}(P)$. Since P is arbitrary, this requirement yields the relation

$$\mathbf{T}^* \cdot (\mathbf{Q}\mathbf{L}^e\mathbf{Q}^\top + \dot{\mathbf{Q}}\mathbf{Q}^\top) + J^{-1}\mathbf{T}^{p*} \cdot \mathbf{L}^p = \mathbf{T} \cdot \mathbf{L}^e + J^{e-1}\mathbf{T}^p \cdot \mathbf{L}^p.$$

Also, since the change in frame is arbitrary, if we choose it such that $\dot{\mathbf{Q}} = \mathbf{0}$, we find that $\mathbf{T}$ and $\mathbf{T}^p$ transform according to

$$\mathbf{T} \to \mathbf{Q}\mathbf{T}\mathbf{Q}^\top, \qquad \mathbf{T}^p \text{ is invariant.} \tag{2.25}$$

On the other hand, if we assume that $\mathbf{Q} = \mathbf{1}$ at the time in question, so that $\dot{\mathbf{Q}}$ is an arbitrary skew tensor, we find that $\mathbf{T} \cdot \dot{\mathbf{Q}} = 0$, and hence $\mathbf{T}$ is symmetric:

$$\mathbf{T} = \mathbf{T}^\top. \tag{2.26}$$

Finally, using the symmetry of $\mathbf{T}$, we may write the internal power as

$$\mathcal{W}_{\text{int}}(P) = \int_P (\mathbf{T} \cdot \mathbf{D}^e + J^{e-1}\mathbf{T}^p \cdot \mathbf{L}^p)\, dv. \tag{2.27}$$

2.3 Principle of virtual power. Macroscopic and microscopic force balances

The theory presented here is based on the belief that the power expended by each independent "rate-like" kinematical descriptor be expressible in terms of an associated

force system consistent with its own balance. But the basic "rate-like" descriptors, namely, $\mathbf{v}$, $\mathbf{L}^e$, and $\mathbf{L}^p$ *are not independent,* as they are constrained by (2.6), and it is not apparent what forms the associated force balances should take. For that reason, we determine these balances using the principal of virtual power.

2.3.1 Principle of virtual power

Assume that, at some arbitrarily chosen but *fixed time*, the fields $\mathbf{y}$, $\mathbf{F}^e$ (and hence $\mathbf{F}$ and $\mathbf{F}^p$) are known, and consider the fields $\mathbf{v}$, $\mathbf{L}^e$, and $\mathbf{L}^p$ as virtual velocities to be specified independently in a manner consistent with (2.6); that is, denoting the virtual fields by $\tilde{\mathbf{v}}$, $\tilde{\mathbf{L}}^e$, and $\tilde{\mathbf{L}}^p$ to differentiate them from fields associated with the actual evolution of the body, we require that

$$\operatorname{grad}\tilde{\mathbf{v}} = \tilde{\mathbf{L}}^e + \mathbf{F}^e\tilde{\mathbf{L}}^p\mathbf{F}^{e-1}. \tag{2.28}$$

More specifically, we define a *generalized virtual velocity* to be a list

$$\mathcal{V} = (\tilde{\mathbf{v}}, \tilde{\mathbf{L}}^e, \tilde{\mathbf{L}}^p),$$

consistent with (2.28).

Writing

$$\left.\begin{aligned} \mathcal{W}_{\text{ext}}(P,\mathcal{V}) &= \int_{\partial P} \mathbf{t}(\mathbf{n})\cdot\tilde{\mathbf{v}}\,da + \int_P \mathbf{b}\cdot\tilde{\mathbf{v}}\,dv, \\ \mathcal{W}_{\text{int}}(P,\mathcal{V}) &= \int_P (\mathbf{T}\cdot\tilde{\mathbf{L}}^e + J^{e-1}\mathbf{T}^p\cdot\tilde{\mathbf{L}}^p)\,dv, \end{aligned}\right\} \tag{2.29}$$

respectively, for the external and internal expenditures of *virtual power*, the *principle of virtual power* is the requirement that the external and internal powers be balanced: given any part P,

$$\mathcal{W}_{\text{ext}}(P,\mathcal{V}) = \mathcal{W}_{\text{int}}(P,\mathcal{V}) \quad \text{for all generalized virtual velocities } \mathcal{V}. \tag{2.30}$$

2.3.2 Macroscopic force and moment balances. Microforce balance

To deduce the consequences of the principle of virtual power, assume that (2.30) is satisfied. In applying the virtual balance (2.30) we are at liberty to choose any $\mathcal{V}$ consistent with the constraint (2.28).

Consider a generalized virtual velocity with $\tilde{\mathbf{L}}^p \equiv \mathbf{0}$, so that $\operatorname{grad} \tilde{\mathbf{v}} = \tilde{\mathbf{L}}^e$. For this choice of $\mathcal{V}$, (2.30) yields

$$\int_{\partial P} \mathbf{t}(\mathbf{n}) \cdot \tilde{\mathbf{v}}\, da + \int_P \mathbf{b} \cdot \tilde{\mathbf{v}}\, dv = \int_P \mathbf{T} \cdot \operatorname{grad} \tilde{\mathbf{v}}\, dv.$$

and, using the divergence theorem,

$$\int_{\partial P} \big(\mathbf{t}(\mathbf{n}) - \mathbf{T}\mathbf{n}\big) \cdot \tilde{\mathbf{v}}\, da + \int_P (\operatorname{div} \mathbf{T} + \mathbf{b}) \cdot \tilde{\mathbf{v}}\, dv = 0.$$

Since this relation must hold for all P and all $\tilde{\mathbf{v}}$, standard variational arguments yield the traction condition

$$\mathbf{t}(\mathbf{n}) = \mathbf{T}\mathbf{n}\,, \tag{2.31}$$

and the local force balance

$$\operatorname{div} \mathbf{T} + \mathbf{b} = \mathbf{0}. \tag{2.32}$$

Therefore, recalling (2.26), the symmetric stress $\mathbf{T}$ plays the role of the *Cauchy stress*, and (2.32) and (2.26) represent the *macroscopic force and moment balances.*

To discuss the microscopic counterparts of these results, we next choose $\tilde{\mathbf{v}} \equiv \mathbf{0}$. Then the external power vanishes identically, so that, by (2.30), the internal power must also vanish. Moreover, by (2.28), $\tilde{\mathbf{L}}^e = -\mathbf{F}^e \tilde{\mathbf{L}}^p \mathbf{F}^{e-1}$, and hence

$$\int_{\mathrm{P}} J^{e-1} \Big(\mathbf{T}^p - J^e \mathbf{F}^{e\mathsf{T}} \mathbf{T} \mathbf{F}^{e-\mathsf{T}} \Big) \cdot \tilde{\mathbf{L}}^p\, dv = 0.$$

Since this must be satisfied for all P and all tensors $\tilde{\mathbf{L}}^p$, a standard argument yields

the *microforce balance*

$$\mathbf{T}^e = \mathbf{T}^p, \qquad \text{where} \qquad \mathbf{T}^e \stackrel{\text{def}}{=} J^e \mathbf{F}^{e\mathsf{T}} \mathbf{T} \mathbf{F}^{e-\mathsf{T}}. \tag{2.33}$$

This balance characterizes the interaction between internal forces associated with the elastic response of the material and internal forces associated with inelasticity.

2.4 Dissipation inequality (second law)

We consider a purely mechanical theory based on a second law requiring that *the temporal increase in free energy of any part P be less than or equal to the power expended on P.* Let ψ denote the *free energy*, measured per unit volume in the relaxed configuration. The second law therefore takes the form of a *dissipation inequality*

$$\dot{\int_P} \psi J^{e-1}\, dv \leq \mathcal{W}_{\text{ext}}(P) = \mathcal{W}_{\text{int}}(P). \tag{2.34}$$

Since $J^{-1}dv$ with $J = \det \mathbf{F}$ represents the volume measure in the reference configuration, and since $P = P(t)$ deforms with the body, we find, using (2.11) and (2.12),

$$\dot{\int_P} \psi J^{e-1}\, dv = \dot{\int_P} \psi J^p J^{-1}\, dv = \int_P \dot{\psi J^p} J^{-1}\, dv = \int_P (\dot{\psi} + \psi\, (\operatorname{tr} \mathbf{L}^p)) J^{e-1}\, dv.$$

Thus, since P is arbitrary, we may use (2.27) to localize (2.34); the result is the *local dissipation inequality*

$$\dot{\psi} - J^e \mathbf{T} \cdot \mathbf{D}^e - \mathbf{T}^p \cdot \mathbf{L}^p + \psi \operatorname{tr} \mathbf{L}^p \leq 0. \tag{2.35}$$

2.5 Constitutive theory

The macroforce balance, the microforce balance, and the dissipation inequality are basic laws, common to large classes of elastic-plastic materials; we keep such laws distinct from specific constitutive equations, which differentiate between particular

materials. We view the dissipation inequality (2.35) as a guide in the development of a suitable constitutive theory. In this regard *we do not seek the most general constitutive equations consistent with the dissipation inequality*; instead we develop *special* constitutive equations close to those upon which the classical theories of plasticity are based.

2.5.1 Constitutive equations

We introduce a list of n scalar *internal state-variables* $\boldsymbol{\xi} = (\xi^1, \xi^2, \ldots, \xi^n)$, and based on experience with existing theories assume that[4]

$$\left.\begin{aligned} \psi &= \hat{\psi}(\mathbf{F}^e, \eta), \\ \mathbf{T} &= \hat{\mathbf{T}}(\mathbf{F}^e, \eta), \\ \mathbf{T}^p &= \hat{\mathbf{T}}^p(\mathbf{L}^p, \eta, \boldsymbol{\xi}), \\ \dot{\xi}^i &= h^i(\mathbf{L}^p, \eta, \boldsymbol{\xi}). \end{aligned}\right\} \tag{2.36}$$

Under a change in frame $\mathbf{F}^e \to \mathbf{Q}\mathbf{F}^e$ and $\mathbf{T} \to \mathbf{Q}\mathbf{T}\mathbf{Q}^\top$, while $\mathbf{L}^p$, $\mathbf{T}^p$ and the scalars η and $\boldsymbol{\xi}$ are invariant; thus, using a standard argument, we see that frame-indifference reduces (2.36) to the specific form

$$\left.\begin{aligned} \psi &= \hat{\psi}(\mathbf{U}^e, \eta), \\ \mathbf{T} &= \mathbf{R}^e \hat{\mathbf{T}}(\mathbf{U}^e, \eta)\mathbf{R}^{e\top}, \\ \mathbf{T}^p &= \hat{\mathbf{T}}^p(\mathbf{L}^p, \eta, \boldsymbol{\xi}), \\ \dot{\xi}^i &= h^i(\mathbf{L}^p, \eta, \boldsymbol{\xi}). \end{aligned}\right\} \tag{2.37}$$

The following definitions help to make precise our notion of an isotropic (amorphous) material (Anand and Gurtin, 2003):

(i) Orth^+ = the group of all rotations (the proper orthogonal group);

[4]To avoid an overly complex presentation, our constitutive equations have been taken to depend on $\mathbf{F}^p$ only through the plastic volumetric strain η, and from the outset we have neglected a dependence of the free energy, ψ, and the Cauchy stress, $\mathbf{T}$, on the internal variables $\boldsymbol{\xi}$.

(ii) the *referential symmetry group* G^{ref} is the group of all rotations of the *reference* configuration that leave the response of the material unaltered;

(iii) the *relaxed symmetry group* G^{rel} is the group of all rotations of the *relaxed* space that leave the response of the material unaltered.

We refer to the material as *isotropic* (*amorphous*) (and to the reference and relaxed spaces as undistorted) if

$$G^{\text{ref}} = \text{Orth}^+, \qquad G^{\text{rel}} = \text{Orth}^+, \tag{2.38}$$

so that the response of the material is invariant under arbitrary rotations of the reference and relaxed spaces.[5]

We now discuss the manner in which the basic fields transform under such transformations, granted the physically natural requirement of invariance of the internal power (2.27), or equivalently, the requirement that

$$\mathbf{T} \cdot \mathbf{D}^e \quad \text{and} \quad \mathbf{T}^p \cdot \mathbf{L}^p \quad \text{be invariant.} \tag{2.39}$$

Let $\mathbf{Q}$ be a *time-independent rotation of the reference configuration.* Then

$$\mathbf{F}^p \to \mathbf{F}^p\mathbf{Q} \quad \text{and} \quad \mathbf{F}^e \text{ is invariant,} \tag{2.40}$$

so that, by (2.3), $\mathbf{L}^e$, and (hence) $\mathbf{D}^e$, and $\mathbf{L}^p$ are invariant. We may therefore use (2.39) to conclude that $\mathbf{T}$ and $\mathbf{T}^p$ are invariant.

On the other hand, let $\mathbf{Q}$ be a *time-independent rotation of the relaxed space.* Then

$$\mathbf{F}^e \to \mathbf{F}^e\mathbf{Q} \quad \text{and} \quad \mathbf{F}^p \to \mathbf{Q}^\top\mathbf{F}^p, \tag{2.41}$$

and hence (2.3) yields the transformation law $\mathbf{L}^p \to \mathbf{Q}^\top\mathbf{L}^p\mathbf{Q}$, and the invariance of $\mathbf{L}^e$, so that $\mathbf{D}^e$ is invariant. Finally, (2.39) yields the invariance of $\mathbf{T}$ and the transformation law $\mathbf{T}^p \to \mathbf{Q}^\top\mathbf{T}^p\mathbf{Q}$.

[5]For metallic glasses this notion attempts to characterize situations in which the material has a completely disordered atomic or molecular structure.

We henceforth restrict attention to materials that are *isotropic* (*amorphous*) in the sense that the constitutive relations (2.36) (or equivalently, (2.37)) are invariant under all rotations of the reference configuration and, independently, under all rotations of the relaxed spaces.

Applying the former we find that our constitutive equations (2.37) are invariant to all rotations of the reference configuration.

Next, let

$$\mathbf{C}^e = \mathbf{F}^{e\top}\mathbf{F}^e = (\mathbf{U}^e)^2,$$

and, in (2.37), replace $\mathbf{R}^e$ by $\mathbf{F}^e\mathbf{U}^{e-1}$ and $\mathbf{U}^e$ by $\sqrt{\mathbf{C}^e}$; this reduces (2.37) to

$$\left.\begin{aligned} \psi &= \bar{\psi}(\mathbf{C}^e, \eta), \\ \mathbf{T} &= \mathbf{F}^e\bar{\mathbf{T}}(\mathbf{C}^e, \eta)\mathbf{F}^{e\top}, \\ \mathbf{T}^p &= \bar{\mathbf{T}}^p(\mathbf{L}^p, \eta, \boldsymbol{\xi}), \\ \dot{\xi}^i &= h^i(\mathbf{L}^p, \eta, \boldsymbol{\xi}). \end{aligned}\right\} \tag{2.42}$$

Our final step is to consider invariance under rotations of the relaxed configuration using the transformation rules specified in the paragraph containing (2.41). Under a rotation $\mathbf{Q}$ of the relaxed space,

$$\mathbf{C}^e \to \mathbf{Q}^\top\mathbf{C}^e\mathbf{Q},$$

and the response functions $\bar{\psi}$, $\bar{\mathbf{T}}$, $\bar{\mathbf{T}}^p$, and h^i appearing in (2.42) must each be *isotropic*.

2.5.2 Thermodynamic restrictions

With a view toward determining the restrictions imposed by the local dissipation inequality, note that

$$\dot{\psi} = \frac{\partial\bar{\psi}}{\partial\mathbf{C}^e}\cdot\dot{\mathbf{C}}^e + \frac{\partial\bar{\psi}}{\partial\eta}\,\dot{\eta}.$$

Using the symmetry of $\partial\bar{\psi}/\partial\mathbf{C}^e$,

$$\frac{\partial\bar{\psi}}{\partial\mathbf{C}^e}\cdot\dot{\mathbf{C}}^e = \frac{\partial\bar{\psi}}{\partial\mathbf{C}^e}\cdot(2\,\mathbf{F}^{e\top}\dot{\mathbf{F}}^e) = \left(2\,\mathbf{F}^e\frac{\partial\bar{\psi}}{\partial\mathbf{C}^e}\mathbf{F}^{e\top}\right)\cdot\mathbf{L}^e = \left(2\,\mathbf{F}^e\frac{\partial\bar{\psi}}{\partial\mathbf{C}^e}\mathbf{F}^{e\top}\right)\cdot\mathbf{D}^e.$$

Thus, using (A.24) and the result above,

$$\dot{\bar{\psi}} = \Big(2\,\mathbf{F}^e \frac{\partial \bar{\psi}}{\partial \mathbf{C}^e} \mathbf{F}^{e\top}\Big) \cdot \mathbf{D}^e + \Big(\frac{\partial \bar{\psi}}{\partial \eta}\ \mathbf{1}\Big) \cdot \mathbf{L}^p. \tag{2.43}$$

If we substitute (2.42) and (2.43) into the local dissipation inequality (2.35), we find that

$$\Big\{\mathbf{F}^e\Big(2\,\frac{\partial \bar{\psi}}{\partial \mathbf{C}^e} - J^e \bar{\mathbf{T}}(\mathbf{C}^e, \eta)\Big)\mathbf{F}^{e\top}\Big\} \cdot \mathbf{D}^e - \Big\{\bar{\mathbf{T}}^p(\mathbf{L}^p, \eta, \boldsymbol{\xi}) - \Big(\bar{\psi} + \frac{\partial \bar{\psi}}{\partial \eta}\Big)\mathbf{1}\Big\} \cdot \mathbf{L}^p \le 0. \tag{2.44}$$

This inequality is to hold for all values of $\mathbf{C}^e$, $\mathbf{D}^e$, $\mathbf{L}^p$, η, and $\boldsymbol{\xi}$. Since $\mathbf{D}^e$ appears linearly, its "coefficient" must vanish. Thus $J^e\,\bar{\mathbf{T}} = 2\,\partial\bar{\psi}/\partial\mathbf{C}^e$, and we are led to the following constitutive relation for the stress:

$$\mathbf{T} = 2\,J^{e-1}\mathbf{F}^e\Big(\frac{\partial \bar{\psi}(\mathbf{C}^e, \eta)}{\partial \mathbf{C}^e}\Big)\mathbf{F}^{e\top}. \tag{2.45}$$

Also, defining

$$\mathbf{Y}^p(\mathbf{C}^e, \mathbf{L}^p, \eta, \boldsymbol{\xi}) \stackrel{\text{def}}{=} \Big\{\bar{\mathbf{T}}^p(\mathbf{L}^p, \eta, \boldsymbol{\xi}) - \Big(\bar{\psi}(\mathbf{C}^e, \eta) + \frac{\partial \bar{\psi}(\mathbf{C}^e, \eta)}{\partial \eta}\Big)\mathbf{1}\Big\}, \tag{2.46}$$

we must have

$$\mathbf{Y}^p(\mathbf{C}^e, \mathbf{L}^p, \eta, \boldsymbol{\xi}) \cdot \mathbf{L}^p \ge 0. \tag{2.47}$$

The left side of (2.47) represents the rate of *energy dissipation*, measured per unit volume in the relaxed space. To rule out trivial special cases, we assume that the material is *strictly dissipative* in the sense that

$$\mathbf{Y}^p(\mathbf{C}^e, \mathbf{L}^p, \eta, \boldsymbol{\xi}) \cdot \mathbf{L}^p > 0 \quad \text{whenever} \quad \mathbf{L}^p \neq \mathbf{0}. \tag{2.48}$$

In light of the dissipation inequality (2.47), we refer to $\mathbf{Y}^p$ as the *dissipative flow stress.*

2.5.3 Flow rule

A central result of the theory—which follows upon using (2.46) and the microforce balance (2.33)—is the *flow rule*

$$\mathbf{T}^e - \Big(\bar{\psi}(\mathbf{C}^e,\eta) + \frac{\partial\bar{\psi}(\mathbf{C}^e,\eta)}{\partial\eta}\Big)\mathbf{1} = \mathbf{Y}^p(\mathbf{C}^e,\mathbf{L}^p,\eta,\boldsymbol{\xi}). \tag{2.49}$$

Using the definition $(2.33)_2$ for $\mathbf{T}^e$ in (2.45), we find that

$$\mathbf{T}^e = 2\,\mathbf{C}^e\frac{\partial\bar{\psi}(\mathbf{C}^e,\eta)}{\partial\mathbf{C}^e}. \tag{2.50}$$

We note that since $\bar{\psi}(\mathbf{C}^e,\eta)$ is an isotropic function of its arguments, the principal directions of $\partial\bar{\psi}(\mathbf{C}^e,\eta)/\partial\mathbf{C}^e$ coincide with those of $\mathbf{C}^e$, and hence for isotropic materials the tensor $\mathbf{T}^e$ is *symmetric*.

Hence, defining the symmetric stress $\boldsymbol{\Sigma}$ by

$$\boldsymbol{\Sigma} \stackrel{\text{def}}{=} \mathbf{T}^e - \Big(\bar{\psi}(\mathbf{C}^e,\eta) + \frac{\partial\bar{\psi}(\mathbf{C}^e,\eta)}{\partial\eta}\Big)\mathbf{1}, \qquad \boldsymbol{\Sigma} = \boldsymbol{\Sigma}^\top, \tag{2.51}$$

we may rewrite the flow rule (2.49) as

$$\boldsymbol{\Sigma} = \mathbf{Y}^p(\mathbf{C}^e,\mathbf{L}^p,\eta,\boldsymbol{\xi}). \tag{2.52}$$

2.6 Specialization of the constitutive equations

The constitutive restrictions derived thus far are fairly general. With a view towards applications we now simplify the theory by imposing additional constitutive assumptions based on experience with existing theories of viscoplasticity.

2.6.1 Invertibility assumption for the flow rule

In classical theories of plasticity, the flow rule is usually specified as an equation for the plastic velocity gradient $\mathbf{L}^p$ in terms of a suitable stress measure and other internal variables. Accordingly, we assume that for fixed state $(\mathbf{T}^e,\mathbf{E}^e,\eta,\boldsymbol{\xi})$, the dissipative

flow stress function $\mathbf{Y}^p$ is *invertible*, so that we may write

$$\mathbf{L}^p = \hat{\mathbf{L}}^p(\boldsymbol{\Sigma}, \eta, \boldsymbol{\xi}). \tag{2.53}$$

In this case, the dissipation inequality (2.48) may be written as

$$\boldsymbol{\Sigma} \cdot \hat{\mathbf{L}}^p(\boldsymbol{\Sigma}, \eta, \boldsymbol{\xi}) > 0 \quad \text{for} \quad \mathbf{L}^p \neq \mathbf{0}. \tag{2.54}$$

Since the function $\mathbf{Y}^p$ is isotropic, we assume that the function $\hat{\mathbf{L}}^p$ is also an *isotropic function* of its arguments.

2.6.2 Free energy function. Elastic constitutive equations

Let

$$\mathbf{U}^e = \sum_{\alpha=1}^{3} \lambda_\alpha^e \, \mathbf{r}_\alpha \otimes \mathbf{r}_\alpha, \qquad \mathbf{C}^e = \sum_{\alpha=1}^{3} \lambda_\alpha^{e\,2} \, \mathbf{r}_\alpha \otimes \mathbf{r}_\alpha, \tag{2.55}$$

be the spectral representation of $\mathbf{U}^e$ and $\mathbf{C}^e$, respectively, with $\{\lambda_\alpha^e | \alpha = 1, 2, 3\}$ the positive eigenvalues, and $\{\mathbf{r}_\alpha | \alpha = 1, 2, 3\}$ the orthonormal eigenvectors of $\mathbf{U}^e$. Then, the isotropic free energy function may be expressed as a symmetric function of the principal stretches λ_α^e:

$$\bar{\psi}(\mathbf{C}^e, \eta) = \tilde{\psi}(\lambda_1^e, \lambda_2^e, \lambda_3^e, \eta). \tag{2.56}$$

Restricting our attention (for now) to the case of distinct eigenvalues $\{\lambda_\alpha^e | \alpha = 1, 2, 3\}$, and using the chain rule we obtain

$$\frac{\partial \bar{\psi}(\mathbf{C}^e, \eta)}{\partial \mathbf{C}^e} = \sum_{\alpha=1}^{3} \frac{\partial \tilde{\psi}}{\partial \lambda_\alpha^e} \, \frac{\partial \lambda_\alpha^e}{\partial \lambda_\alpha^{e\,2}} \, \frac{\partial \lambda_\alpha^{e\,2}}{\partial \mathbf{C}^e} \, .$$

Then, since $\lambda_\alpha^e = \sqrt{\lambda_\alpha^{e\,2}}$ and $\lambda_\alpha^{e\,2} = \mathbf{r}_\alpha \cdot \mathbf{C}^e \mathbf{r}_\alpha$, we obtain

$$\mathbf{T}^e = 2\mathbf{C}^e \, \frac{\partial \bar{\psi}(\mathbf{C}^e, \eta)}{\partial \mathbf{C}^e} = \sum_{\alpha=1}^{3} \lambda_\alpha^e \, \frac{\partial \tilde{\psi}}{\partial \lambda_\alpha^e} \, \mathbf{r}_\alpha \otimes \mathbf{r}_\alpha. \tag{2.57}$$

Let

$$\mathbf{E}^e \stackrel{\text{def}}{=} \sum_{\alpha=1}^{3} E^e_\alpha \, \mathbf{r}_\alpha \otimes \mathbf{r}_\alpha \tag{2.58}$$

denote the symmetric *logarithmic elastic strain tensor*, with *principal logarithmic elastic strains*

$$E^e_\alpha \stackrel{\text{def}}{=} \ln \lambda^e_\alpha. \tag{2.59}$$

Then, (2.57) may be written as

$$\mathbf{T}^e = \sum_{\alpha=1}^{3} \frac{\partial \tilde{\psi}}{\partial E^e_\alpha} \, \mathbf{r}_\alpha \otimes \mathbf{r}_\alpha, \tag{2.60}$$

from which we note that *for isotropic materials the symmetric stress measure* $\mathbf{T}^e$ *is power-conjugate to the logarithmic elastic strain.*

Thus, for isotropic materials we may replace the free energy function $\tilde{\psi}(\lambda^e_1, \lambda^e_2, \lambda^e_3, \eta)$ by

$$\tilde{\psi}(\mathbf{E}^e, \eta),$$

with the stress measure $\mathbf{T}^e$ given by

$$\mathbf{T}^e = \frac{\partial \tilde{\psi}(\mathbf{E}^e, \eta)}{\partial \mathbf{E}^e} \, . \tag{2.61}$$

Recalling $(2.33)_2$, we note that for isotropic materials

$$\mathbf{T}^e \stackrel{\text{def}}{=} \mathbf{F}^{e\mathsf{T}}(J^e\mathbf{T})\mathbf{F}^{e-\mathsf{T}} \equiv \mathbf{R}^{e\mathsf{T}}(J^e\mathbf{T})\mathbf{R}^e. \tag{2.62}$$

To describe the elastic response of the solid we consider the following simple generalization of the classical strain energy function of infinitesimal isotropic elasticity, in which we replace the infinitesimal measure of elastic strain by the logarithmic measure of finite elastic strain (Anand, 1979):

$$\tilde{\psi}(\mathbf{E}^e, \eta) = G|\mathbf{E}^e_0|^2 + \frac{1}{2}K(\operatorname{tr}\mathbf{E}^e)^2, \tag{2.63}$$

where

$$G = \hat{G}(\eta) > 0, \quad K = \hat{K}(\eta) > 0 \tag{2.64}$$

are the elastic shear and bulk moduli, which we have assumed to depend on plastic volumetric strain η. In this case the constitutive equations for the stress becomes

$$\mathbf{T}^e = 2G\mathbf{E}_0^e + K\,(\mathrm{tr}\,\mathbf{E}^e)\mathbf{1}. \tag{2.65}$$

2.6.3 Kinematical hypothesis for plastic velocity gradient. Internal variables

We assume that plastic flow occurs by shearing accompanied by dilatation (or compaction) relative to some slip systems. Each slip system is specified by a slip direction $\mathbf{s}^{(\alpha)}$, and a slip plane normal $\mathbf{m}^{(\alpha)}$ (we label slip systems by integers α), with

$$\mathbf{s}^{(\alpha)} \cdot \mathbf{m}^{(\alpha)} = 0, \qquad |\mathbf{s}^{(\alpha)}|,\ |\mathbf{m}^{(\alpha)}| = 1, \tag{2.66}$$

and we take the plastic stretching to be made up of shearing rates $\nu^{(\alpha)}$ on the set of potential slip systems, and assume that this shearing is accompanied by *shear-induced dilatation* rates $\delta^{(\alpha)}$ in the directions normal to the shear directions. That is, the total plastic velocity gradient is taken as

$$\left.\begin{aligned} \mathbf{L}^p &= \sum_\alpha \mathbf{L}^{p(\alpha)}, \\ \mathbf{L}^{p(\alpha)} &= \nu^{(\alpha)}(\mathbf{s}^{(\alpha)} \otimes \mathbf{m}^{(\alpha)}) + \delta^{(\alpha)}(\mathbf{m}^{(\alpha)} \otimes \mathbf{m}^{(\alpha)}), \qquad \nu^{(\alpha)} \geq 0, \\ \delta^{(\alpha)} &= \beta\,\nu^{(\alpha)}, \end{aligned}\right\} \tag{2.67}$$

where β is a *dilatancy function.* Positive values of β describe plastically dilatant behavior, while $\beta < 0$ describes behavior that is plastically compacting.

For an amorphous isotropic material there are no preferred directions other than the principal directions of stress, and accordingly we consider potential slip systems with respect to these principal directions of stress. The symmetric stress $\mathbf{\Sigma}$ has the

spectral representation

$$\boldsymbol{\Sigma} = \sum_{i=1}^{3} \sigma_i \, \hat{\mathbf{e}}_i \otimes \hat{\mathbf{e}}_i. \tag{2.68}$$

where $\{\sigma_i | i = 1, 2, 3\}$ are the principal values, and $\{\hat{\mathbf{e}}_i | i = 1, 2, 3\}$ are the orthonormal principal directions of $\boldsymbol{\Sigma}$. We assume that the principal stresses $\{\sigma_i | i = 1, 2, 3\}$ are strictly ordered such that

$$\sigma_1 \geq \sigma_2 \geq \sigma_3. \tag{2.69}$$

First, consider potential slip in the $(\hat{\mathbf{e}}_1, \hat{\mathbf{e}}_3)$-plane. Let $\left(\mathbf{s}^{(\alpha)}, \mathbf{m}^{(\alpha)}\right)$ denote a potential slip system lying in this plane and oriented such that $\mathbf{s}^{(\alpha)}$ makes an angle ϑ with respect to the $\hat{\mathbf{e}}_1$-axis

$$\mathbf{s}^{(\alpha)} = \cos\vartheta \hat{\mathbf{e}}_1 + \sin\vartheta \hat{\mathbf{e}}_3, \qquad \mathbf{m}^{(\alpha)} = \sin\vartheta \hat{\mathbf{e}}_1 - \cos\vartheta \hat{\mathbf{e}}_3,$$

and let

$$\tau^{(\alpha)}(\vartheta) = \mathbf{s}^{(\alpha)} \cdot \boldsymbol{\Sigma}\mathbf{m}^{(\alpha)}, \qquad \text{and} \qquad \sigma^{(\alpha)}(\vartheta) = -\mathbf{m}^{(\alpha)} \cdot \boldsymbol{\Sigma}\mathbf{m}^{(\alpha)},$$

denote the resolved shear stress and compressive normal traction for such a system. Then, introducing an internal variable $\mu \geq 0$ called the *internal friction coefficient*, we define the quantity

$$\phi \stackrel{\text{def}}{=} \arctan\mu \tag{2.70}$$

called the *angle of internal friction*, and assume that any given instant for a fixed stress $\boldsymbol{\Sigma}$, shearing is possible only on those slip systems for which

$$f(\vartheta) = \{\tau(\vartheta) - (\tan\phi)\,\sigma(\vartheta)\},$$

is a *maximum* with respect to ϑ (Coulomb, 1773). It is easily shown that $f(\vartheta)$ is a maximum for

$$\vartheta = \pm\left\{\frac{\pi}{4} + \frac{\phi}{2}\right\}. \tag{2.71}$$

Hence, there are two potential slip systems in the $(\hat{\mathbf{e}}_1, \hat{\mathbf{e}}_3)$-plane, with slip directions

which are symmetrically disposed about the maximum principal stress direction:

$$\left.\begin{aligned} \mathbf{s}^{(1)} &= \cos\vartheta\hat{\mathbf{e}}_1 + \sin\vartheta\hat{\mathbf{e}}_3, \quad \mathbf{m}^{(1)} = \sin\vartheta\hat{\mathbf{e}}_1 - \cos\vartheta\hat{\mathbf{e}}_3, \\ \mathbf{s}^{(2)} &= \cos\vartheta\hat{\mathbf{e}}_1 - \sin\vartheta\hat{\mathbf{e}}_3, \quad \mathbf{m}^{(2)} = \sin\vartheta\hat{\mathbf{e}}_1 + \cos\vartheta\hat{\mathbf{e}}_3, \end{aligned}\right\} \tag{2.72}$$

with

$$\vartheta = (\pi/4) + (\phi/2). \tag{2.73}$$

In an entirely analogous manner, the slip systems in the $(\hat{\mathbf{e}}_1, \hat{\mathbf{e}}_2)$-plane are

$$\left.\begin{aligned} \mathbf{s}^{(3)} &= \cos\vartheta\hat{\mathbf{e}}_1 + \sin\vartheta\hat{\mathbf{e}}_2, \quad \mathbf{m}^{(3)} = \sin\vartheta\hat{\mathbf{e}}_1 - \cos\vartheta\hat{\mathbf{e}}_2, \\ \mathbf{s}^{(4)} &= \cos\vartheta\hat{\mathbf{e}}_1 - \sin\vartheta\hat{\mathbf{e}}_2, \quad \mathbf{m}^{(4)} = \sin\vartheta\hat{\mathbf{e}}_1 + \cos\vartheta\hat{\mathbf{e}}_2, \end{aligned}\right\} \tag{2.74}$$

while those in the $(\hat{\mathbf{e}}_2, \hat{\mathbf{e}}_3)$-plane are

$$\left.\begin{aligned} \mathbf{s}^{(5)} &= \cos\vartheta\hat{\mathbf{e}}_2 + \sin\vartheta\hat{\mathbf{e}}_3, \quad \mathbf{m}^{(5)} = \sin\vartheta\hat{\mathbf{e}}_2 - \cos\vartheta\hat{\mathbf{e}}_3, \\ \mathbf{s}^{(6)} &= \cos\vartheta\hat{\mathbf{e}}_2 - \sin\vartheta\hat{\mathbf{e}}_3, \quad \mathbf{m}^{(6)} = \sin\vartheta\hat{\mathbf{e}}_2 + \cos\vartheta\hat{\mathbf{e}}_3. \end{aligned}\right\} \tag{2.75}$$

Thus, the total velocity gradient is made up of contributions from shearing on each of the six potential slip systems:

$$\mathbf{L}^p = \sum_{\alpha=1}^{6} \nu^{(\alpha)} \left\{ (\mathbf{s}^{(\alpha)} \otimes \mathbf{m}^{(\alpha)}) + \beta \mathbf{m}^{(\alpha)} \otimes \mathbf{m}^{(\alpha)} \right\}. \tag{2.76}$$

The shearing rates $\nu^{(\alpha)}$ are taken to be constitutively prescribed by a flow equation as follows:

$$\nu^{(\alpha)} = \nu_0 \left\{ \frac{\tau^{(\alpha)}}{c + \mu\sigma^{(\alpha)}} \right\}^{1/m} \geq 0\,, \tag{2.77}$$

where we have introduced another internal variable $c > 0$, called the *cohesion* (Coulomb, 1773). Also, $\nu_0 > 0$ is a *reference plastic shear strain rate*, such that $\nu^{(\alpha)} = \nu_0$ when $\tau^{(\alpha)} = c + \mu\sigma^{(\alpha)}$, and $m > 0$ is a *strain-rate sensitivity parameter*. For $\nu^{\alpha} > 0$, the flow equation (2.77) may be inverted to read

$$\tau^{(\alpha)} = \left(c + \mu\sigma^{(\alpha)}\right) \left(\frac{\nu^{(\alpha)}}{\nu_0}\right)^m. \tag{2.78}$$

Thus, it is clear that the limit $m \to 0$ renders the theory *rate-independent.*[6]

The dissipation inequality (2.54) requires that

$$\mathbf{\Sigma} \cdot \mathbf{L}^p = \sum_{\alpha=1}^{6} \left[\tau^{(\alpha)} - \beta\, \sigma^{(\alpha)}\right] \nu^{(\alpha)} > 0, \tag{2.79}$$

whenever plastic flow occurs. On physical grounds we require that

$$\left[\tau^{(\alpha)} - \beta\, \sigma^{(\alpha)}\right] \nu^{(\alpha)} > 0 \qquad \text{for each } \alpha\,; \tag{2.80}$$

thus, whenever $\nu^{(\alpha)} > 0$, we must have

$$\left[\tau^{(\alpha)} - \beta\, \sigma^{(\alpha)}\right] > 0, \tag{2.81}$$

which is a *restriction* that the dilatancy function β must satisfy.

We emphasize that we do not assume that $\mu = \beta$, which (using classical terminology) would correspond to an *associated/normality flow rule.*

Straight-forward calculations show that the resolved shear stresses and compressive normal tractions on the slip systems are given by

$$\left.\begin{aligned} \tau^{(1,2)} &= \tfrac{1}{2}\sin(2\vartheta)(\sigma_1 - \sigma_3), \quad \sigma^{(1,2)} &&= -\tfrac{1}{2}(\sigma_1 + \sigma_3) + \tfrac{1}{2}\cos(2\vartheta)(\sigma_1 - \sigma_3), \\ \tau^{(3,4)} &= \tfrac{1}{2}\sin(2\vartheta)(\sigma_1 - \sigma_2), \quad \sigma^{(3,4)} &&= -\tfrac{1}{2}(\sigma_1 + \sigma_2) + \tfrac{1}{2}\cos(2\vartheta)(\sigma_1 - \sigma_2), \\ \tau^{(5,6)} &= \tfrac{1}{2}\sin(2\vartheta)(\sigma_2 - \sigma_3), \quad \sigma^{(5,6)} &&= -\tfrac{1}{2}(\sigma_2 + \sigma_3) + \tfrac{1}{2}\cos(2\vartheta)(\sigma_2 - \sigma_3). \end{aligned}\right\} \tag{2.82}$$

Thus, from (2.77) we note that in the case of distinct principal stresses

$$\nu^{(1)} = \nu^{(2)}, \qquad \nu^{(3)} = \nu^{(4)}, \qquad \nu^{(5)} = \nu^{(6)}, \quad \text{if} \quad \sigma_1 > \sigma_2 > \sigma_3, \tag{2.83}$$

and in situations when the principal stresses are not distinct we have

$$\nu^{(1)} = \nu^{(2)} = \nu^{(3)} = \nu^{(4)}, \qquad \nu^{(5)} = \nu^{(6)} = 0 \quad \text{if} \quad \sigma_1 > \sigma_2 = \sigma_3, \tag{2.84}$$

[6]More elaborate forms for the rate-dependence may be considered, but a simple power-law rate-dependence makes the structure of our theory more transparent.

$$\nu^{(1)} = \nu^{(2)} = \nu^{(5)} = \nu^{(6)}, \qquad \nu^{(3)} = \nu^{(4)} = 0, \quad \text{if} \quad \sigma_1 = \sigma_2 > \sigma_3\,, \tag{2.85}$$

and

$$\nu^{(1)} = \nu^{(2)} = \nu^{(3)} = \nu^{(4)} = \nu^{(5)} = \nu^{(6)} = 0 \quad \text{if} \quad \sigma_1 = \sigma_2 = \sigma_3\,. \tag{2.86}$$

Remark 1: When $\sigma_1 > \sigma_2 = \sigma_3$, $\hat{\mathbf{e}}_2$ and $\hat{\mathbf{e}}_3$ are *any two* orthonormal vectors perpendicular to $\hat{\mathbf{e}}_1$, and we have an *infinite number of potential slip systems with slip directions* $\mathbf{s}^{(\alpha)}$ *lying on a cone with axis* $\hat{\mathbf{e}}_1$ *and a semi-angle* $\vartheta = \{(\pi/4) + (\phi/2)\}$. In enumerating our slip systems we choose *an arbitrary pair* of orthonormal vectors $(\hat{\mathbf{e}}_2, \hat{\mathbf{e}}_3)$ perpendicular to $\hat{\mathbf{e}}_1$; this choice, and therefore the choice of slip systems is clearly non-unique. A similar remark concerning a non-unique choice of slip systems holds when $\sigma_1 = \sigma_2 > \sigma_3$.

Remark 2: On account of (2.83), (2.84), (2.85), we note the important result that in this flow rule for isotropic materials, the plastic spin vanishes, $\mathbf{W}^p = \mathbf{0}$.

2.6.4 Evolution equations for internal variables. Dilatancy equation

The internal variables $\boldsymbol{\xi}$ of the model are the cohesion c and the internal friction $\mu = \tan\phi$, for which we need to prescribe evolution equations, and we also need to specify a constitutive equation for the dilatancy function β, which determines the evolution of the volumetric plastic strain η.

For the amorphous metallic materials under consideration we adopt the following special forms:

(1) **Internal friction**: The internal friction μ is taken to be a constant,

$$\mu = \mu_0 > 0. \tag{2.87}$$

(2) **Evolution of η. Dilatancy Function. Evolution of c**: The *free-volume* for an amorphous material is defined to be the difference between the actual specific volume of the material and the specific volume if the material was in a state of dense random packing. A key feature controlling the plastic deformation of

amorphous materials is the evolution of the local free-volume associated with the metastable state of these materials. It is commonly believed that for amorphous materials the increase of the free-volume is the major reason for the the post-yield strain-softening and formation of shear bands.

In our macroscopic theory, we associate the *change in the free-volume of an amorphous material from its virgin state* with the *plastic volumetric strain* η. During the initial stages of plastic flow from a virgin state we expect the free volume η to increase monotonically to an equilibrium value $\eta_{\rm cv}$, while the cohesion c decreases smoothly to an equilibrium value $c_{\rm cv}$. The parameter c_{cv} denotes a value of c in the fully-developed, *constant plastic volume* state, where $\eta = \eta_{cv}$ and $\dot{\eta} = 0$. With this physical picture in mind we develop evolution equations for η and c in the special coupled-form shown below.

Recalling (A.24), that is $\dot{\eta} = \operatorname{tr}\mathbf{L}^p$, and using (2.76) we have that

$$\dot{\eta} = \beta\,\nu, \qquad \text{where} \quad \nu \stackrel{\text{def}}{=} \sum_{\alpha=1}^{6} \nu^{(\alpha)}. \tag{2.88}$$

We assume that the dilatancy function β depends on the current value of η, and take this dependency to be in the form

$$\dot{\eta} = g_0 \left(1 - \frac{\eta}{\eta_{cv}}\right)^p \nu, \qquad \eta(0) = 0, \tag{2.89}$$

where g_0, η_{cv}, and p are positive-valued material parameters.

Further, we assume that the cohesion c decreases as the material softens due to the increase in the free-volume during the course of deformation. This is modelled phenomenologically by

$$c = c_{cv} + b \left(1 - \frac{\eta}{\eta_{cv}}\right)^q, \qquad c(0) = c_{cv} + b, \tag{2.90}$$

where c_{cv}, b and q are additional positive-valued material parameters. Thus, using (5.17) and (5.22) the evolution of the cohesion is governed by the differential

equation

$$\dot{c} = -\left\{ b\, q\, g_0 \left(1 - \frac{\eta}{\eta_{cv}}\right)^{p+q-1} \right\} \nu, \qquad \text{with} \quad c(0) = c_{cv} + b. \tag{2.91}$$

2.7 Final constitutive equations

In this section we summarize the resulting constitutive theory. The underlying constitutive equations relate the following basic fields:

ψ,	free energy density per unit volume of relaxed space,
$\mathbf{y}$,	motion,
$\mathbf{F} = \nabla \mathbf{y}, \quad J = \det \mathbf{F} > 0,$	deformation gradient,
$\mathbf{F}^p, \quad J^p = \det \mathbf{F}^p > 0,$	plastic deformation gradient,
$\mathbf{F}^e = \mathbf{F}\mathbf{F}^{p-1}, \quad J^e = \det \mathbf{F}^e > 0,$	elastic deformation gradient,
$\mathbf{F}^e = \mathbf{R}^e \mathbf{U}^e,$	polar decomposition of $\mathbf{F}^e$,
$\mathbf{U}^e = \sum_{\alpha=1}^{3} \lambda_\alpha^e \mathbf{r}_\alpha \otimes \mathbf{r}_\alpha,$	spectral decomposition of $\mathbf{U}^e$,
$\mathbf{E}^e = \sum_{\alpha=1}^{3} (\ln \lambda_\alpha^e) \mathbf{r}_\alpha \otimes \mathbf{r}_\alpha,$	logarithmic elastic strain,
$\epsilon^e = \operatorname{tr} \mathbf{E}^e,$	volumetric elastic strain,
$\mathbf{E}_0^e = \mathbf{E}^e - \frac{1}{3}(\epsilon^e)\mathbf{1},$	deviatoric elastic strain,
$\mathbf{T}, \quad \mathbf{T} = \mathbf{T}^\top,$	Cauchy stress,
$\mathbf{T}^e = \mathbf{R}^{e\top}(J^e \mathbf{T})\mathbf{R}^e,$	stress conjugate to elastic strain $\mathbf{E}^e$,
$\eta = \ln J^p,$	plastic volumetric strain
$c,$	cohesion,
$\mu \geq 0,$	internal friction coefficient,
$\phi = \arctan \mu,$	internal friction angle,
$\beta,$	dilatancy parameter.

The special set of constitutive equations that should be useful in applications are summarized below:

(1) **Free energy**:

$$\tilde{\psi}(\mathbf{E}^e, \eta) = G|\mathbf{E}_0^e|^2 + \tfrac{1}{2}K(\mathrm{tr}\,\mathbf{E}^e)^2, \tag{2.92}$$

with

$$G = \hat{G}(\eta) > 0, \quad K = \hat{K}(\eta) > 0, \tag{2.93}$$

the elastic shear modulus and bulk modulus, which depend on the plastic volumetric strain η.

(2) **Equation for the stress**:

$$\mathbf{T}^e = \frac{\partial \tilde{\psi}(\mathbf{E}^e, \eta)}{\partial \mathbf{E}^e} = 2G\mathbf{E}_0^e + K\,(\mathrm{tr}\,\mathbf{E}^e)\mathbf{1}. \tag{2.94}$$

(3) **Dissipative stress**:

The thermodynamically-consistent driving stress for plastic flow is given by

$$\mathbf{\Sigma} \stackrel{\text{def}}{=} \mathbf{T}^e - \Big(\tilde{\psi}(\mathbf{E}^e, \eta) + \frac{\partial \tilde{\psi}(\mathbf{E}^e, \eta)}{\partial \eta}\Big)\mathbf{1}, \tag{2.95}$$

and this symmetric stress tensor has the spectral representation

$$\mathbf{\Sigma} = \sum_{i=1}^{3} \sigma_i\, \hat{\mathbf{e}}_i \otimes \hat{\mathbf{e}}_i, \tag{2.96}$$

where $\{\sigma_i | i = 1, 2, 3\}$ are the principal values, and $\{\hat{\mathbf{e}}_i | i = 1, 2, 3\}$ are the orthonormal principal directions of $\mathbf{\Sigma}$. We assume that the principal stresses $\{\sigma_i | i = 1, 2, 3\}$ are strictly ordered such that

$$\sigma_1 \geq \sigma_2 \geq \sigma_3. \tag{2.97}$$

(4) **Slip systems. Resolved shear stress. Compressive normal traction:**

We assume that plastic flow occurs by shearing accompanied by dilatation (or compaction) relative to some slip systems. Slip systems are labelled by integers α; each slip system is specified by a slip direction $\mathbf{s}^\alpha$, and a slip plane normal

$\mathbf{m}^\alpha$ with

$$\mathbf{s}^{(\alpha)} \cdot \mathbf{m}^{(\alpha)} = 0, \qquad |\mathbf{s}^{(\alpha)}|,\ |\mathbf{m}^{(\alpha)}| = 1. \tag{2.98}$$

For an amorphous isotropic material there are no preferred directions other than the principal directions of stress, and accordingly we consider plastic flow to be possible on six potential slip systems defined relative to the principal directions of stress $\mathbf{\Sigma}$:

$$\left.\begin{aligned}
\mathbf{s}^{(1)} &= \cos\vartheta\hat{\mathbf{e}}_1 + \sin\vartheta\hat{\mathbf{e}}_3, \quad & \mathbf{m}^{(1)} &= \sin\vartheta\hat{\mathbf{e}}_1 - \cos\vartheta\hat{\mathbf{e}}_3,\\
\mathbf{s}^{(2)} &= \cos\vartheta\hat{\mathbf{e}}_1 - \sin\vartheta\hat{\mathbf{e}}_3, \quad & \mathbf{m}^{(2)} &= \sin\vartheta\hat{\mathbf{e}}_1 + \cos\vartheta\hat{\mathbf{e}}_3,\\
\mathbf{s}^{(3)} &= \cos\vartheta\hat{\mathbf{e}}_1 + \sin\vartheta\hat{\mathbf{e}}_2, \quad & \mathbf{m}^{(3)} &= \sin\vartheta\hat{\mathbf{e}}_1 - \cos\vartheta\hat{\mathbf{e}}_2,\\
\mathbf{s}^{(4)} &= \cos\vartheta\hat{\mathbf{e}}_1 - \sin\vartheta\hat{\mathbf{e}}_2, \quad & \mathbf{m}^{(4)} &= \sin\vartheta\hat{\mathbf{e}}_1 + \cos\vartheta\hat{\mathbf{e}}_2,\\
\mathbf{s}^{(5)} &= \cos\vartheta\hat{\mathbf{e}}_2 + \sin\vartheta\hat{\mathbf{e}}_3, \quad & \mathbf{m}^{(5)} &= \sin\vartheta\hat{\mathbf{e}}_2 - \cos\vartheta\hat{\mathbf{e}}_3,\\
\mathbf{s}^{(6)} &= \cos\vartheta\hat{\mathbf{e}}_2 - \sin\vartheta\hat{\mathbf{e}}_3, \quad & \mathbf{m}^{(6)} &= \sin\vartheta\hat{\mathbf{e}}_2 + \cos\vartheta\hat{\mathbf{e}}_3.
\end{aligned}\right\} \tag{2.99}$$

where

$$\vartheta = \frac{\pi}{4} + \frac{\phi}{2}. \tag{2.100}$$

and

$$\phi \stackrel{\text{def}}{=} \arctan\mu \tag{2.101}$$

is an *angle of internal friction*, and $\mu \geq 0$ is a *friction coefficient.*

The resolved shear and compressive normal traction on each slip system are given by

$$\tau^{(\alpha)} \stackrel{\text{def}}{=} \mathbf{s}^{(\alpha)} \cdot \mathbf{\Sigma}\mathbf{m}^{(\alpha)}, \qquad \sigma^{(\alpha)} \stackrel{\text{def}}{=} -\mathbf{m}^{(\alpha)} \cdot \mathbf{\Sigma}\mathbf{m}^{(\alpha)}. \tag{2.102}$$

(5) **Flow rule**:

The evolution equation for $\mathbf{F}^p$ is

$$\dot{\mathbf{F}}^p = \mathbf{D}^p\,\mathbf{F}^p, \qquad \mathbf{F}^p(\mathbf{X}, 0) = \mathbf{1}, \tag{2.103}$$

with $\mathbf{D}^p$ given by

$$\mathbf{D}^p = \sum_{\alpha=1}^{6} \nu^{(\alpha)} \left[\text{sym} \left(\mathbf{s}^{(\alpha)} \otimes \mathbf{m}^{(\alpha)} \right) + \beta \, \mathbf{m}^{(\alpha)} \otimes \mathbf{m}^{(\alpha)} \right]. \tag{2.104}$$

The constitutive equation for the shearing rates $\nu^{(\alpha)}$ is taken as

$$\nu^{(\alpha)} = \nu_0 \left\{ \frac{\tau^{(\alpha)}}{c + \mu \sigma^{(\alpha)}} \right\}^{1/m} > 0, \tag{2.105}$$

where $c > 0$ is an internal variable called the *cohesion*. Also, ν_0 is a *reference plastic shear strain rate*, such that $\nu^{(\alpha)} = \nu_0$ when $\tau^{(\alpha)} = c + \mu \sigma^{(\alpha)}$, and $m > 0$ is a *strain-rate sensitivity parameter*. For $\nu^{\alpha} > 0$, the flow equation $(2.105)_2$ may be inverted to read

$$\tau^{(\alpha)} = \left\{ c + \mu \sigma^{(\alpha)} \right\} \left(\frac{\nu^{(\alpha)}}{\nu_0} \right)^m \tag{2.106}$$

Thus, the limit $m \to 0$ renders the theory *rate-independent*.

The quantity β is a *shear-induced plastic dilatancy function*. Positive values of β describe plastically dilatant behavior, while $\beta < 0$ describes behavior that is plastically compacting. The dissipation inequality requires that

$$\mathbf{\Sigma} \cdot \mathbf{L}^p = \sum_{\alpha=1}^{6} \left[\tau^{(\alpha)} - \beta \, \sigma^{(\alpha)} \right] \nu^{(\alpha)} > 0 \tag{2.107}$$

whenever plastic flow occurs. We require that

$$\left[\tau^{(\alpha)} - \beta \, \sigma^{(\alpha)} \right] \nu^{(\alpha)} > 0 \qquad \text{for each } \alpha\,; \tag{2.108}$$

thus, whenever $\nu^{(\alpha)} > 0$, we must have

$$\left[\tau^{(\alpha)} - \beta \, \sigma^{(\alpha)} \right] > 0. \tag{2.109}$$

This is a restriction that the dilatancy function β must satisfy.

We emphasize that we do not assume that $\mu = \beta$, which would correspond to

an *associated/normality flow rule.*

The dilatancy function is taken as

$$\beta = g_0 \left(1 - \frac{\eta}{\eta_{cv}}\right)^p, \tag{2.110}$$

where g_0, η_{cv} and p are positive-valued material parameters. Thus, $\beta = 0$ when $\eta = \eta_{cv}$, and η_{cv} denotes the value of the plastic volume change in the fully-developed constant plastic volume state.

(6) **Evolution equations for η, c and μ:**

For the amorphous metallic materials under consideration we take the internal friction μ to be a constant,

$$\mu = \mu_0 > 0. \tag{2.111}$$

Recall that $\eta = \ln J^p$, and therefore $\dot{\eta} = \operatorname{tr} \mathbf{L}^p$. Thus using (2.104) we have that

$$\dot{\eta} = \beta \nu, \qquad \text{where} \quad \nu \stackrel{\text{def}}{=} \sum_{\alpha=1}^{6} \nu^{(\alpha)}. \tag{2.112}$$

With β given by (2.110), we have

$$\dot{\eta} = g_0 \left(1 - \frac{\eta}{\eta_{cv}}\right)^p \nu, \qquad \eta(0) = 0\,. \tag{2.113}$$

The cohesion is taken to depend on the plastic volumetric strain as

$$c = c_{cv} + b \left(1 - \frac{\eta}{\eta_{cv}}\right)^q, \qquad c(0) = c_{cv} + b, \tag{2.114}$$

where c_{cv}, b and q are additional positive-valued material parameters. Thus, the evolution of the cohesion is governed by the differential equation

$$\dot{c} = -\left\{ b\, q\, g_0 \left(1 - \frac{\eta}{\eta_{cv}}\right)^{p+q-1} \right\} \nu, \qquad \text{with} \quad c(0) = c_{cv} + b. \tag{2.115}$$

Chapter 3

Application to a Zr-based bulk metallic glasses

We have implemented our constitutive model in the finite-element computer program ABAQUS/Explicit (2004) by writing a user material subroutine. Using this numerical capability, in this section we present results from simulations of some prototypical problems concerning the mechanical response of a representative Zirconium-based bulk metallic glass in tension, compression, bending, and indentation. At the outset we note that we shall *not* attempt to *quantitatively* match experimental data because we have not conducted any experiments of our own to determine the material parameters in our constitutive model. However, using reasonable values for the material parameters, we shall show that the results from our simulations *qualitatively* reproduce the salient features of the response of zirconium-based bulk metallic glasses observed in experiments reported in the literature.

3.1 Estimates of material parameters for a zirconium-based metallic glass

The specific values of the material parameters that we have used in our simulations are:

- Elastic Moduli (?): $E = 96\,\text{GPa}$, $\nu = 0.36 \Rightarrow G = 35.3\,\text{GPa}$, $K = 114.3\,\text{GPa}$.

For simplicity we have assumed that the effect of the very small plastic volume change (see below) on the elastic moduli of amorphous metals is negligible.

- Friction coefficient (Lewandowski and Lowhaphandu, 2002): $\mu = 0.04$

- Viscoplasticity parameters: $\nu_0 = 0.001$, $m = 0.005$.

  The glass transition temperature of Zirconium-based metallic glasses is $\approx 625\,\mathrm{K}$, and under room temperature conditions $\approx 300\,\mathrm{K}$, the mechanical response of these materials is observed to be *almost rate-insensitive.* The low value of the strain-rate sensitivity parameter $m = 0.005$ is chosen to model such a nearly rate-independent response.

- Plastic volume change:

$$\dot{\eta} = \beta\nu, \qquad \beta = g_0\Big(1 - \frac{\eta}{\eta_{cv}}\Big)^p,$$

$$g_0 = 0.04 \text{ in compression, } 0.4 \text{ in tension,} \qquad \eta_{cv} = 0.005, \qquad p = 0.8.$$

  Density measurements in metallic glasses show that the *overall* maximum density reduction as a result of plastic deformation is approximately $0.15 - 0.25$ However, experiments are inconclusive about the *maximum* amount of dilatation *in fully developed shear bands*; here we assume this maximum to be a small number, $\eta_{cv} = 0.005$, twice the value indicated by the overall density reduction. Of particular note is our use of two different values for the parameter g_0 in the dilatancy relation. Physically, we expect that the *rate of dilatation* can be much higher in tension than in compression; accordingly we have assumed that $g_0 = 0.04$ in compression, while it has a value ten times higher, $g_0 = 0.4$, in tension.[1] These differing values of g_0, and hence the dilatancy parameter β, are crucial in providing an explanation for the differing values of the shear-band orientations in tension and compression.

[1]The total amount of dilatation can also possibly be higher in tension than in compression, but the experimental evidence is weak here.

- Cohesion function:

$$c = c_{cv} + b\left(1 - \frac{\eta}{\eta_{cv}}\right)^q, \; c_0 = 960\,\text{MPa}, \; c_{cv} = 660\,\text{MPa}, \; b = 300\,\text{MPa}, \; q = 1.2.$$

The stress-strain curves in tension and compression obtained from a single finite-element (ABAQUS C3D8R) calculation using these material parameters are shown as solid lines in Fig. 3-1.

Let

$$\tilde{\gamma}^p \stackrel{\text{def}}{=} |\mathbf{D}_0^p| \tag{3.1}$$

define an equivalent plastic shear strain-rate, and

$$\gamma^p(t) \stackrel{\text{def}}{=} \int_0^t \tilde{\gamma}^p(\chi)\, d\chi, \tag{3.2}$$

define an equivalent plastic shear strain. Then, as a *simple* model for fracture by shear localization, we introduce a damage variable d whose value is zero for γ^p less than a critical value γ_c^p, and thereafter $d = (\gamma^p - \gamma_c^p)/(\gamma_f^p - \gamma_c^p)$, so that the damage variable evolves linearly towards a value of unity as γ^p evolves to a failure value γ_f^p. Correspondingly, the cohesion c is decreased linearly towards a value of zero. When the cohesion vanishes (i.e. damage goes to unity) in a given element, the material is deemed to have "failed", and it is "removed" from the finite element calculation. The stress-strain curves in tension and compression obtained from a *single finite-element* (ABAQUS C3D8R) calculation using the same material parameter as before, but with $\gamma_c^p = 0.05$ and $\gamma_f^p = 0.15$, are shown as dashed lines in Fig. 3-1. We recognize that γ_c^p and γ_f^p may be substantially higher in compression than in tension, but here, for simplicity, we shall use the same values for these two parameters. Much work remains to be done in developing more realistic models for the transition from shear localization to actual fracture.

3.2 Tension and compression of a metallic glass

A cylindrical specimen of a height-to-diameter ratio of 2:1 was modelled using 11,136 ABAQUS-C3D8R three-dimensional elements. A few elements in the center of the specimen were given a slightly lower initial value of cohesion (935 MPa) to serve as a nucleation site for shear localization. Fig. 3-2 shows the overall *engineering* stress-strain curve in tension; the peak-stress has a value of 1.84 GPa, and it occurs at a macroscopic strain of 1.98%. The figure also shows contour plots of the equivalent plastic strain in the vicinity of the peak, and at final failure. Failure occurs by localization of the plastic strain into a shear band. Fig. 3-3 shows the overall engineering stress-strain curve in compression (absolute values). In this case the peak-stress has a value of 2.09 GPa, and it occurs at a macroscopic strain of 2.16%. Due to the pressure sensitivity of plastic flow, the peak stress is higher in compression than in tension. There is some additional post-peak inelastic deformation to a strain of 2.85%, at which point a dominant shear band forms, and final failure occurs almost immediately thereafter.

The three-dimensional tension and compression calculations involve a reasonably coarse mesh. Since the essential features of the double-shearing mechanism are better revealed in two-dimensional plane-strain calculations, we repeated the tension and compression simulations using a mesh of 5,000 ABAQUS-CPE4R plane-strain elements, Fig. 3-4 (a). In this case the initial cohesion was statistically varied in *every* element using a Gaussian distribution with a mean value of 960 MPa, and a standard deviation of 8 MPa; Fig. 3-4 (b). Fig. 3-5 shows the overall engineering stress-strain curve in tension; in this case the peak-stress has a value of 1.81 GPa, and it occurs at a macroscopic strain of 1.68%. The figure also shows contour plots of the equivalent plastic strain in the vicinity of the peak, and at final failure. From this two-dimensional calculation it is clear that shear localization and failure can occur in multiple pairs of conjugate shear bands, with the location of the bands controlled by the *initial heterogeneity* in the specimen. Fig. 3-6 shows the overall engineering stress-strain curve in plane-strain compression (absolute values). In this case the peak-stress has a value of 2.10 GPa, and it occurs at a macroscopic strain of 1.89%. Thereafter,

additional inelastic deformation occurs with an overall slight strain-softening. The contour levels of the equivalent plastic strain prior to final failure clearly show that inelastic deformation occurs by a "double-shearing"-mechanism, and it is quite heterogeneous because of the initial heterogeneity in the cohesion. Finally, at an overall strain of 2.19% a dominant shear band develops, and final failure occurs almost immediately thereafter within this shear band.

As recently reviewed by Zhang et al. (2003), for a wide variety of metallic glasses under compressive loads, fracture along localized shear bands occurs at a fracture angle $\theta_C \approx 42^\circ$ between the compressive axis and the shear-fracture plane, while under tensile loads the fracture angle between the tensile axis and the shear-fracture plane, θ_T, is in the range $50 - 65^\circ$. Our simulation results, Fig. 3-5 and Fig. 3-6, show that our model, with the assumed values of the material parameters, predicts $\theta_T \approx 50^\circ$ and $\theta_C \approx 42^\circ$, which is in the right range for metallic glasses. As noted previously, the shear fracture plane orientation is determined not only by the internal friction parameter μ, but also by the dilatancy parameter β. The differing values of g_0, and hence the dilatancy parameter β, used in our simulations are crucial in providing an explanation for the differing values of the predicted shear-band orientations in tension and compression. This fact has long been known (cf., e.g., Rudnicki and Rice, 1975; Anand and Spitzig, 1982), but seems to have escaped the notice of many recent investigators conducting research on metallic glasses.

3.3 Bending of a strip

Since the yield strength in tension is smaller than that in compression due to pressure-sensitivity effects, and since the shear band orientations in tension and compression are also different, we expect that the response of a metallic glass to bending should also show evidence of a tension-compression asymmetry. We have conducted a simulation of plane-strain bending of a strip of a metallic glass. In this simulation, to better observe the characteristics of the shear-band asymmetries, we *suppress failure*. As shown schematically in Fig. 3-7 (a) the strip is clamped between a pair of rigid dies, and then a rigid mandrel is moved upwards to bend the strip about the nose-radius of

the upper die. The simulation was carried out using frictionless conditions between the strip and the dies/mandrel. The complete plastically deformed strip is shown in Fig. 3-7 (b), while Fig. 3-7 (c) shows a magnified image of a section of the deformed strip. As is clear, the shear bands on the tension side of the sample extend farther into the sample than do those on the compression side, and the shear strains in the bands on the tension side are also much higher. The shear band pattern observed in the simulation is very similar to that which is observed by Conner et al. (2003) in their experiments; their Fig. 1.

3.4 Plane-strain wedge indentation

Indentation testing has long been used to study the mechanical properties of metallic glasses, and Schuh and Nieh (2004) have recently reviewed the literature. Shear bands have been observed on the surface around indents in metallic glasses for quite some time, and recent studies have improved the resolution of these observations by using atomic force microscopy (AFM). A typical AFM micrograph of a Berkovich indent in a Zr-based bulk metallic glass is shown in Fig. 1 of Kim et al. (2002), where a number of shear bands can be observed in the piled-up area surrounding the indenter. In addition to examination of the surface around an indentation, there are a few experimental studies that have experimentally studied the plastic flow field beneath the indenter (cf., e.g., Donovan, 1989; Jana et al., 2003). A nice photograph of the shear band pattern underneath a Vickers indenter is that in Fig. 4 of Jana et al. (2003). Schuh and Nieh (2004) have noted the qualitative similarity of the shear-band patterns observed in these experiments to the classical slip-line field of Hill (1950) for a rigid-perfectly-plastic material indented in plane-strain by a wedge.

We have conducted a simulation of plane-strain wedge indentation of a metallic glass. As before, to better observe the shear-band patterns beneath the indenter, we suppressed failure in the simulation. The initial value of cohesion was given the same statistical variation as in the previous calculations; cf. Fig. 3-4 (b). Fig. 3-8 (a) shows the finite element mesh and indenter geometry. The mesh consists of 25,458 ABAQUS-CPE4R plane strain elements; the mesh density under the indenter

is much higher than elsewhere. To approximate a Vickers indenter, the wedge half-angle is chosen to be 68°. Fig. 3-8 (b), a magnified image of the indented region under the tip, shows contours of the equivalent plastic shear strain. The figure reveals a complex shear-band pattern with two sets of dominant curved shear bands: one set of curved shear bands is directed towards the interior of the specimen, while another set intersects the free-surface to produce slip-steps. Our simulations reveal that during the initial stages of indentation, the shear bands that form are mainly the ones that are directed towards the interior of the specimen; the ones that intersect the free-surface appear during a much later stage of the indentation process. The slight asymmetry in the shear-band pattern in Fig. 3-8 (b) is related to the initial distribution of the value of cohesion.[2]

Fig. 3-9 shows a curve of the indentation load per unit thickness, P, versus the indentation depth, h.[3] Our simulations indicate that the numerous "ripples" and "load-drops" in the early stage of the $P - h$ curve are related to the formation of numerous shear bands that are directed towards the interior of the specimen; it is difficult to identify these early load drops with the formation of any particular shear band(s).[4] However, the distinct "load-drops" marked as events a, b, and c on the later stage of the $P - h$ curve, occur when the shear bands indicated by arrows in Fig. 3-9 (a), (b) and (c) intersect the free surface. As reviewed by Schuh and Nieh (2004), serrated $P - h$ curves are widely observed in experiments, where instead of "load-drops" one observes "displacement-bursts" or "pop-ins" because indentation experiments are typically carried out under load-control, while our indentation simulation was conducted under displacement-control.

[2]An asymmetrical pattern can also develop due to numerical noise which is invariably present in explicit-dynamic calculations. The numerical noise arises due to the use of mass-scaling to speed up quasi-static simulations.

[3]Note that our theory has no internal length scale, so the indentation depth and load per unit thickness are relative to the geometry and boundary conditions shown in Fig. 3-8 (a), in which we have used a micron as the unit of length.

[4]One has to be careful in the interpretation of such ripples. If a high value of mass-scaling is used, then the numerical noise in explicit-dynamic calculations gives rise to noisy reaction force curves. In our calculations we took care to ensure that any numerical noise was minimal.

3.5 Concluding remarks

We have formulated a three-dimensional elastic-viscoplastic constitutive model based on a "double-shearing" frictional and dilatant mechanism for plastic flow, and implemented it in a finite element program. A first step to use the model to represent the mechanical response of metallic glasses at low homologous temperatures has been taken, and the qualitative agreement of the results from numerical simulations with experimental results, is very encouraging. However, much work remains to be done to (a) accurately model the transition from strain localization to failure, and (b) to extend the model to describe the response of metallic glasses at high homologous temperatures.

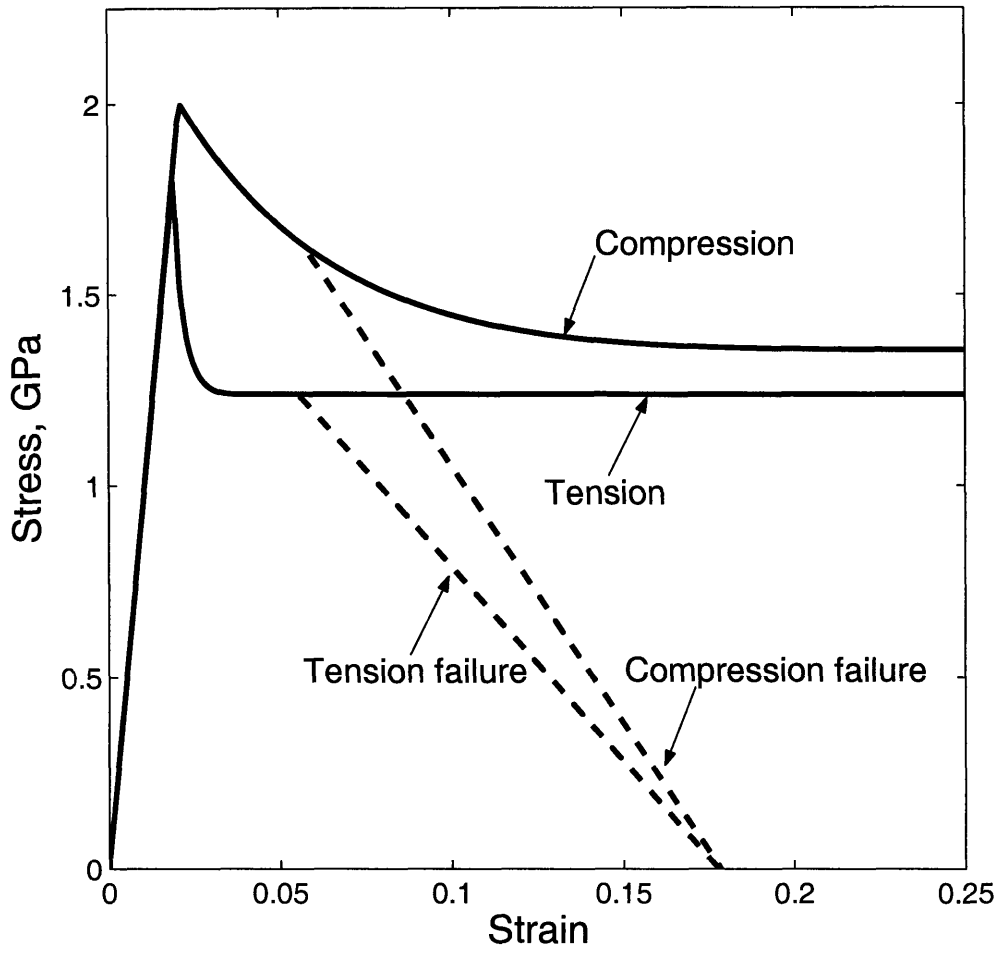

Figure 3-1: The solid lines show the stress-strain response in tension and compression (absolute values) for a zirconium-based metallic glass, based on the material parameters listed in §3.1. The dashed lines show the assumed stress-strain curves when modelling failure due to shear localization.

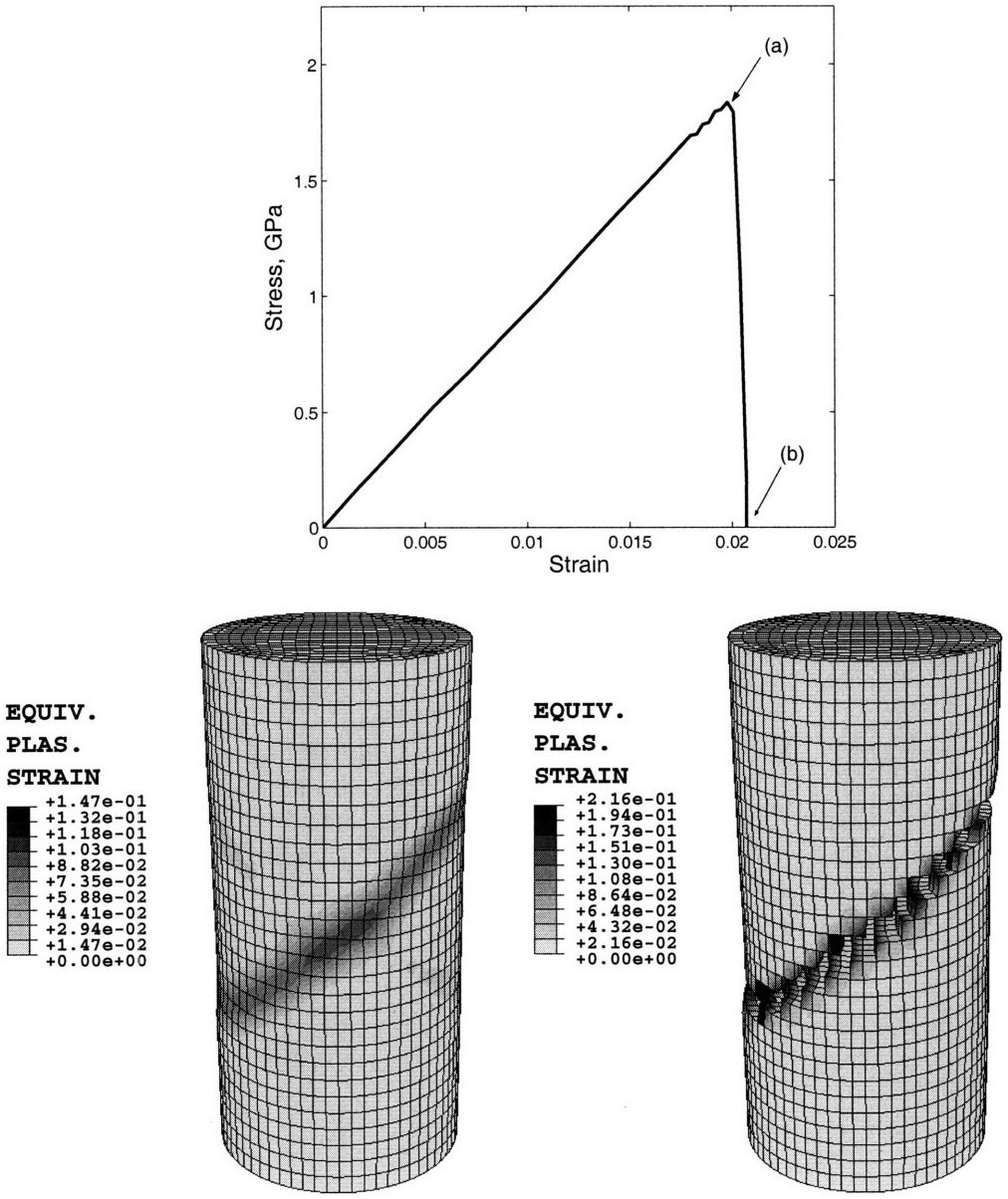

(a) (b)

Figure 3-2: Stress-strain curve from a three-dimensional tension simulation. Contour plots of the equivalent plastic strain keyed to two points on the stress-strain curve are also shown: (a) in the vicinity of the peak, and (b) at final failure.

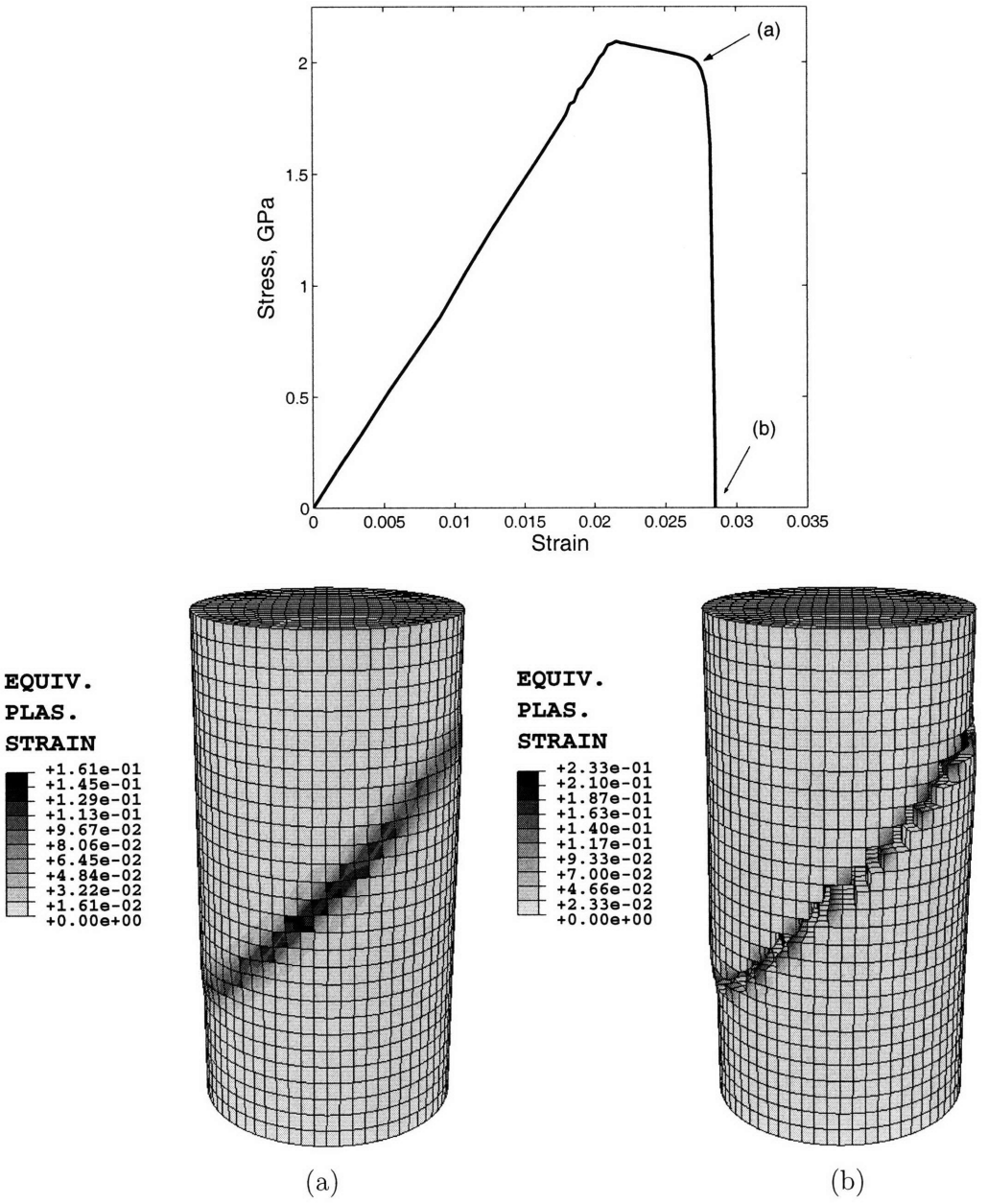

(a) (b)

Figure 3-3: Stress-strain curve from a three-dimensional compression simulation (absolute values). Contour plots of the equivalent plastic strain keyed to two points on the stress-strain curve are also shown: (a) in the vicinity of the peak, and (b) at final failure.

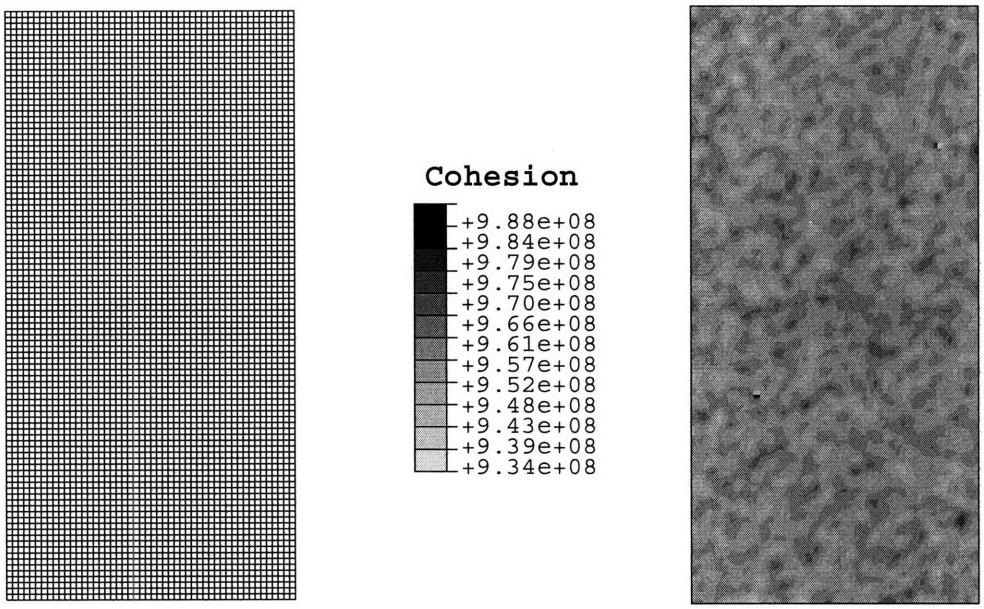

(a) (b)

Figure 3-4: (a) Finite element mesh consisting of 5000 ABAQUS-CPE4R elements for two-dimensional simulations of plane-strain tension and compression. (b) Contour plot of initial value of cohesion.

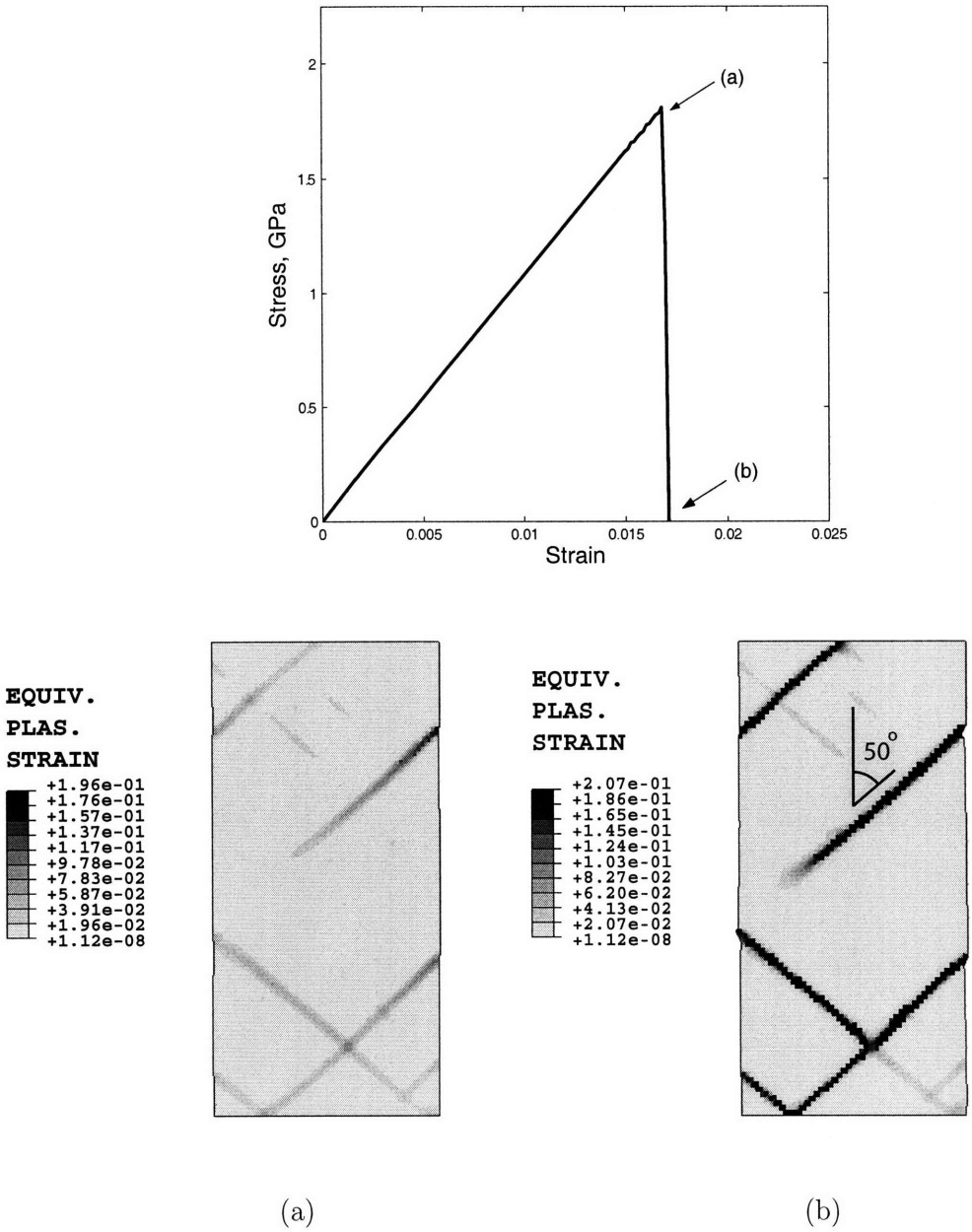

(a) (b)

Figure 3-5: Stress-strain curve from a two-dimensional plane-strain tension simulation. Contour plots of the equivalent plastic strain keyed to two points on the stress-strain curve are also shown: (a) in the vicinity of the peak, and (b) at final failure.

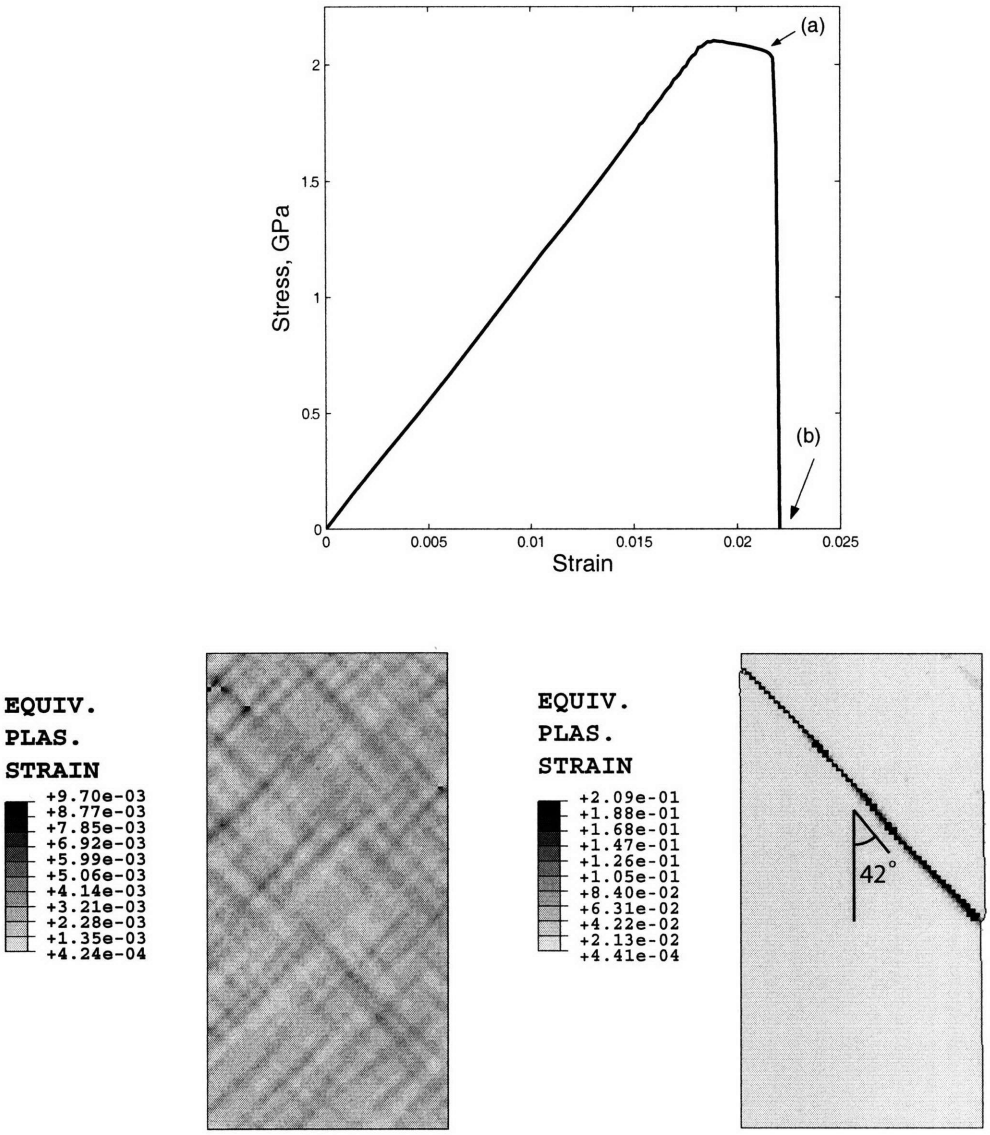

(a) (b)

Figure 3-6: Stress-strain curve from a two-dimensional plane-strain compression simulation (absolute values). Contour plots of the equivalent plastic strain keyed to two points on the stress-strain curve are also shown: (a) in the vicinity of the peak, and (b) at final failure.

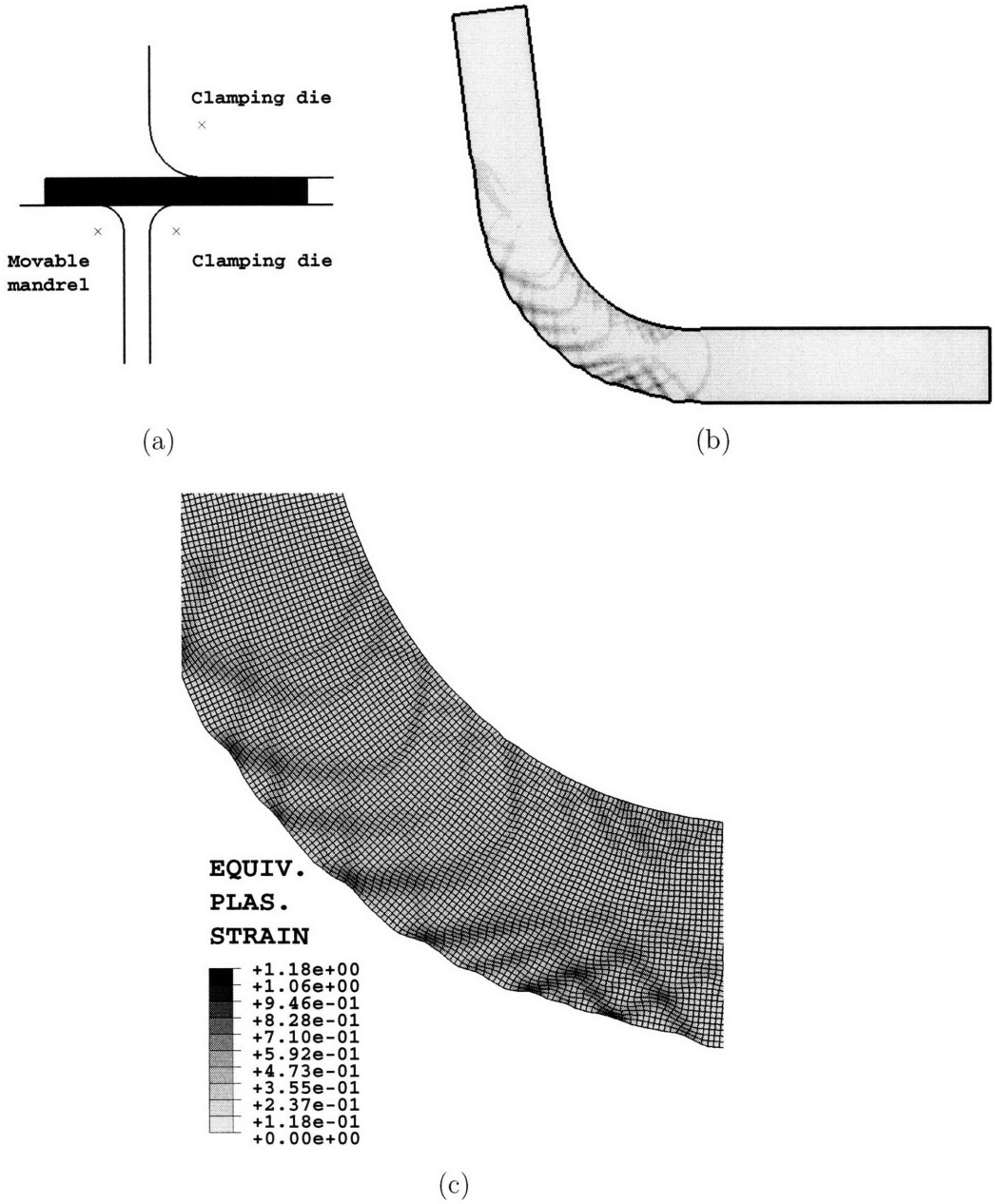

Figure 3-7: Simulation of bending of a strip of a metallic glass. (a) The strip is clamped between a pair of rigid dies, and then the rigid mandrel is moved upwards to bend the strip about the radius of the upper die. (b) Deformed strip showing shear bands in the plastically-deformed region (not to scale). (c) Magnified image of a portion of the strip showing contour plots of the equivalent plastic strain.

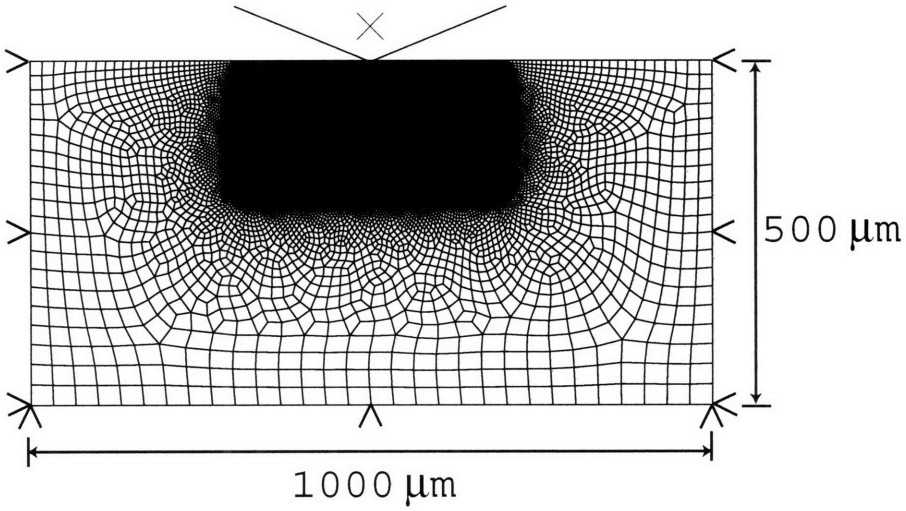

(a)

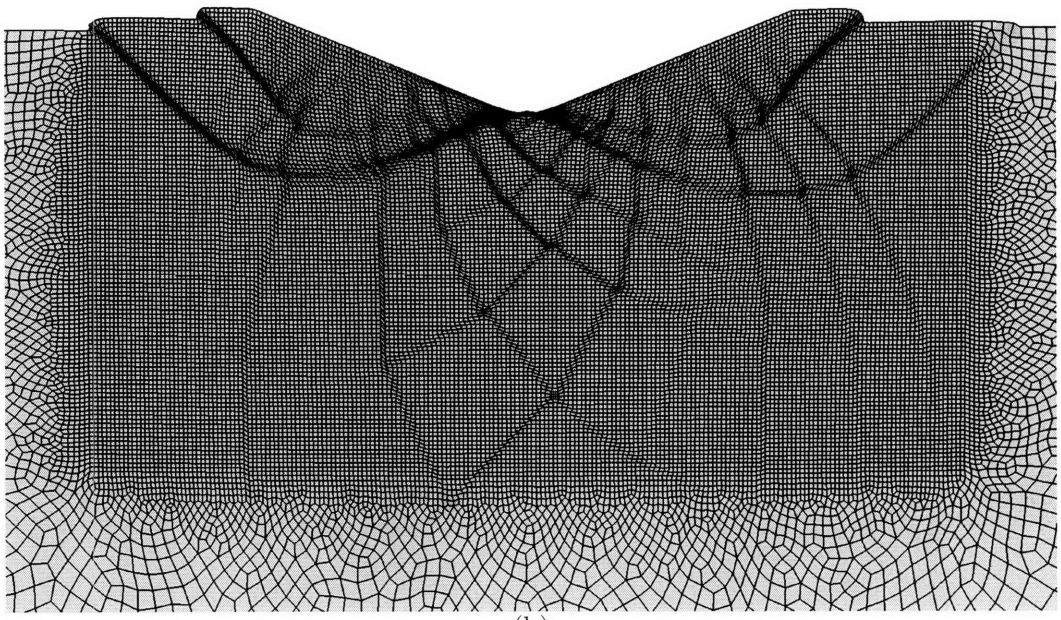

(b)

Figure 3-8: Simulation of plane-strain wedge indentation of a metallic glass. (a) The finite element mesh and indenter geometry. The mesh consists of 25,458 ABAQUS-CPE4R plane strain elements; the mesh density under the indenter is much higher than elsewhere. To approximate a Vickers indenter, the wedge half-angle is chosen to be 68°. (b) Magnified image of the indented region under the tip showing shear-bands (as evidenced by contour plots of the equivalent plastic strain).

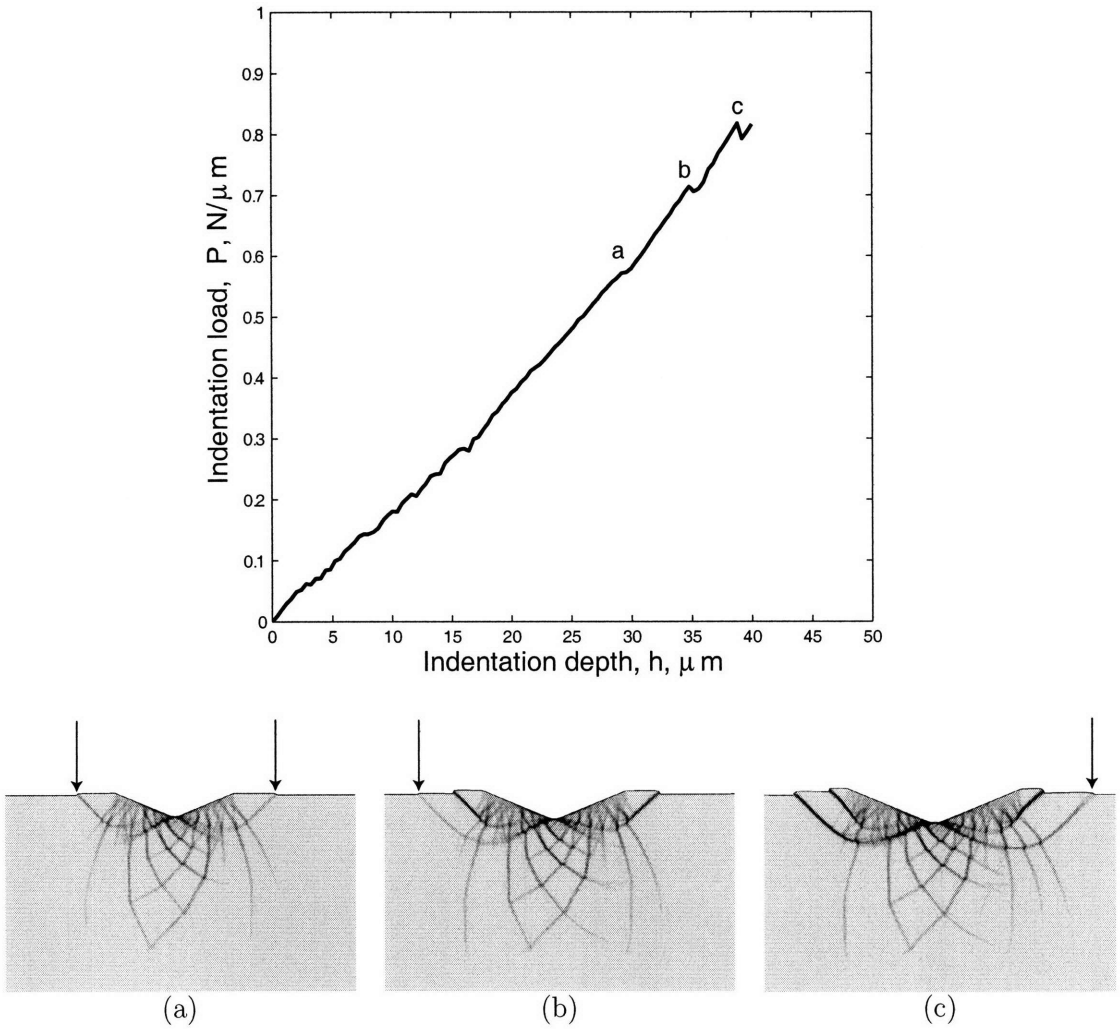

Figure 3-9: Indentation load per unit thickness P, versus indentation depth h (absolute values). Distinct "load-drops" marked as events a, b, and c on the $P - h$ curve, occur when the shear bands indicated by arrows in figures (a), (b) and (c) in the bottom panel intersect the free surface.

Chapter 4

Plane strain indentation of a Zr-based metallic glass: experiments and numerical simulation

The response of a Zr-based metallic glass in instrumented plane strain indentation with a cylindrical indenter tip is studied experimentally. A recently-developed constitutive model and simulation capability for metallic glasses is used to numerically calculate indentation load versus depth curves, and the evolution of corresponding shear-band patterns under the indenter. The numerical simulations are shown to compare very favorably against the corresponding experimental results.

4.1 Introduction

There is considerable current interest in studying and modelling the mechanical behavior of metallic glasses. When a metallic glass is deformed at ambient temperatures, well below its glass transition temperature, its inelastic deformation is characterized by strain-softening which results in the formation of intense localized shear bands; fracture typically occurs after very small inelastic strain in tension, but substantial

inelastic strain levels can be achieved under states of confined compression, such as in indentation experiments.

The micro-mechanisms of inelastic deformation in bulk metallic glasses are not related to dislocation-based mechanisms that characterize the plastic deformation of crystalline metals. The plastic deformation of amorphous metallic glasses is fundamentally different from that in crystalline solids because of the lack of long-range order in the atomic structure of these materials. The computer simulations of Argon and co-workers (cf., e.g., Deng et al., 1989) show that at a micromechanical level inelastic deformation in metallic glasses occurs by local shearing of clusters of atoms ($\approx$ 30 to 50 atoms), this shearing is accompanied by inelastic *dilatation* that produces strain-softening, which then leads to the formation of intense shear bands. An important consequence of the micro-mechanism of inelastic deformation in amorphous metals is that at the macroscopic level, experimentally-determined yield criteria for inelastic deformation are found not to obey the classical pressure-insensitive forms (Donovan, 1989; Bruck et al., 1993; Lewandowski and Lowhaphandu, 2002), but show a significant pressure sensitivity of plastic flow, which may be approximated by the Coulomb-Mohr yield criterion (Donovan, 1989; Lewandowski and Lowhaphandu, 2002). The recent molecular-dynamic simulations of Lund and Schuh (2003) indicate that the yield data from their atomistic simulations was also well-described by the Coulomb-Mohr yield criterion.

The Coulomb-Mohr yield condition is widely used in soil mechanics to determine the stress required for flow of a granular material. However, a suitable three-dimensional *flow rule*, that is the equation which governs the flow behavior for this class of materials, is more recent in origin (e.g., Spencer, 1964; Mehrabadi and Cowin, 1978; Nemat-Nasser et al., 1981; Anand, 1983; Anand and Gu, 2000).

In Chapter 2 we have generalized the rate-independent elastic-plastic constitutive model of Anand and Gu (2000) (originally developed for cohesionless granular materials) to formulate a thermodynamically-consistent, finite-deformation macroscopic theory for the *rate-dependent* elastic-viscoplastic deformation of pressure-sensitive, and plastically-dilatant materials. We have also implemented our new constitutive model in the finite element program ABAQUS/Explicit (2004) by writing a user ma-

terial subroutine. Using this numerical implementation of our model, in Chapter 3, we have simulated the response of a metallic glass in tension, compression, strip bending, and indentation, and shown that results from their numerical simulations qualitatively capture major features of corresponding results from physical experiments available in the literature.

The purpose of this chapter is to report on our own plane strain indentation experiments on a Zr-based bulk metallic glass. We have measured the corresponding macroscopic load (P) versus indentation depth (h) curves, and studied the evolution of the shear band patterns under the indenter. We shall show that the constitutive model and numerical simulation capability developed previously is capable of producing simulations that *quantitatively* compare very favorably against the corresponding experimental results.

Indentation testing has long been used to study the mechanical properties of metallic glasses, and Schuh and Nieh (2004) have recently reviewed the substantial literature. Shear bands have been observed on the surface around indents in metallic glasses for quite some time, and recent studies have improved the resolution of these observations by using atomic force microscopy (AFM). A typical AFM micrograph of a Berkovich indent in a Zr-based bulk metallic glass is shown in Fig. 1 of Kim et al. (2002), where a number of shear bands can be observed in the piled-up area surrounding the indenter. In addition to examination of the surface around an indentation, there are a few experimental studies that have experimentally studied the plastic flow field beneath the indenter (cf., e.g., Donovan, 1989; Jana et al., 2003, 2005; Zhang et al., 2005). A nice photograph of the shear band pattern underneath a Vickers indenter is that in Fig. 7 of Jana et al. (2005). The shear band patterns produced under a three-dimensional Vickers indent are *complex* and difficult to interpret. In this chapter we report on the results of a study of the evolution of shear band patterns under indents produced by an indenter with a *cylindrical-tip* under *plane strain* conditions. This is a much simpler geometry to study the evolution of inelastic deformation due to shear banding in an inhomogeneous deformation field. Another advantage of plane strain indentation is that — relative to full three-dimensional simulations — it is less time-consuming to perform numerical simulations in two-dimensions.

The plan of this chapter is as follows. We describe our experiments in §4.2. In §4.3 we use the data from macroscopic stress-strain tests and instrumented indentation test on our Zr-based metallic glass to estimate certain key material parameters appearing in the model, while the other material parameters in the model are estimated from experimental results available in the literature. Using these material parameters we compare how well the numerically calculated P-h curves and corresponding shear-band patterns under the indenter compare against the experimental results. We close in Section §4.4 with some final remarks.

4.2 Experiment procedures and results

A metallic glass with composition $Zr_{56.06}Cu_{23.39}Ni_{15.54}Ta_{2.27}Al_{1.62}Ti_{1.11}$ was used in this study.[1] We first conducted a simple compression experiment on this material. The compression specimen was a rectangular block that is 7.56 mm high, 5.70 mm wide, and 4.47 mm thick (into the plane of the paper), as shown in Fig. 4-1a. The experiment was conducted on an Instron 8501 servo-hydraulic testing machine in displacement control at a cross-head rate of 0.3 μm per second. A 100 kN load cell was used to measure the compressive force, while strain was measured locally on the specimen with an optical extensometer which tracks the displacements of two painted marks on the specimen surface with sub-micrometer accuracy; thus influence of machine compliance on strain measurement is eliminated. The material fails abruptly by shear localization at a stress level of 1.69 GPa. The shear fracture surface forms an angle of $\approx 42^\circ$ with the compression direction, Fig. 4-1b, which agrees well with typical values for Zr-based bulk metallic glasses reported in the literature (cf., e.g., Lewandowski and Lowhaphandu, 2002; Zhang et al., 2003). Fig. 4-1 c shows the resulting engineering stress-strain curve (solid line); absolute values of stress and strain are plotted. This curve gives a value of $E = 89$ GPa for the elastic Young's modulus of this metallic glass.

The indentation experiments were also conducted on our Instron 8501 servo-

[1]The authors gratefully acknowledge Professor Kenneth Vecchio of UCSD for providing the metallic glass.

hydraulic testing machine. For the indenter we used a constant thickness tungsten-carbide cutting tool, which is triangular in shape with a cylindrical tip. The thickness of the indenter, is 4.8 mm and its tip radius is 0.41 mm. The metallic glass to be indented is in the form of a flat plate of height 4.47 mm, width 15.24 mm, and thickness 9 mm, Fig. 4-2 a. A close-up of an end-view of the indenter and the specimen is shown in Fig. 4-2 b. Special care was exercised in fixturing of the specimen and the indenter in the testing machine to ensure that the indenter travel was perpendicular to the flat face of the specimen to be indented. A 100 kN load cell was used to measure the indentation force, while the indentation depth was measured with our optical extensometer which tracks the displacements of two painted marks, one painted on the indenter and the other near the bottom of the specimen, Fig. 4-2 b; as mentioned above our optical extensometer can measure indentation depths with sub-micrometer accuracy.[2] The indentation experiments were carried out under displacement control at a speed of 0.3 μm per second. Three separate indentation experiments were conducted to maximum forces levels of 5 kN, 7.5 kN, and 10 kN, followed by unloading. A typical surface trace of an indent is shown in Fig. 4-2 c. The indentation load (P) versus indentation depth (h) curves (solid lines) are shown in Fig. 4-2 d.

In order to study the evolution of shear bands under the indenter we conducted three additional indentation experiments to maximum forces levels of 5 kN, 7.5 kN, and 10 kN, as in the experiments described above. In this set of experiments the metallic glass specimens had a bonded interface, cf. Fig. 4-3 a, which was achieved by bonding two identical rectangular blocks of the material, with the contacting sides polished to a mirror-finish. The thickness of these composite specimens is 6.2 mm, which is slightly larger than the thickness of 4.8 mm for the indenter. As in the previous specimens, the height and the width of the specimens were 4.47 mm and

[2]Our indentation experiments are not quite plane strain, but approximate this condition. For true plane strain indentation, the indenting tool should be infinitely thick (into the plane of the paper), and the substrate should be an infinite half space, with no out-of-plane displacements. However, since the indenter used in our experiments has a thickness of 4.8 mm (into the plane of the paper) and this is impressed onto the middle of the specimen surface of thickness 9 mm (into the plane of the paper),the resulting indents have surface traces in the form rectangular impressions of length 4.8 mm and widths of the order of the tool tip radius of 0.41 mm; cf. Fig. 4-2 c. The indentation length is therefore much larger than the indentation width (a ratio of 11.7), and the whole indent is contained by a sufficiently large volume of undeformed material; our indentation experiments may therefore be considered to *approximate* plane strain indentation.

15.24 mm, respectively. In order to prevent the specimen form splitting along the bonded-interface during indentation, and also to ensure approximate plane strain conditions, two hardened tool steel blocks, each 26 mm thick, were used to restrict any out-of-plane movement.

After indenting a specimen to its maximum load (5 kN, 7.5 kN, or 10 kN), the specimen was unloaded, the adhesive bonding the two halves of each specimen was dissolved, and the polished surfaces under the indents were examined in an optical microscope for shear band patterns. The resulting optical photo-micrographs are shown in Fig. 4-3 b,c, and d. At 5 kN, observable shear bands have formed under the indenter. The groove left by the indenter on the material is barely discernable in this figure. The shear-band pattern has a (nearly) symmetrical spiral shape pointing towards the interior of the substrate, and appears to be most intense near the edge of the indentation mark. At 7.5 kN, substantially more shear bands have formed and penetrated deeper into the material, but they do not intersect with the free surface to form slip steps as is typically observed around the indenter in three-dimensional Berkovich or Vickers indentation experiments. As the load increases to 10 kN, the shear band pattern penetrates deeper into the specimen and becomes more pronounced; also a crack is seen to have initiated on the right edge of the surface indent. The slight asymmetry in the shear-band patterns under the indenter is probably due to a slight misalignment in the indentation experiment and/or slight variations in the material properties of the specimen.[3]

We have implemented our constitutive model in the finite-element computer program ABAQUS/Explicit (ABAQUS/Explicit, 2004) by writing a user material subroutine. Using this numerical capability, in the next section we explore how well numerically calculated P-h curves and corresponding shear-band patterns under the indenter compare against the corresponding experimental results reported in §4.2.

[3]After we had completed our experiments and numerical simulations, we have become aware of a recent paper by Antoniou et al. (2005) in which these authors have performed experiments and obtained results very similar to those reported in this paper. However, they have not performed any simulations similar to those reported here.

4.3 Simulations of plane strain indentation with a cylindrical tip

4.3.1 Material parameters for our Zr-based metallic glass

We have used the data from macroscopic compression test and instrumented indentation tests on our Zr-based metallic glass to estimate certain key material parameters appearing in the model, while the other material parameters in the model are estimated from experimental results available in the literature. The following specific values for the material parameters were chosen:

- *Elastic Moduli*: Our compression experiments gave a value of $E = 89\,\text{GPa}$, and for the Poisson's ratio we use a value of $\nu = 0.36$ reported in (Lu et al., 2003) for Zr-based metallic glasses, we obtain

  $$G = 32.7\,\text{GPa} \quad \text{and} \quad K = 106\,\text{GPa},$$

  for the shear and bulk moduli, respectively. For simplicity we assume that the effect of the very small plastic volume change (see below) on the elastic moduli of amorphous metals is negligible.

- *Friction coefficient*: For the internal friction coefficient we take

  $$\mu = 0.04$$

  which has been estimated in (Lewandowski and Lowhaphandu, 2002) for Zr-based metallic glasses.

- *Viscoplasticity parameters*: The glass transition temperature of Zr-based metallic glasses is $\approx 625\,\text{K}$, and under room temperature conditions $\approx 300\,\text{K}$, the mechanical response of these materials is observed to be *almost rate-insensitive.* The low value of the strain-rate sensitivity parameter

  $$m = 0.005,$$

is chosen to model such a nearly rate-independent response. The reference shearing rate is taken to be

$$\nu_0 = 0.001\,\mathrm{s}^{-1}.$$

- *Plastic volume change*: Recall that,

$$\dot{\eta} = \beta\nu, \qquad \beta = g_0\Big(1 - \frac{\eta}{\eta_{cv}}\Big)^p.$$

Density measurements in metallic glasses show that the *overall* maximum density reduction as a result of plastic deformation is approximately $0.15 - 0.25\%$ (Deng and Lu, 1983; Cahn et al., 1984; Argon, 1993). However, experiments are inconclusive about the *maximum* amount of dilatation *in fully developed shear bands*; here we assume this maximum to be a small number, $\eta_{cv} = 0.005$, which is twice the value indicated by the overall density reduction. Concerning the parameter g_0 , which controls the *initial rate of dilatancy*, we expect (on physical grounds) that this initial rate of dilatation can be much higher in tension than in compression. Accordingly, based on experience with our previous study (Anand and Su, 2005), we assume that $g_0 = 0.04$ in compression, while it has a value ten times higher, $g_0 = 0.4$, in tension. *The total amount of dilatation can also possibly be higher in tension than in compression, but the experimental evidence is weak here.* The parameter p simply controls how quickly η approaches η_{cv}, and is here taken as $p = 0.5$. Summarizing, we assume that

$$g_0 = 0.04 \text{ in compression}, \quad 0.4 \text{ in tension}$$
$$\eta_{cv} = 0.005, \quad p = 0.5$$

The differing values of g_0, and hence the dilatancy parameter β, were found by Anand and Su (Anand and Su, 2005) to be crucial in providing an explanation for the differing values of shear-band orientations in tension and compression.

- *Cohesion function*: Recall that

$$c = c_{cv} + b\left(1 - \frac{\eta}{\eta_{cv}}\right)^q, \qquad c_0 \equiv c(0) = c_{cv} + b\,.$$

The initial value of the cohesion, c_0 (shear resistance), controls the stress level at which the material starts to deform plastically. This is estimated from our compression test to be

$$c_0 = 820\,\text{MPa},$$

which, upon allowing for the pressure-sensitivity of plastic flow, is slightly less than approximately half the compressive yield strength of 1.69 GPa measured in the compression experiment.

The other parameters c_{cv}, b, and q were estimated by carrying out numerical simulations of our plane strain indentation experiments and adjusting the values of these parameters to obtain a reasonable match of the experimentally-measured P-h curves shown in Fig. 4-2 d. This curve fitting procedure gives

$$c_{cv} = 750\,\text{MPa}, \quad b = 70\,\text{MPa}, \quad q = 2\,.$$

The reasonably acceptable quality of the curve-fit is shown in Fig. 4-2 d, where the numerically calculated P-h curves (dashed lines) are compared with experimentally-measured P-h curves (solid lines).

In the indentation simulations, the substrate was modelled by a finite element mesh consisting of 27,665 ABAQUS-CPE4R plain strain elements, and the indenter was modelled as an appropriately-shaped rigid surface with a tip-radius of 0.41 mm, Fig. 4-4 a; contact between the indenter and the substrate was approximated to be *frictionless* in the simulations.

Let

$$\tilde{\gamma}^p \stackrel{\text{def}}{=} |\mathbf{D}_0^p| \tag{4.1}$$

define an equivalent plastic shear strain-rate, and

$$\gamma^p(t) \stackrel{\text{def}}{=} \int_0^t \tilde{\gamma}^p(\chi)\, d\chi, \tag{4.2}$$

define an equivalent plastic shear strain. Contour plots of the equivalent plastic shear strain after unloading for the 10 kN indent are shown in Fig. 4-4 b. The asymmetry in the plastic strain pattern observable in Fig. 4-4 b is due to numerical noise which is invariably present in explicit-dynamic calculations. The numerical noise arises due to the use of mass-scaling to speed up quasi-static simulations.

The numerically-calculated stress-strain curve in compression using a single element (ABAQUS C3D8R) with the material parameters listed above is shown as a dashed line in Fig. 4-1 c. The initial linear elastic portion and the yield strength in the simulation agree well with the experimental result. The softening portion of the this curve is of course, because of the shear localization and fracture in the unconfined compression experiment, not experimentally accessible.

4.3.2 Shear band patterns under the indenter

Contour plots of the equivalent plastic shear strain after unloading for the 5 kN, 7.5 kN, and 10 kN cases are compared against the corresponding micrographs showing experimentally observed shear band patterns under the indenter in Fig. 4-3. For a better comparison, Fig. 4-5 shows the numerically-calculated plastic strain profile superposed on the experimental micrograph of the shear-band patterns for the 10 kN case. The extent and general shapes of the numerical and experimental inelastic deformation fields are remarkably similar. Also the site having the highest plastic strain in the numerical simulation is where the crack appears to have initiated in the experiment. It is fortuitous that the slight asymmetry caused by the numerical noise in the calculation is in the same direction as the asymmetry observed in the experiments!

Concerning the orientation of the shear bands under the indenter, Fig. 4-6 a shows a higher magnification SEM image of a portion of the inelastically deforming region under the indenter for the 10 kN indent. Focussing on a central region of this mi-

crograph, Fig. 4-6 b shows that the shear bands intersect forming an acute angle of $\approx 84°$. A plot of the equivalent plastic strain contours of the same region under the indenter from the numerical simulation is shown in Fig. 4-6 c; the angle between two intersecting numerically-predicted shear bands is essentially identical to the experimentally-measured angle shown in Fig. 4-6 b.

The shear bands in the numerical simulations are of course not as sharp and distinct as in the experiments. Our theory is local, it does not contain any material length scales, and in such cases (as is well-known) the deformation in a simulation localizes to the width of a typical element dimension. Consequently, the sharpest shear band that can be represented by the numerical simulation will have a width of the same order as the edge length of an element. Although we used more than twenty-seven thousands elements and have a relatively dense mesh under the indenter, cf. Fig. 4-4 b, the smallest element edge length is still $8\,\mu$m, which is considerably larger than the typical shear band width of $< 1\,\mu$m. A denser mesh would of course give finer numerically-calculated shear bands.

A technical point worth noting in Fig. 4-3 is that it appears that shear bands *do not* first appear *on the symmetry axis at a finite distance beneath the indenter*, where, according to a two-dimensional elastic Hertzian-analysis, the highest shear stress occurs (Johnson, 1999; Gouldstone et at., 2001). A more detailed examination of our numerical simulations, reveals that indeed the very beginnings of inelastic deformation does occur in the vicinity of such high shear stress location, as shown in Fig. 4-7. However, as soon as the material starts to deform plastically, the stress distribution under the indenter changes. The accumulated plastic shear strain at this initiating site remains small, and the location of the highest inelastic shearing rates shifts to other sites. Fig. 4-8 shows the contour plots of Tresca stress ($(1/2)(\sigma_1 - \sigma_3)$), mean normal pressure ($-(1/3)\mathrm{tr}\,\boldsymbol{\Sigma}$), and plastic work rate ($\boldsymbol{\Sigma} \cdot \mathbf{D}^p$) at a load level of 5 kN from the numerical simulation. The location of the highest Tresca stress is still in the center under the indenter, but the Tresca stress slightly offset from the center is also quite high. The central region right below the indenter has the highest pressure level, which also results in high compressive tractions on the local slip systems. It is this high compressive traction on the slip systems that results in a diminished plastic

flow rate and therefore inelastic dissipation rate directly under the indenter, and the highest inelastic dissipation rate occurs at the edges of indent, as is clearly shown by the plastic work rate contours in Fig. 4-8c.

4.4 Concluding remarks

The response of a Zr-based bulk metallic glass in (approximate) plane strain indentation with a cylindrical indenter tip has been experimentally investigated. Indentation load versus indentation depth curves were measured, and a bonded-interface technique was used to study the evolution of the shear band patterns under the indenter. By judiciously using experimental results available in the literature as well as our own experiments, we have estimated the material parameters appearing in our constitutive model. Using these material parameters we have compared the numerically calculated shear-band patterns under the indenter against the corresponding experimental results. Our results clearly show that our continuum constitutive model and numerical simulation procedures are capable of not only quantitatively matching the experimentally-measured P-h curves, but also capable of approximately matching the experimentally-observed inelastic strain-distribution and its evolution during indentation.

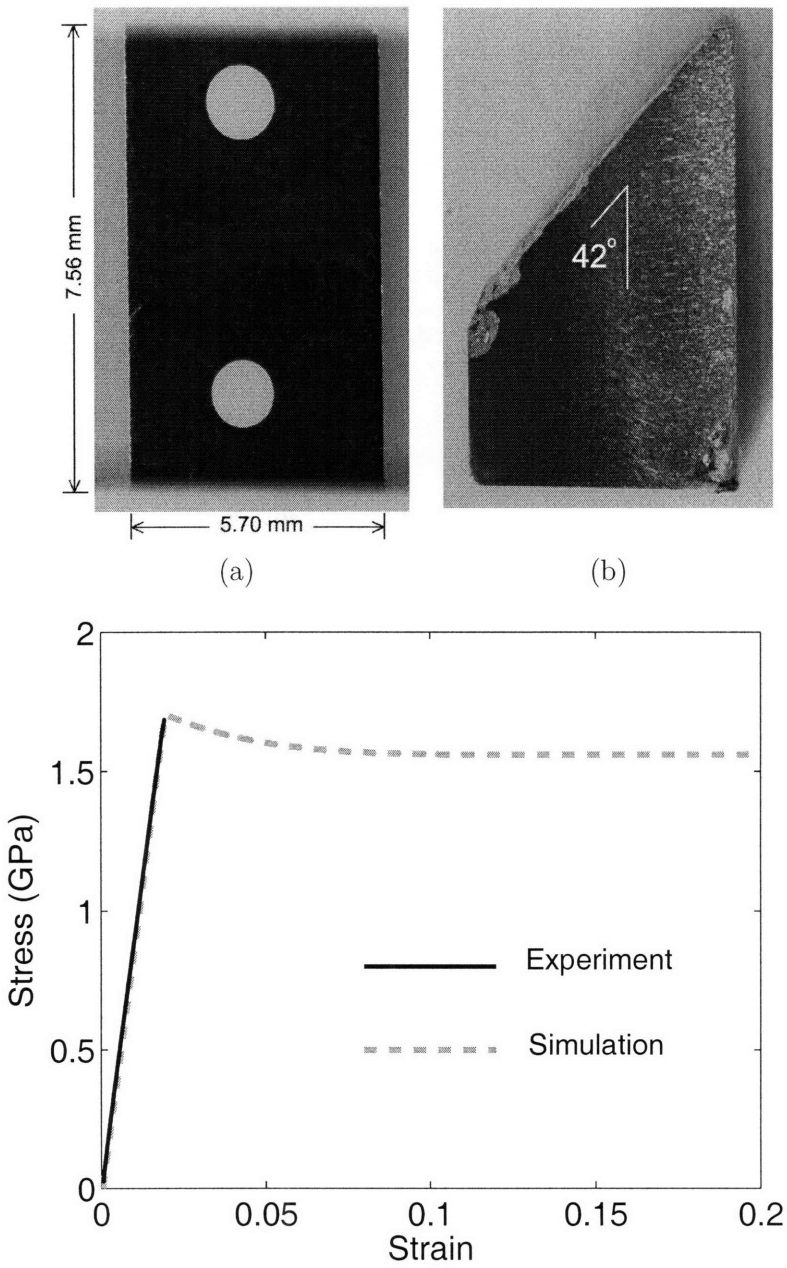

Figure 4-1: Simple compression experiment on a Zr-based metallic glass. (a) Specimen between compression platens; the two painted dots were used as markers for an optical strain measurement system. (b) One-half of the fractured specimen. (c) The experimentally-measured stress-strain curve is shown as the solid line. The underlying strain-softening stress-strain curve used in the indentation simulations is shown as the dashed line.

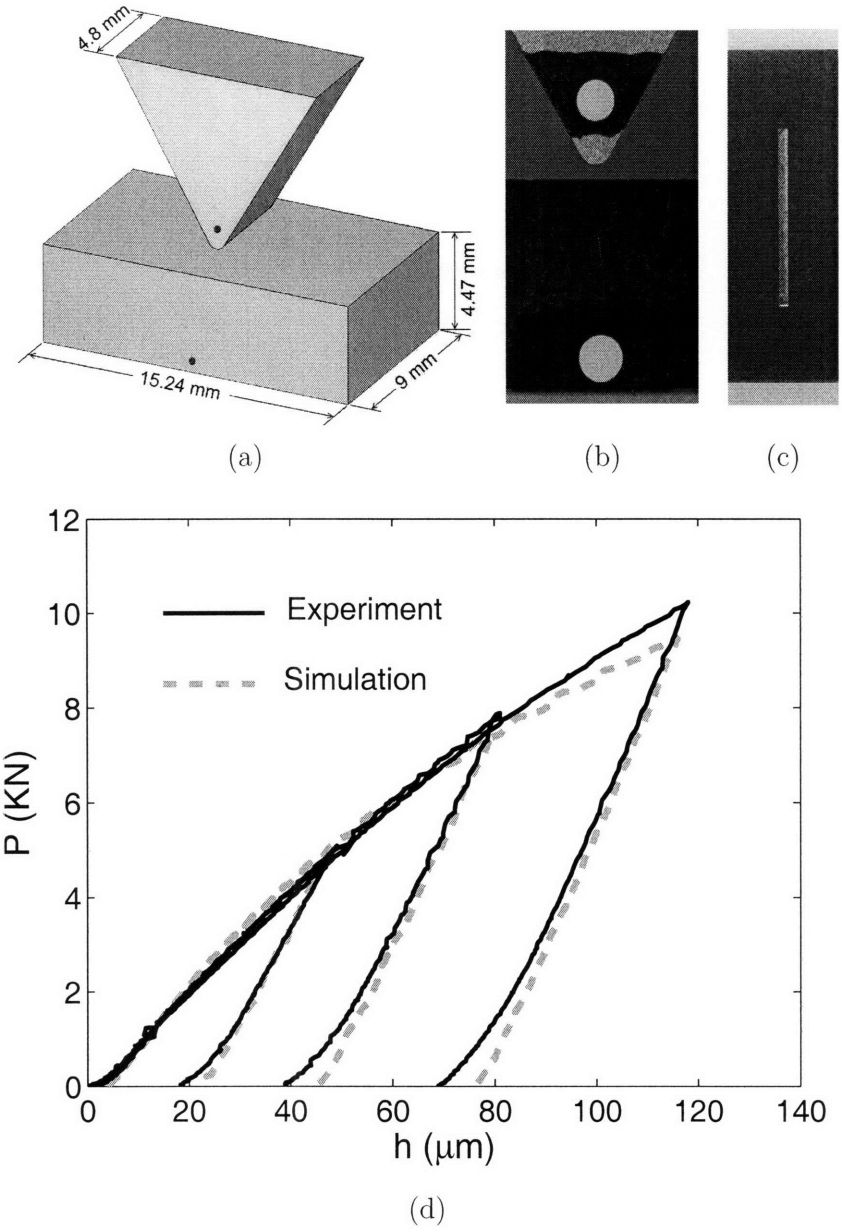

Figure 4-2: (a) Schematic of the plane-strain indentation experiment. (b) Front-view of the indenter and the substrate; the two painted dots were used as markers for an optical indentation depth measurement system. (c) Rectangular impression left on the surface after indentation. (d) Experimentally-measured P-h curves to load levels of 5 kN, 7.5 kN, and 10 kN are shown as solid lines. The numerically-calculated curves are shown as the dashed lines

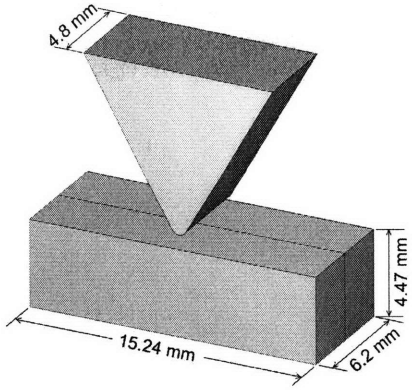

(a)

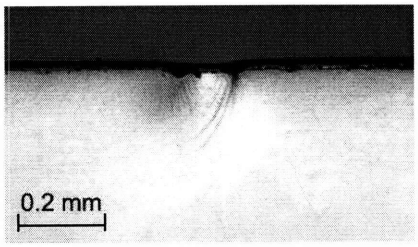

(b) 5 kN experiment

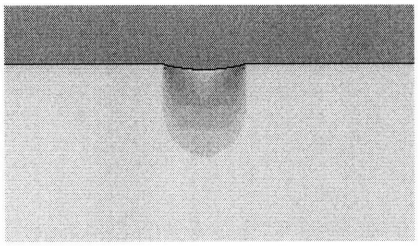

(e) 5 kN simulation

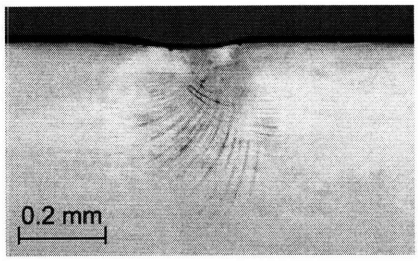

(c) 7.5 kN experiment

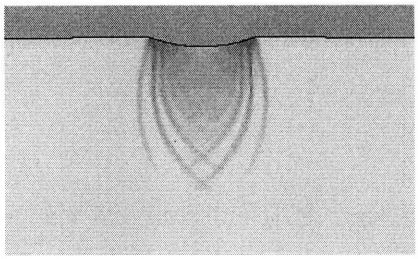

(f) 7.5 kN simulation

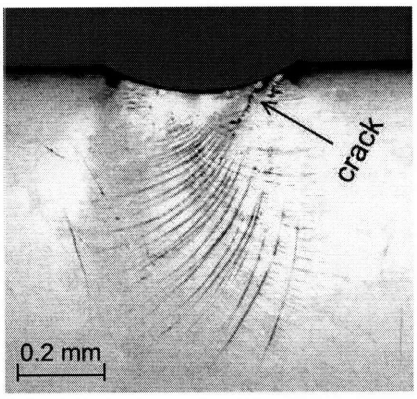

(d) 10 kN experiment

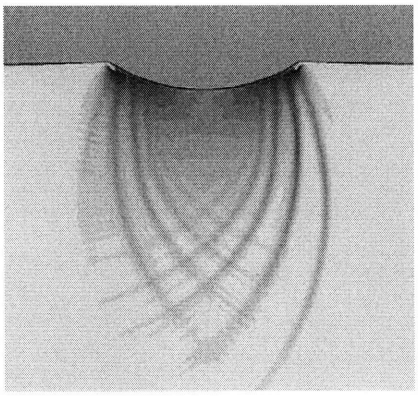

(g) 10 kN simulation

Figure 4-3: (a) Schematic of an indentation experiment on a specimen with a bonded-interface. (b, c, d) Optical micrographs of shear band patterns under the indenter after unloading from load levels of 5 kN, 7.5 kN, and 10 kN. (e, f, g) Corresponding numerical simulations showing contour plots of the equivalent plastic shear strain.

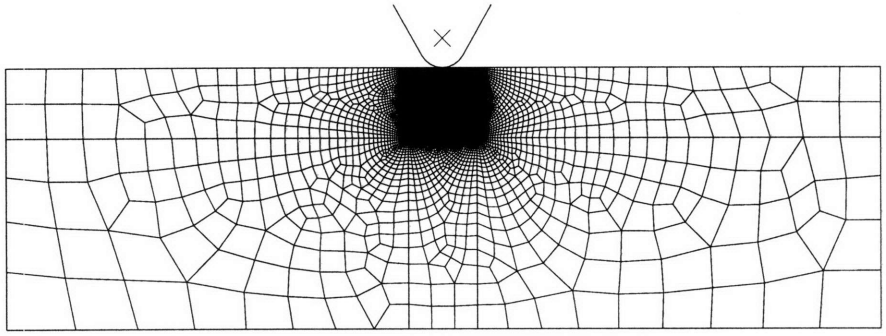

(a)

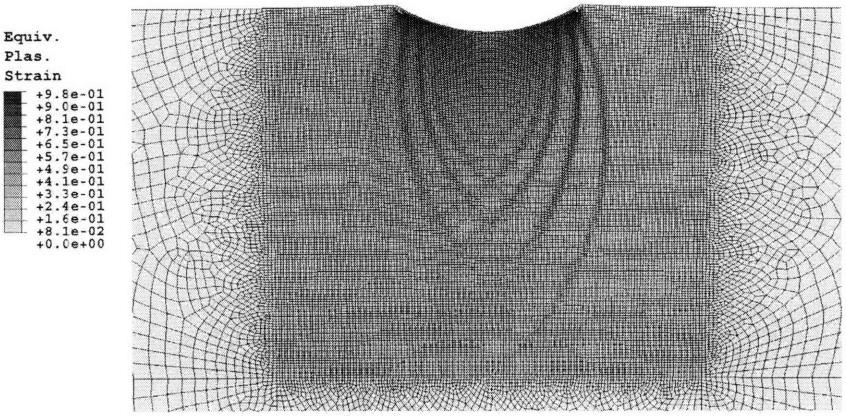

(b)

Figure 4-4: (a) Initial finite element mesh for the plane strain indentation simulation. The region of the mesh under the indenter appears black because it has a much higher mesh density. (b) A magnified image of the area under the indenter in the deformed mesh after unloading from a 10 kN simulation. A contour plot of the equivalent plastic shear strain is also shown on this deformed mesh.

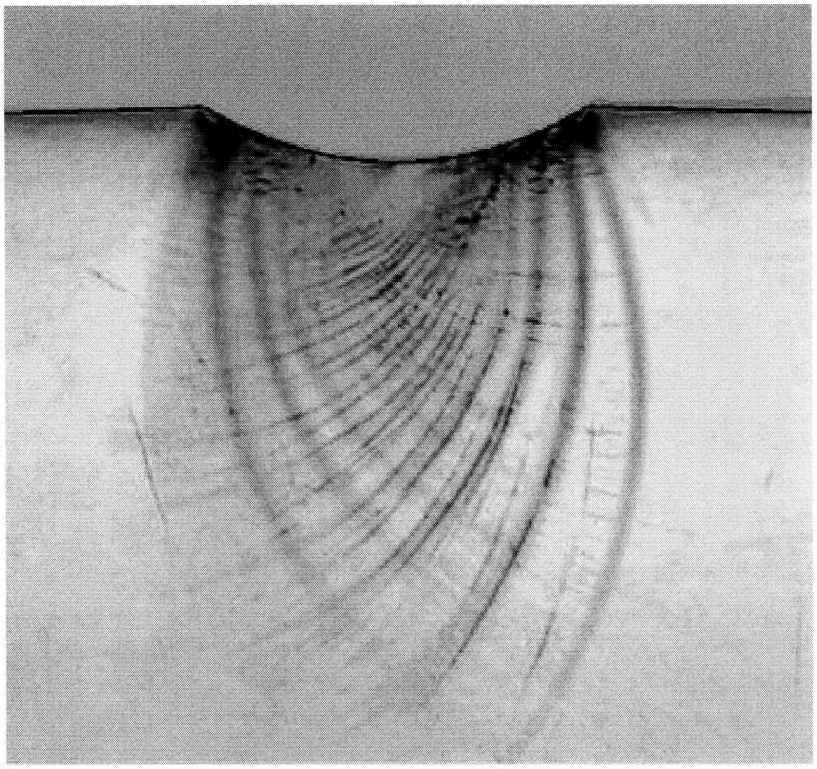

Figure 4-5: Superposition of the contour plot for the equivalent plastic shear strain on the corresponding experimentally-observed shear band pattern under the indenter for the 10 kN indentation.

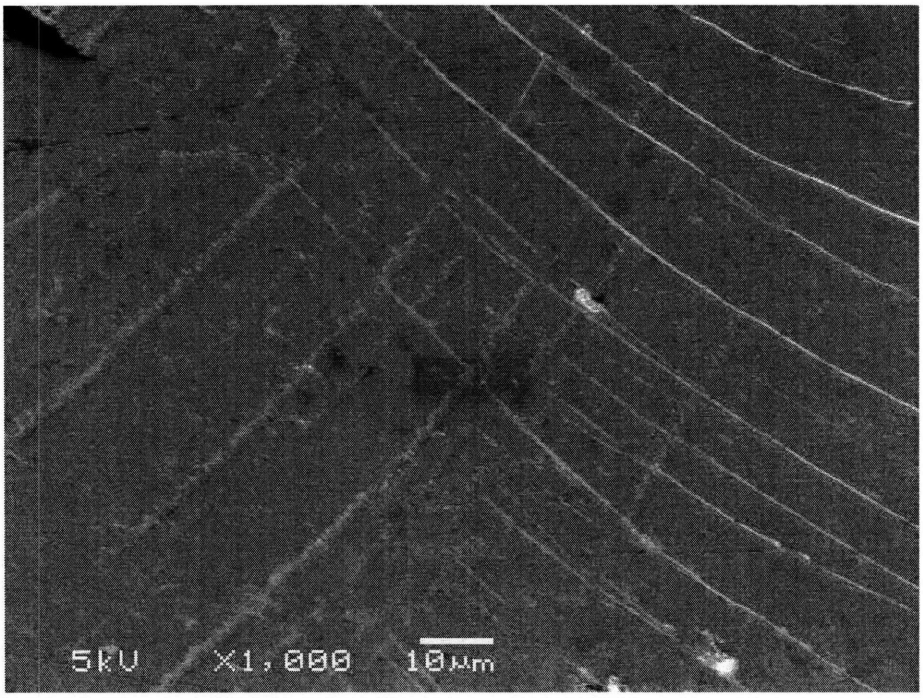

(a)

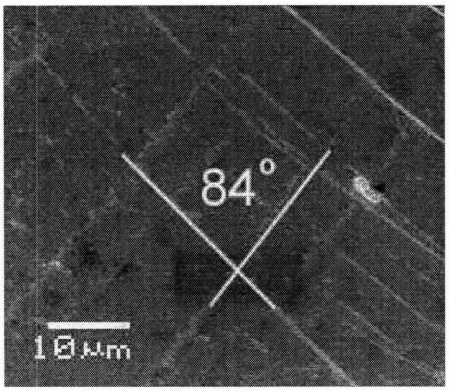

(b)

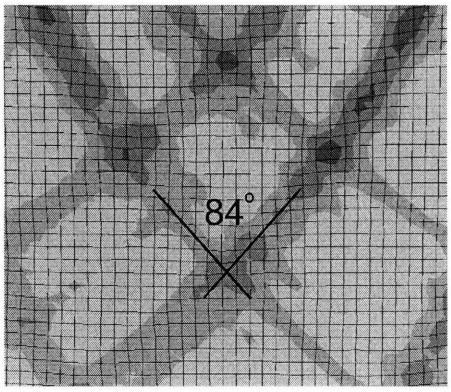

(c)

Figure 4-6: (a) SEM image of intersecting shear bands under the indenter; (b) the angle between two intersecting shear bands is $\approx 84°$; (c) contour plot of the equivalent plastic strain from the numerical simulation gives essentially the same angle between two intersecting shear bands.

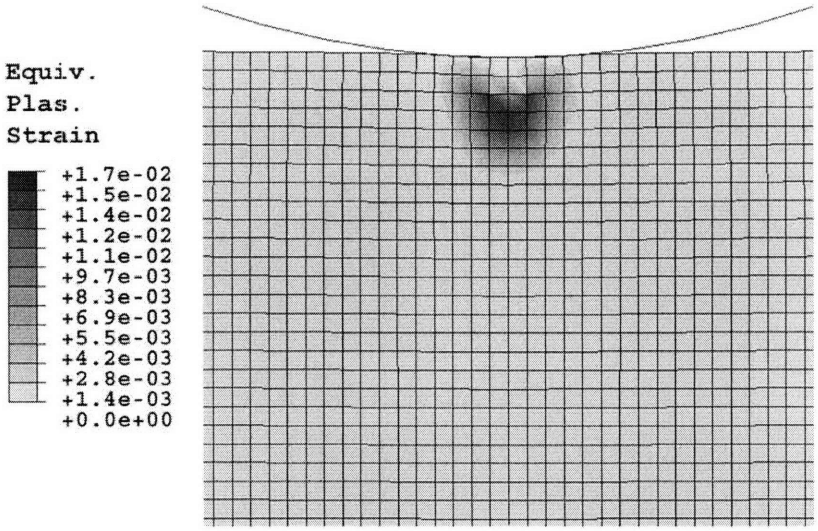

Figure 4-7: Contour plot of the equivalent plastic shear strain under the cylindrical indenter showing that plastic flow first takes place at a finite distance beneath the indenter.

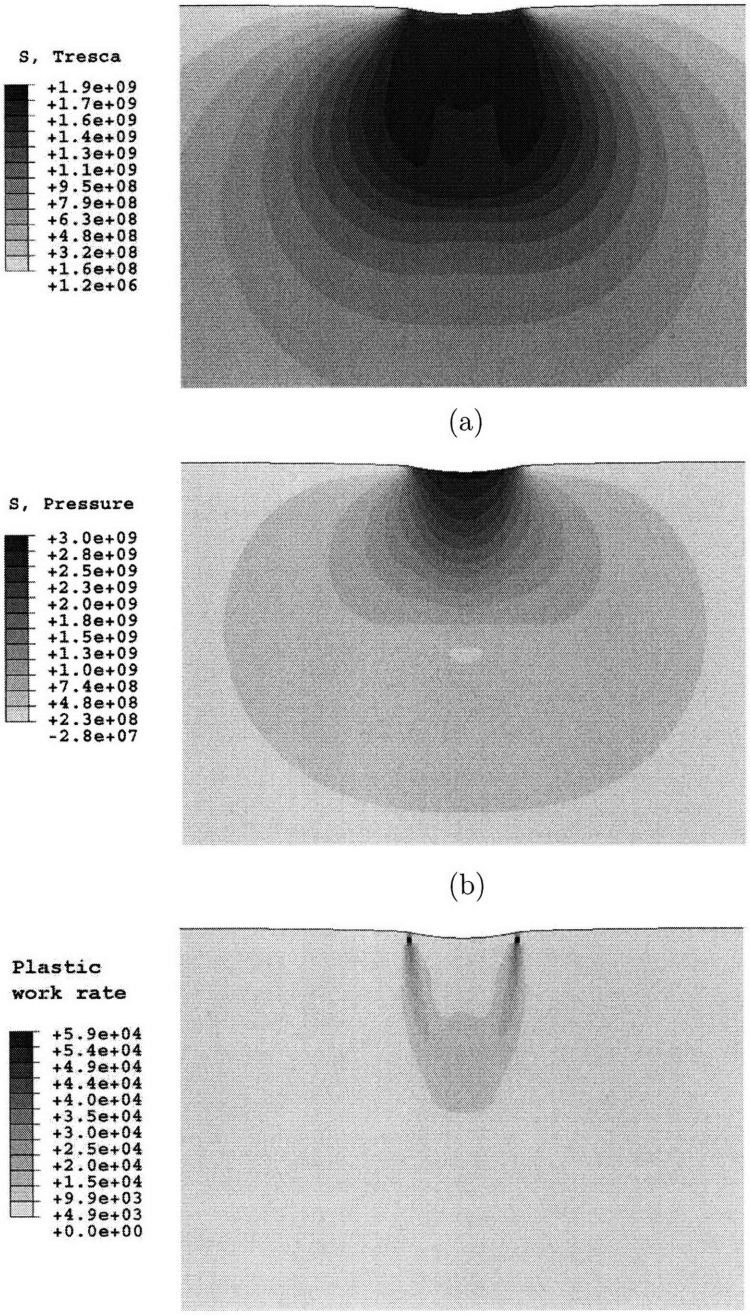

Figure 4-8: Contour plots of (a) Tresca stress, (b) mean normal pressure, and (c) plastic work rate under the indenter at a load of 5 kN.

Chapter 5

A viscoplastic constitutive model for metallic glasses at high homologous temperatures

The elastic-viscoplastic constitutive theory of Anand and Su (2005) for metallic glasses has been extended for application in the high homologous temperature regime. The constitutive equations appearing in the theory have been specialized to model the response of metallic glasses in the temperature range $0.7\,\vartheta_g \lessapprox \vartheta \lessapprox \vartheta_g$ and strain rate range $[10^{-5}, 10^{-2}]\,\mathrm{s}^{-1}$. The material parameters appearing in the theory have been estimated for the metallic glass $Pd_{40}Ni_{40}P_{20}$ from the experimental data of de Hey et al. (1998). The model is shown to capture the major features of the stress-strain response and free volume evolution of this metallic glass. In particular, the phenomena of stress overshoot and strain softening in monotonic experiments at a given strain rate and temperature, as well as strain rate history effects in experiments involving strain rate increments and decrements are shown to be nicely reproduced by the model. The model has been implemented in the finite element program ABAQUS/Explicit (2004) by writing a user material subroutine, and some representative simulations of simple high temperature deformation processing operations on metallic glasses are shown.

5.1 Introduction

Under slow-to-moderate cooling rates most metallic materials solidify in a polycrystalline form. However, under high cooling rates certain metallic alloys solidify in a disordered form; such disordered metals are referred to as *amorphous metals* or *metallic glasses*. The first generation of amorphous metallic glasses were developed in thin ribbon form using very high cooling rates ($\approx 10^5 - 10^6$ K/s) (Klement et al., 1960), but more recently it has been discovered that metallic glasses can be processed in bulk form at relatively slow cooling rates ($\approx 1 - 100$ K/s) in certain multi-component alloy systems due to the sluggish crystallization kinetics in these alloys (Inoue, 2000; Johnson, 1999). The lack of long range order makes the mechanical behavior of amorphous metals considerably different from that of crystalline metals. For a survey of the mechanical properties of metallic glasses, and references to the pertinent literature, see the articles in a recent viewpoint set in Scripta Materialia (Hufnagel, 2006).

When a metallic glass is deformed at ambient temperatures, well below its glass transition temperature, its inelastic response is almost rate-independent and characterized by strong strain-softening, which results in the formation of intense localized shear bands. Fracture typically occurs after very small inelastic strain in tension, but substantial inelastic strain levels can be achieved under states of confined compression, such as in indentation experiments (Spaepen, 1977; Argon, 1979; Donovan, 1988, 1989). However, when a metallic glass is deformed at an absolute temperature ϑ in the range $0.7\vartheta_g \lessapprox \vartheta \lessapprox \vartheta_x$, where ϑ_g and ϑ_x are the glass transition and crystallization temperatures respectively, then its inelastic response is highly rate-dependent and it deforms more-or-less "homogeneously" (Spaepen, 1977), and indeed in the supercooled liquid range $\vartheta_g \lessapprox \vartheta \lessapprox \vartheta_x$ many metallic glasses are known to show superplastic behavior at sufficiently slow strain rates (schroers, 2005).

Some important experimentally-observed features of the tensile or compressive true stress-strain response of metallic glasses at moderate strain rates ($\lessapprox 10^{-2}$/s) in the high temperature range $0.7\vartheta_g \lessapprox \vartheta \lessapprox \vartheta_g$ are: (a) the phenomenon of *stress overshoot and strain softening* (which is a function of pre-annealing history) in monotonic experiments at a given strain rate; and (b) *strain rate history effects* in experiments

involving strain rate increments and decrements. Even though the material may exhibit strain softening in this temperature and strain rate regime, because of the high strain rate sensitivity of the material at elevated temperatures, it does not exhibit macroscopic localized shear bands and the deformation appears as nominally "homogeneous" in simple compression or tensile experiments. A particularly noteworthy experimental study which nicely demonstrates such behaviors for the amorphous metal $Pd_{40}Ni_{40}P_{20}$ ($\vartheta_g \approx 578 - 597\,\mathrm{K}$) is the study conducted by de Hey et al. (1998), in which they used various annealing histories prior to conducting tensile experiments at various strain rates and temperatures, and also conducted attendant differential scanning calorimetry (DSC) experiments to study the effects of disordering of the material during deformation. Some of their major findings are as follows:

- For specimens pre-annealed at 564K for 5000s (which is long enough to bring the material into its equilibrium metastable state at this temperature), tensile stress-strain curves from experiments conducted at 564K and strain rates of $(0.083, 0.17, 0.42, 0.83)\ \times 10^{-3}\mathrm{s}^{-1}$, Fig. 5-1a, exhibited a large amount of stress overshoot and strain softening, after which the flow stress leveled off to a "plateau" value at about 15–20% strain; both the magnitude of the strain softening and the plateau value of the flow stress increase with increasing strain rate.

- For specimens pre-annealed at 556K for 120 s, 720 s and 10,000 s (the two smaller times are not long enough to bring the material into its equilibrium metastable state at this temperature), tensile stress-strain experiments conducted at 556K and a strain rate of $1.7 \times 10^{-4}\mathrm{s}^{-1}$, Fig. 5-1b, show markedly different characteristics in the manner in which the flow stress approaches its plateau value at this strain rate and temperature. As in Fig. 5-1a, the pre-equilibriated sample which was annealed for 10,000 s, exhibited a large amount of strain softening. The strain softening effect was less pronounced in the specimen pre-annealed for 720 s, while the sample with the shortest pre-annealing time of 120 s showed strain hardening instead of strain softening in its approach to the plateau level of the flow stress. The plateau value of the flow stress itself was essentially

independent of the pre-annealing time.

- For specimens pre-annealed at 556K for 3600s, tensile stress-strain curves from strain rate increment-and-decrement experiments conducted at 556K and axial strain rates of $8.3 \times 10^{-5} \rightarrow 4.2 \times 10^{-4} \rightarrow 8.3 \times 10^{-5} s^{-1}$, Fig. 5-1c, showed a pronounced strain-rate-history effect with strong overshoot and undershoot relative to the monotonic experiments conducted at $4.2 \times 10^{-4} s^{-1}$ and $8.3 \times 10^{-5} s^{-1}$.

Based on these experimental observations and their estimates of the changes in the free-volume from their DSC measurements, de Hey et al. (1998) conclude that:

- The material disorders during deformation, and that at a given temperature and strain rate the free volume (a measure of the degree of disorder) reaches an equilibrium value which is different from and independent of its thermal equilibrium volume prior to deformation.

- The strain-softening phenomenon is directly related to the disordering of the material, and that the decrease in the flow stress during a tensile test is related to the creation of additional free volume during the deformation.

Similar conclusions from experimental observations on other metallic glasses have also been recently reported in the literature (cf., e.g., Bletry et al. (2006)).

In a recent paper, aimed at modelling the room-temperature response of metallic glasses, we have developed a thermodynamically-consistent, finite-deformation constitutive theory for the elastic-viscoplastic deformation of isotropic pressure-sensitive and plastically-dilatant materials (Anand and Su, 2005). We also implemented our constitutive model in the finite element program ABAQUS/Explicit (2004) by writing a user material subroutine, and using this numerical implementation of our model, we simulated the room temperature response of a Zr-based metallic glass in tension, compression, strip bending, and indentation, and showed that the results from our numerical simulations qualitatively captured the major features of corresponding results from physical experiments available in the literature. In a companion paper, we experimentally studied the response of a Zr-based metallic glass in instrumented

plane strain indentation, and used our constitutive model and simulation capability to numerically calculate indentation load versus depth curves, and the evolution of corresponding shear-band patterns under the indenter. The numerical simulations were shown to compare very favorably against the corresponding experimental results (Su and Anand, 2006).

The purpose of this chapter is to present a development which extends the theory of Anand and Su (2005) to high homologous temperatures. The new constitutive theory is outlined in §5.2; this theory is fairly general, so in §5.3, with the aim of modelling the experimental observations of de Hey et al. (1998), we specialize the theory for application in the temperature range $0.7\,\vartheta_g \lessapprox \vartheta \lessapprox \vartheta_g$ and strain rate range $[10^{-5}, 10^{-2}]\text{s}^{-1}$ of interest. In §5.4 we use experimental data for $Pd_{40}Ni_{40}P_{20}$ from de Hey et al. (1998) to estimate the material parameters appearing in our specialized constitutive equations, and using these material parameters we show how well the numerically-calculated stress-strain curves compare against the corresponding experimental results. We have implemented our constitutive model in the finite element program ABAQUS/Explicit (2004). As representative examples of our numerical simulation capability to model high temperature deformation processing operations, in §5.5 we report on finite element simulations of plane-strain tension, plane-strain strip bending, and axi-symmetric hot-embossing. We close in §5.6 with some final remarks.

5.2 Constitutive model

We limit our considerations to *isothermal* situations at a fixed temperature in the absence of temperature gradients. Our constitutive equations relate the following basic fields: $\mathbf{x} = \boldsymbol{\chi}(\mathbf{X}, t)$, motion; $\mathbf{F} = \nabla\boldsymbol{\chi}$ with $J = \det\mathbf{F} > 0$, deformation gradient; $\mathbf{F} = \mathbf{F}^e\mathbf{F}^p$, multiplicative elastic-plastic decomposition; $\mathbf{F}^p$ with $J^p = \det\mathbf{F}^p > 0$, plastic distortion; $\mathbf{F}^e$ with $J^e = \det\mathbf{F}^e > 0$, elastic distortion; $\mathbf{F}^e = \mathbf{R}^e\mathbf{U}^e$, polar decomposition of $\mathbf{F}^e$; $\mathbf{U}^e = \sum_{\alpha=1}^{3} \lambda_\alpha^e \mathbf{r}_\alpha \otimes \mathbf{r}_\alpha$, spectral decomposition of $\mathbf{U}^e$; $\mathbf{E}^e = \sum_{\alpha=1}^{3} (\ln\lambda_\alpha^e)\mathbf{r}_\alpha \otimes \mathbf{r}_\alpha$, logarithmic elastic strain; $\mathbf{T}$, Cauchy stress; $\mathbf{T}^e = J^e\,\mathbf{R}^{e\mathsf{T}}\,\mathbf{T}\,\mathbf{R}^e$, stress conjugate to elastic strain $\mathbf{E}^e$; ψ, free energy density per unit volume of intermediate space; $\vartheta > 0$, absolute temperature; and $\eta > 0$, "free volume" (order-

parameter).[1]

The set of constitutive equations is summarized below:

1. **Free energy under isothermal conditions at a temperature ϑ:**

$$\psi = G|\mathbf{E}_0^e|^2 + \frac{1}{2}K(\mathrm{tr}\,\mathbf{E}^e)^2, \quad \text{with} \quad G(\vartheta) > 0 \quad \text{and} \quad K(\vartheta) > 0, \tag{5.1}$$

where G and K denote the temperature-dependent shear and bulk moduli, respectively. the elastic constants (G, K) will depend on the "free-volume" parameter η. However, the effects of including such a dependence on (G, K) are expected to be small, and for simplicity we neglect such a dependence of ψ on η here (cf. (Anand and Su, 2005) for a theory including such a dependence).

2. **Equation for the stress:**

$$\mathbf{T}^e = \frac{\partial \psi}{\partial \mathbf{E}^e} = 2G\mathbf{E}_0^e + K\,(\mathrm{tr}\,\mathbf{E}^e)\,\mathbf{1}\,. \tag{5.2}$$

This symmetric stress tensor has the spectral representation

$$\mathbf{T}^e = \sum_{i=1}^{3} \sigma_i\, \hat{\mathbf{e}}_i \otimes \hat{\mathbf{e}}_i, \tag{5.3}$$

where $\{\sigma_i | i = 1, 2, 3\}$ are the principal values, and $\{\hat{\mathbf{e}}_i | i = 1, 2, 3\}$ the corresponding orthonormal principal directions. We assume that the principal stresses $\{\sigma_i | i = 1, 2, 3\}$ are strictly ordered such that

$$\sigma_1 \geq \sigma_2 \geq \sigma_3. \tag{5.4}$$

3. **Flow rule:**

We assume that plastic flow occurs by shearing accompanied by dilatation relative to some "slip systems", and take the evolution equation for $\mathbf{F}^p$ to be given by

$$\dot{\mathbf{F}}^p = \mathbf{L}^p\,\mathbf{F}^p, \qquad \mathbf{F}^p(\mathbf{X}, 0) = \mathbf{1}, \tag{5.5}$$

[1] *Caution*: η does not denote either the entropy density, nor a viscosity parameter.

with

$$\mathbf{L}^p = \sum_\alpha \nu^{(\alpha)}\, \mathbf{s}^{(\alpha)} \otimes \mathbf{m}^{(\alpha)} + \delta^{(\alpha)}\, \mathbf{m}^{(\alpha)} \otimes \mathbf{m}^{(\alpha)}, \qquad \text{and} \qquad \delta^{(\alpha)} = \beta \nu^{(\alpha)}. \quad (5.6)$$

Each slip system is specified by a slip direction $\mathbf{s}^\alpha$ and a slip plane normal $\mathbf{m}^\alpha$, with $(\mathbf{s}^\alpha, \mathbf{m}^\alpha)$ orthonormal, and ν^α denotes the shearing rate.[2] The dilatation rate associated with shearing on each slip system is $\delta^{(\alpha)} = \beta \nu^{(\alpha)}$, with β a *shear-induced plastic dilatancy function*; positive values of β describe plastically dilatant behavior, while $\beta < 0$ describes behavior that is plastically compacting.

For an amorphous isotropic material there are no preferred directions other than the principal directions of stress; accordingly we consider plastic flow to be possible on the following six potential slip systems defined relative to the principal directions of stress $\mathbf{T}^e$:

$$\left.\begin{aligned}
\mathbf{s}^{(1)} &= \cos\xi \hat{\mathbf{e}}_1 + \sin\xi \hat{\mathbf{e}}_3, & \mathbf{m}^{(1)} &= \sin\xi \hat{\mathbf{e}}_1 - \cos\xi \hat{\mathbf{e}}_3, \\
\mathbf{s}^{(2)} &= \cos\xi \hat{\mathbf{e}}_1 - \sin\xi \hat{\mathbf{e}}_3, & \mathbf{m}^{(2)} &= \sin\xi \hat{\mathbf{e}}_1 + \cos\xi \hat{\mathbf{e}}_3, \\
\mathbf{s}^{(3)} &= \cos\xi \hat{\mathbf{e}}_1 + \sin\xi \hat{\mathbf{e}}_2, & \mathbf{m}^{(3)} &= \sin\xi \hat{\mathbf{e}}_1 - \cos\xi \hat{\mathbf{e}}_2, \\
\mathbf{s}^{(4)} &= \cos\xi \hat{\mathbf{e}}_1 - \sin\xi \hat{\mathbf{e}}_2, & \mathbf{m}^{(4)} &= \sin\xi \hat{\mathbf{e}}_1 + \cos\xi \hat{\mathbf{e}}_2, \\
\mathbf{s}^{(5)} &= \cos\xi \hat{\mathbf{e}}_2 + \sin\xi \hat{\mathbf{e}}_3, & \mathbf{m}^{(5)} &= \sin\xi \hat{\mathbf{e}}_2 - \cos\xi \hat{\mathbf{e}}_3, \\
\mathbf{s}^{(6)} &= \cos\xi \hat{\mathbf{e}}_2 - \sin\xi \hat{\mathbf{e}}_3, & \mathbf{m}^{(6)} &= \sin\xi \hat{\mathbf{e}}_2 + \cos\xi \hat{\mathbf{e}}_3,
\end{aligned}\right\} \quad (5.7)$$

with

$$\xi \stackrel{\text{def}}{=} \frac{\pi}{4} + \frac{\phi}{2}, \quad (5.8)$$

where

$$\phi \stackrel{\text{def}}{=} \arctan \mu \quad (5.9)$$

is an *angle of internal friction*, and $\mu \geq 0$ an *internal friction coefficient.* We emphasize that these slip systems are not the classical slip systems of crystal plasticity, but are constructs of our mathematical model for isotropic amorphous materials; they are related to the principal directions of the stress, and they

[2]The shearing rate is often denoted as $\dot{\gamma}^{(\alpha)}$ in the literature.

change both spatially and temporally as the principal directions of stress change in a non-homogeneously deforming material.

With the resolved shear and compressive normal traction on each slip system defined by

$$\tau^{(\alpha)} \stackrel{\text{def}}{=} \mathbf{s}^{(\alpha)} \cdot \mathbf{T}^e \mathbf{m}^{(\alpha)}, \qquad \sigma^{(\alpha)} \stackrel{\text{def}}{=} -\mathbf{m}^{(\alpha)} \cdot \mathbf{T}^e \mathbf{m}^{(\alpha)}, \tag{5.10}$$

the corresponding shearing rate is given by a flow function

$$\nu^{(\alpha)} = \hat{\nu}^{(\alpha)}(\tau^{(\alpha)}, \sigma^{(\alpha)}, \vartheta, s, \mu, \eta) \geq 0, \tag{5.11}$$

where $s > 0$ is a stress-dimensioned internal variable representing the *slip resistance*, assumed for an isotropic material to be the same for all slip systems.

It is convenient to write Λ for the list of variables

$$\Lambda = (\mathbf{T}^e, \vartheta, s, \mu, \eta).$$

Using this notation, we assume that the dilatancy parameter β depends on Λ,

$$\beta = \hat{\beta}(\Lambda). \tag{5.12}$$

The dissipation inequality in the theory is

$$\mathbf{T}^e : \mathbf{L}^p > 0 \quad \text{for} \quad \mathbf{L}^p \neq \mathbf{0}. \tag{5.13}$$

With $\mathbf{L}^p$ given by (5.6) and (5.7), the dissipation inequality requires that

$$\mathbf{T}^e : \mathbf{L}^p = \sum_{\alpha=1}^{6} \left[\tau^{(\alpha)} - \beta\, \sigma^{(\alpha)}\right] \nu^{(\alpha)} > 0 \tag{5.14}$$

whenever plastic flow occurs. We assume that the material is *strongly dissipative*

in the sense that

$$\left[\tau^{(\alpha)} - \beta\,\sigma^{(\alpha)}\right]\nu^{(\alpha)} > 0 \qquad \text{for each } \alpha\,. \tag{5.15}$$

Thus, whenever $\nu^{(\alpha)} > 0$, we must have

$$\left[\tau^{(\alpha)} - \beta\,\sigma^{(\alpha)}\right] > 0, \tag{5.16}$$

which is a restriction that the dilatancy function $\beta = \hat{\beta}(\Lambda)$ must satisfy.

4. **Evolution equations for the internal variables**:

   The internal variables of the theory are the internal friction coefficient $\mu \geq 0$, the slip resistance $s > 0$, and the free-volume parameter $\eta > 0$. We assume that the evolution of these internal variables is given by coupled differential equations:

$$\left.\begin{aligned} \dot{\mu} &= f(\Lambda, \nu), \\ \dot{s} &= h(\Lambda, \nu), \\ \dot{\eta} &= g(\Lambda, \nu), \end{aligned}\right\} \tag{5.17}$$

   where

$$\nu \stackrel{\text{def}}{=} \sum_{\alpha} \nu^{(\alpha)} \tag{5.18}$$

   is the sum of the shearing rate on all the slip systems.

5.3 Specialization of the constitutive equations. Application to the metallic glass $Pd_{40}Ni_{40}P_{20}$

The constitutive theory outlined in the previous section is fairly general. With the aim of modelling the experimental observations of de Hey et al. (1998), we specialize the scalar constitutive functions (5.11), (5.12) and (5.17) for application in the temperature range $0.7\,\vartheta_g \lessapprox \vartheta \lessapprox \vartheta_g$ and strain rate range $[10^{-5}, 10^{-2}]\,\mathrm{s}^{-1}$ of interest.

5.3.1 Scalar shearing rate $\nu^{(\alpha)}$

The shearing rate on each slip system is taken in a simple thermally-activated power-law form

$$\nu^{(\alpha)} = \nu_0 \exp\left(-\frac{Q}{k_B\vartheta}\right)\left[\frac{\tau^{(\alpha)}}{s+\mu\sigma^{(\alpha)}}\right]^{1/m} \geq 0, \tag{5.19}$$

where ν_0 a *reference shear strain rate*, Q is an *activation energy*, k_B the Boltzmann's constant, and $m = \hat{m}(\vartheta) > 0$ is a temperature-dependent *strain rate sensitivity* parameter.

For $\nu^{(\alpha)} > 0$, the flow equation (5.19) may be inverted to read

$$\tau^{(\alpha)} = \left(s+\mu\sigma^{(\alpha)}\right)\left[\frac{\nu^{(\alpha)}}{\nu_0}\exp\left(\frac{Q}{k_B\vartheta}\right)\right]^m, \tag{5.20}$$

which shows that the term $\mu\sigma^{(\alpha)}$ accounts for the *pressure-sensitivity* of plastic flow. Also, the limits $m \to 1$ and $m \to 0$ correspond to the *linearly viscous* and *rate-independent* limits, respectively.

5.3.2 Evolution equations for μ, s and η; dilatancy function β

For the amorphous metallic materials under consideration we take the internal friction μ to be a constant,

$$\mu = \mu_0 \geq 0; \tag{5.21}$$

there is not enough experimental information to be more specific here.

For s and η we consider evolution equations in the following special *coupled* form:

$$\left.\begin{aligned} \dot{s} &= \underbrace{h\,\nu}_{\text{dynamic evolution}} - \underbrace{r_s}_{\text{static recovery}}, \\ \dot{\eta} &= \underbrace{\beta\,\nu}_{\text{dynamic evolution}} - \underbrace{r_\eta}_{\text{static recovery}}, \end{aligned}\right\} \tag{5.22}$$

with

$$\left.\begin{aligned} h &= h_0\,(s_* - s)\,, \qquad & s_* &= \hat{s}_*(\nu, \vartheta, \eta) > 0, \\ \beta &= g_0 \left(1 - \frac{\eta}{\eta_*}\right), \qquad & \eta_* &= \hat{\eta}_*(\nu, \vartheta) > 0, \end{aligned}\right\} \tag{5.23}$$

also

$$r_s = \hat{r}_s(s, \eta, \vartheta), \qquad r_\eta = \hat{r}_\eta(s, \eta, \vartheta), \tag{5.24}$$

and temperature-dependent initial values

$$s(\mathbf{X}, 0) = s_0(\vartheta), \qquad \eta(\mathbf{X}, 0) = \eta_0(\vartheta)\,. \tag{5.25}$$

In these evolution equations h represents the strain-hardening/softening function for the slip resistance during plastic flow, $\nu > 0$: the material hardens ($h > 0$) if $s_* > s$, and softens ($h < 0$) if $s_* < s$. The critical value s_* of s controlling such hardening/softening transitions is assumed to depend on the current values of the plastic strain rate, temperature, and free volume. In the dilatancy function the parameter η_* represents a strain rate and temperature-dependent critical value for the free-volume: the material dilates ($\beta > 0$) when $\eta < \eta_*$, and compacts ($\beta < 0$) when $\eta > \eta_*$. In a monotonic experiment at a given strain rate and temperature the shear-induced dilatancy vanishes ($\beta = 0$) when $\eta = \eta_*$. However, in an experiment in which the strain rate and temperature are varying (e.g. strain rate or temperature jump experiments) the material will in general dilate or compact, depending on the strain rate and temperature history, and because of the coupling between the evolution equations for s and η the slip resistance will also vary.

The functions r_s and r_η represent *static thermal recovery* functions for the slip resistance and the free volume at a given temperature, whenever there is no macroscopic plastic flow ($\nu = 0$).

The tension experiments by de Hey et al. (1998) on $Pd_{40}Ni_{40}P_{20}$ that we shall consider in the next section were all performed at macroscopic strain rates greater than $8 \times 10^{-5}\,\mathrm{s}^{-1}$ to strain levels of less than 50%. For this strain rate and strain regime, we assume that the time-scale of the static recovery processes is sufficiently slow so that effects of static recovery on the evolution of s and η may be neglected.

Accordingly, we do not consider further specifications of the recovery functions r_s and r_η, and set them to zero for the application under consideration.

As a particular form for the critical value s_* of s in the hardening function (5.23), we consider

$$s_* = \tilde{s} \left[\frac{\nu}{\nu_0} \exp\left(\frac{Q}{k_B \vartheta} \right) \right]^n + b \, (\eta_* - \eta) \,, \tag{5.26}$$

with $n = \hat{n}(\vartheta)$ not necessarily equal to $m = \hat{m}(\vartheta)$, but (ν_0, Q) the same as in (5.19).

A simple analytical form for the dependency of the critical value η_* on ν and ϑ is elusive. In the next section, guided by the experimental data of de Hey et al. (1998) for the metallic glass $Pd_{40}Ni_{40}P_{20}$, we will construct and curve-fit a simple empirical form for this function.

To summarize, we have considered specialized constitutive equations for the slip rates ν^α which involve the material parameters

$$\{\nu_0, Q, m, \mu_0\} \,,$$

and the material parameters

$$\{h_0, \tilde{s}, n, b, g_0\} \,.$$

in the evolution equations for s and η, with the particular function $\eta_* = \hat{\eta}_*(\nu, \vartheta)$ and the attendant material parameters yet to be determined.

Remark:

Let ν denote a positive plastic shear strain rate in a *one-dimensional* setting. In such a setting, de Hey et al. (1998) use an Eyring-type flow equation of the form

$$\nu = 2 \, c_f \, k_f \frac{\gamma_0 \upsilon_0}{\Omega} \sinh\left(\frac{\tau \, \gamma_0 \, \upsilon_0}{2 \, k_B \, \vartheta} \right)$$

proposed by Spaepen (1977). Here τ is a positive shear stress, γ_0 is a local transformation strain, υ_0 is an activation volume, Ω is an atomic volume, k_f is a temperature dependent rate factor, and

$$c_f = \exp(-\frac{1}{\eta}) \tag{5.27}$$

is concentration of flow defects defined in terms of the free-volume parameter η.[3]

In de Hey et al. (1998), the evolution of the defect concentration is taken as

$$\dot{c}_f = \underbrace{(a_x\, c_f\, \ln^2 c_f)\, \nu}_{\text{dynamic evolution}} - \underbrace{k_r\, c_f\, (c_f - c_{f,eq})}_{\text{static recovery}} \tag{5.28}$$

with a_x a temperature dependent parameter, k_r a temperature-dependent rate factor, and

$$c_{f,eq} = \exp(-\frac{1}{\eta_{eq}}), \tag{5.29}$$

where

$$\eta_{eq} = \frac{\vartheta - \vartheta_0}{B} \tag{5.30}$$

is the value of the free volume in thermal equilibrium at a temperature ϑ; here ϑ_0 and B are two material constants known as the Vogel-Fulcher-Tamann (VFT) parameters.

The special constitutive functions considered by us, although similar in spirit to those considered by de Hey et al. (1998), are quite different in detail. In particular: (i) they do not introduce an internal variable corresponding to our slip resistance s; and (ii) in their evolution equation for the defect concentration there is no allowance for *dynamic recovery* in the dynamic evolution term in (5.28); the rate of change of c_f vanishes only as a consequence of balance between the production term $(a_x\, c_f\, \ln^2 c_f)\, \nu$ and the *static recovery* term $k_r\, c_f\, (c_f - c_{f,eq})$. In contrast, we have argued that the effects of static recovery in the experiments reported in de Hey et al. (1998) are negligible, and as we shall show below, our evolution for the free volume

$$\dot{\eta} = g_0 \left(1 - \frac{\eta}{\eta_*}\right) \nu, \qquad \eta_* = \hat{\eta}_*(\nu, \vartheta), \tag{5.31}$$

when specialized using the data of de Hey et al. (1998), is able to nicely reproduce their experimental stress-strain curves.

[3]Note: de Hey et al. (1998) use the symbol x instead of η for the (reduced) free volume parameter.

5.4 Estimates of material parameters for $Pd_{40}Ni_{40}P_{20}$

We have estimated the material parameters appearing in our model from experimental data and results available in the literature for $Pd_{40}Ni_{40}P_{20}$. The following specific values for the material parameters were chosen:

- Elastic Moduli:

  Davis et al. (1976) report values of $E = 96\,\text{GPa}$ and $\nu_{\text{Poisson}} = 0.36$ for the room temperature values of the Young's modulus and Poisson's ratio. The corresponding values for the shear and bulk moduli are

  $$G = 35.3\,\text{GPa} \quad \text{and} \quad K = 114.3\,\text{GPa}.$$

  For simplicity we assume that the change in the values of the elastic moduli of amorphous metals for temperatures in the range from room temperature to ϑ_g is small, and use the values above for all temperatures below ϑ_g.

- Friction coefficient:

  Donovan (1989) quotes a value of $\mu = 0.11$ for $Pd_{40}Ni_{40}P_{20}$ from his estimates of this parameter based on measured shear band orientations in compression at room temperature. However, we have shown previously that shear band orientations are controlled not only by the friction coefficient μ, but also the dilatancy parameter β, and estimates for the friction parameters from shear band orientations typically yield abnormally high values (Anand and Su, 2005; Su and Anand, 2006). For a Zr-based metallic glass we estimated a value

  $$\mu = 0.04.$$

  We use this estimate also for the Pd-based glass. No high temperature measurements for the pressure sensitivity of plastic flow for this material appear to have been reported in the literature.

- Viscoplasticity parameters:

We have used the simple tension stress-strain curves of de Hey et al. (1998), Fig. 5-1a, to calibrate the viscoplasticity parameter for $Pd_{40}Ni_{40}P_{20}$. In simple tension the principal stresses are

$$\sigma_1 > 0, \quad \sigma_2 = \sigma_3 = 0\,. \tag{5.32}$$

Straight-forward calculations using (5.7) and (5.10) show that in this case the resolved shear stresses and compressive normal tractions on the slip systems are given by

$$\tau \stackrel{\text{def}}{=} \tau^{(1)} = \tau^{(2)} = \tau^{(3)} = \tau^{(4)} = \tfrac{1}{2}\sin(2\xi)\,\sigma_1, \quad \tau^{(5)} = \tau^{(6)} = 0, \tag{5.33}$$

and

$$\sigma^{(1)} = \sigma^{(2)} = \sigma^{(3)} = \sigma^{(4)} = \sin^2\xi\sigma_1, \quad \sigma^{(5)} = \sigma^{(6)} = 0. \tag{5.34}$$

Thus, (5.19) dictates that the shearing rate on the slip systems must obey,

$$\nu^{(1)} = \nu^{(2)} = \nu^{(3)} = \nu^{(4)} > 0, \quad \text{and} \quad \nu^{(5)} = \nu^{(6)} = 0. \tag{5.35}$$

For $\mu = 0.04$, the angle of internal friction is $\phi = 0.04$ rads, and if we neglect the effects of this small value, it is easy to verify that the non-zero resolved shear stresses and shearing rate on the slip system may be approximated as

$$\tau = \tau^{(1)} = \tau^{(2)} = \tau^{(3)} = \tau^{(4)} \approx \tfrac{1}{2}\sigma, \quad \text{and} \quad \nu^{(1)} = \nu^{(2)} = \nu^{(3)} = \nu^{(4)} \approx \tfrac{1}{2}\dot{\epsilon}^p, \tag{5.36}$$

where $\sigma > 0$ and $\dot{\epsilon}^p > 0$ are the axial stress and axial plastic strain rate in a tension test. Thus, in a fully-developed flow state at an axial strain rate $\dot{\epsilon}$, when the axial stress reaches the steady-state "plateau" stress σ_{ss} and $\dot{\epsilon} \approx \dot{\epsilon}^p$, we have

$$\tau_{ss} \stackrel{\text{def}}{=} \tfrac{1}{2}\sigma_{ss}, \quad \text{and} \quad \nu \stackrel{\text{def}}{=} \sum_{\alpha=1}^{4} \nu^{(\alpha)} = 2\dot{\epsilon}\,. \tag{5.37}$$

At steady state in a monotonic tension test at a given strain rate and temperature, $s = s^*$, $\eta = \eta_*$, the term $b(\eta_* - \eta)$ vanishes, and substituting the

corresponding value of $s_\star$ from (5.26) in (5.20) one obtains

$$\tau_{ss} = \tilde{s}\,(\frac{1}{4})^m \left\{ \frac{\nu}{\nu_0} \exp\left(\frac{Q}{k_B\vartheta}\right)\right\}^{m+n}. \tag{5.38}$$

By taking logarithms on both sides of (5.38) we obtain

$$\ln\tau_{ss} = (m+n)\,\ln\nu + \left[(m+n)\,\left(\frac{Q}{k_B\vartheta} - \ln\nu_0\right) + \ln(\tilde{s}\,(\frac{1}{4})^m)\right], \tag{5.39}$$

which shows that at a constant temperature $\ln\tau_{ss}$ is linear in $\ln\nu$. Tuinstra et al. (1995) provide the following estimate for the activation energy for $Pd_{40}Ni_{40}P_{20}$

$$Q = 2.66 \times 10^{-19}\,\mathrm{J}.$$

A fit of (5.39) to the steady state flow stress σ_{ss} at various strain rates $\dot{\epsilon}$ and temperatures data provided by de Hey et al. (1998) (their Fig. 6), allows us to determine the slope $(m+n)$ as a function of temperature. For simplicity we assume that the two rate-sensitivity parameters m and n are equal to each other. Then at 564K we find that

$$m = n = 0.1316,$$

and that the temperature sensitivity of these parameters in the range 549K through 564K may be approximated by the empirical relation

$$m = n = (2.6375 \times 10^{-3})\,\vartheta - 1.356\,.$$

With these estimates of Q, m and n, (5.39) and the data of de Hey et al. (1998) then allows us to estimate the following values for ν_0 and $\tilde{s}$:

$$\nu_0 = 2.47 \times 10^{13}\,\mathrm{s}^{-1}, \qquad \tilde{s} = 500\,\mathrm{MPa}\,.$$

The quality of the fit using (5.39) and these material parameters to the $(\sigma_{ss}, \dot{\epsilon})$ data of de Hey et al. (1998) is shown in Fig. 5-2.

- Steady state free volume as a function of strain rate and temperature:

  In order to estimate the function

$$\eta_* = \hat{\eta}_*(\nu, \vartheta)$$

  (cf. eq. (5.31)), we use the data in Fig. 5 of de Hey et al. (1998). Their data is expressed in terms of the defect concentration ratio (cf. eq. (5.27))

$$\frac{c_{f,*}}{c_{f,eq}} = \frac{\exp(-1/\eta_*)}{\exp(-1/\eta_{eq})}, \tag{5.40}$$

  as a function of $\dot{\epsilon}$, where η_{eq} is the thermal equilibrium value of the free volume (cf. eq. (5.30)) with VFT parameters

$$\vartheta_0 = 355\,\mathrm{K}, \qquad B = 6600\,\mathrm{K}$$

  for $Pd_{40}Ni_{40}P_{20}$. The $\ln(c_{f,*}/c_{f,eq})$ versus $\ln\dot{\epsilon}$ data of de Hey et al. (1998) at three different temperatures is shown in Fig. 5-3. approximated as a linear dependence of $\ln(c_{f,*}/c_{f,eq})$ on $\ln\dot{\epsilon}$. By fitting such a linear relationship to their data we obtain

$$\ln\left(\frac{c_{f,*}}{c_{f,eq}}\right) = k\,\ln\nu + l, \tag{5.41}$$

  where k and l are linear functions of temperature,

$$k = 10.8 - 0.0179\,\vartheta, \qquad l = 253 - 0.435\,\vartheta.$$

  The quality of the curve-fit is shown in Fig. 5-3.

  Next, using $(5.30)_2$ and (5.40), eq. (5.41) may be expressed in terms of the free volume as

$$\eta_* = \left[\frac{1}{\eta_{eq}} - (k\ln\nu + l)\right]^{-1} \quad \text{with} \quad \eta_{eq} = \frac{\vartheta - \vartheta_0}{B}\,. \tag{5.42}$$

  The steady state free volume as a function of strain rate and temperature using this simple model is plotted in Fig. 5-4 and compared with the corresponding

data of de Hey et al. (1998) (their Fig. 4).

- Material parameters in the evolution equations for the slip resistance and the free volume:

  Recall that the coupled evolution equations for s and η are

$$\begin{aligned} \dot{s} &= h_0 \, (s_* - s) \, \nu, \qquad s(0) = s_0 \,, \\ s_* &= \tilde{s} \left[\frac{\nu}{\nu_0} \exp\left(\frac{Q}{k_B \vartheta} \right) \right]^n + b \, (\eta_* - \eta) \,, \\ \dot{\eta} &= g_0 \left(1 - \frac{\eta}{\eta_*} \right), \qquad \eta(0) = \eta_0. \end{aligned}$$

  The initial value η_0 depends on the pre-annealing history of the material, and at thermal equilibrium is estimated using (5.30) and the values of the VFT parameters ϑ_0 and B listed above. Also, with the function η_* and the material parameters $\{\nu_0, Q, n, \tilde{s}\}$ as estimated above, it remains to determine the parameters $\{s_0, h_0, b, g_0\}$. These are determined by fitting the complete stress strain curves at 564K and four different strain rates, $(0.83, 0.42, 0.17, 0.083) \times 10^{-3} s^{-1}$, Fig. 5-1a.

  The material in these experiments was pre-annealed at 564K for 5000 s, which is long enough for it to be in thermal equilibrium; in this case (5.30) gives

$$\eta_0 = 0.0317.$$

  Noting that s_0 controls the beginning of the nonlinearity in the stress-strain curves, h_0 controls the strain hardening slope of the curves, b controls the peak value, and g_0 controls how quickly the strain softening occurs; a few trials using different values of these parameters yield the following estimates:

$$s_0 = 20 \, \text{MPa}, \quad h_0 = 75, \quad b = 1.4 \times 10^5 \, \text{MPa}, \quad g_0 = 0.55,$$

  which provide the acceptable fits to the complete stress strain curves shown in Fig. 5-5. The model captures the essential features observed in the experiments:

the extent of the stress overshoot, the strain softening, and the different plateau levels of the flow stress after $\approx 15 - 20\%$ strain at the different strain rates are all reproduced very well by the model.

Using the material parameters so determined, in the next two subsections we verify the predictive capability of the model to reproduce the additional experimental results of de Hey et al. (1998) shown in Figs. 5-1b,c.

5.4.1 Effects of pre-annealing history

The pronounced effect of the initial value of the free volume on stress-strain curves is further illustrated with results from tension tests conducted at the same temperature and strain rate, but on specimens with different pre-annealing histories. Fig. 5-1b shows stress-strain curves for specimens pre-annealed at 556K for 120 s, 720 s and 10,000 s, and subsequently tested at a temperature of 556K and a strainrate of $1.7 \times 10^{-4}\,\mathrm{s}^{-1}$.

The initial values of the free volume for the three specimens with the different pre-annealing times are different. The specimen that is annealed for 10,000 s will have an initial free volume very close to the thermal equilibrium value at this temperature, while the specimens that are annealed for shorter periods will have higher initial free volumes. In our simulations of these experiments we assigned initial values

$$\eta_0 = 0.0346, \quad 0.0336, \quad \text{and} \quad 0.0310$$

for the specimens pre-annealed for 120 s, 720 s, and 10,000 s, respectively. The stress-strain curves calculated using these initial values of η_0 and with the values of the other material parameters fixed as in the previous section, are compared against the corresponding experimental measurement in Fig. 5-6; the numerically-simulated results are in excellent agreement with the experimental measurements.

The steady state free volume for this test condition calculated from (5.42) is

$$\eta_*(1.7 \times 10^{-4}\,\mathrm{s}^{-1}, 556\mathrm{K}) = 0.0344.$$

Thus, the specimen that is annealed for 10,000 s has an initial free volume $\eta_0 = 0.031$ that is substantially less than $\eta_* = 0.0344$. Using the terminology of soil-mechanics, it is in an "over-consolidated" state, and it is this over-consolidated initial state that leads to the large amount of stress overshoot. The specimen that is annealed for 720 s has an initial value $\eta_0 = 0.0336$, which is only slightly smaller than $\eta_* = 0.0344$. This specimen is therefore in a slightly over-consolidated condition, and correspondingly the stress overshoot exhibited by this specimen is much less pronounced than that in the previous case. Finally, for the specimen that is annealed for 120 s, the initial value of the free volume is $\eta_0 = 0.0346$, which is larger than $\eta_* = 0.0344$, so the specimen is "under-consolidated." In this case there is no stress overshoot and strain-softening; indeed, the material strain-hardens with the stress-strain curve increasing monotonically to approach the steady state flow stress, which is a function only of temperature and strain rate of the experiment, but independent of the pre-annealing history.

5.4.2 Effects of strain rate history

Fig. 5-1c shows the stress-strain curve from a strain rate increment-and-decrement experiment conducted at 556K and axial strain rates of $8.3 \times 10^{-5} \rightarrow 4.2 \times 10^{-4} \rightarrow 8.3 \times 10^{-5}$/s, with the jumps occurring at strain levels of 0.125 and 0.27 (de Hey et al., 1998). The specimen was pre-annealed at 556K for 3600s, and (5.30) yields a value of

$$\eta_0 = 0.0334.$$

Also, for the strain rates of $8.3 \times 10^{-5}\,\mathrm{s}^{-1}$ and $4.2 \times 10^{-4}\,\mathrm{s}^{-1}$, the steady state values of η at 556K using (5.42) are

$$\eta_*(8.3 \times 10^{-5}\,\mathrm{s}^{-1}, 556\mathrm{K}) = 0.0337, \quad \text{and} \quad \eta_*(4.2 \times 10^{-4}\,\mathrm{s}^{-1}, 556\mathrm{K}) = 0.0354\,.$$

At the beginning of the experiment $\eta_0 = 0.0334$ is slightly less than $\eta_*(8.3\times10^{-5}\,\mathrm{s}^{-1}, 556\mathrm{K}) = 0.0337$, so the specimen is slightly "over-consolidated," and the first portion of the stress-strain curve shows a small amount of overshoot. By a strain level of 0.125 the

specimen has almost reached the steady state value of the free volume for this strain rate. When the strain rate is suddenly increased to $4.2 \times 10^{-5} s^{-1}$, the steady state free volume also increases from $\eta_* = 0.0337 \rightarrow \eta_* = 0.0354$, and hence the specimen is now significantly "over-consolidated" relative to the steady state value η_* at the higher strain rate. This this manifests itself in a clear overshoot in the stress-strain curve followed by strain softening until the flow stress reaches its steady value at the higher strain rate. By a strain level of 0.27 the specimen is almost at its steady state value of $\eta_* = 0.0354$ for the higher strain rate. Thus, when the strain rate is suddenly decreased back to its lower value of $8.3 \times 10^{-5}\,\mathrm{s}^{-1}$, the value of η_* at the lower strain rate is again $\eta_* = 0.0337$, and the specimen is now in an "under-consolidated" condition. Correspondingly, the stress-strain curve now shows a stress undershoot as it approaches the new steady state value. The numerically-simulated stress-strain curve shown in Fig. 5-7 captures the complex experimentally-measured strain rate history response quite well.

We have implemented our constitutive model in the finite-element computer program ABAQUS/Explicit (ABAQUS/Explicit, 2004) by writing a user material subroutine. As representative examples of our numerical simulation capability to model high temperature deformation processing operations, we report on some finite element simulations in the section below.

5.5 Finite element simulations

5.5.1 Plane strain tension

When a metallic glass is deformed at a low homologous temperature, its inelastic response is almost rate-independent and characterized by strong strain-softening, which results in the formation of intense localized shear bands; and in tension the material typically fails abruptly with very little evidence of plastic strain at the macroscopic level. One of the simulations that we performed in our earlier paper (Anand and Su, 2005), was that for plane strain tension of a Zr-based metallic glass at room temperature. In that simulation we used 5000 ABAQUS-CPE4R plane-strain ele-

ments to represent the tension specimen; Fig. 4 of Anand and Su (2005). As shown in our previous simulation, once a few shear bands initiate at heterogeneities in the microstructure, further inelastic deformation occurs mainly inside these bands and the material fails shortly thereafter, with the material outside the shear bands not experiencing much plastic deformation; Fig. 5 of Anand and Su (2005).

We have repeated a similar plane strain tension simulation for the Pd-based glass deformed at a high homologous temperature of 556K and a strain rate of $1.7\times10^{-4}\,\mathrm{s}^{-1}$. The finite element mesh used for this simulation is shown in Fig. 5-8a. In order to simulate the spatial variations in the initial free volume of actual materials, the initial free volume η_0 in the simulation was statistically assigned in every element using a Gaussian distribution with a mean value of 0.0316, and a standard deviation of 0.0001. A contour plot of this initial free volume distribution is shown in Fig. 5-8b. Fig. 5-9 shows the overall engineering stress-strain curve and the contour plots of the equivalent plastic strain in the vicinity of the stress peak, point (a), and at a strain level of 0.2, point (b). Fig. 5-9 a shows that in the vicinity of stress peak, multiple shear bands have formed, with the location and "waviness" of the bands controlled by the initial heterogeneity of the free volume in the specimen. Note, however, that the maximum equivalent plastic strain ($\equiv \int_0^t \nu(\chi)\, d\chi$) only varies a small amount between 3.1% and 3.59%. Fig. 5-9 b at a nominal axial strain of $\approx$ 20% (after substantial macroscopic strain softening) shows that a diffuse shear band pattern persists, but again the maximum equivalent plastic strain varies only a small amount between 23.2% and 27.3%.

The response of a metallic glass at high temperatures is in stark contrast to the numerically-predicted response at low temperatures (cf., e.g., Fig. 5 of Anand and Su (2005)). Even though the material exhibits relatively strong strain softening in its macroscopic stress-strain response, because of the substantially higher strain rate sensitivity of the material at high temperatures, the tendency to form intense shear bands is substantially diminished, and the material deforms more-or-less "homogeneously."

5.5.2 Plane-strain strip bending

We have previously conducted a simulation of plane-strain bending of a strip of a Zr-based metallic glass at room temperature; cf. § 9.3 of Anand and Su (2005). As expected, at this low homologous temperature, intense shear bands develop and the shear bands on the tension side of the sample extend farther into the sample than do those on the compression side, and the shear strains in the bands on the tension side are also much higher. The shear band pattern observed in our simulation was very similar to that which was observed by Conner et al. (2003) in their experiments (their Fig. 1).

We have repeated such a simulation for the Pd-based glass, this time deformed at a high homologous temperature of 556K. As shown schematically in Fig. 5-10 (a), the strip is clamped between a pair of rigid dies, and then a rigid mandrel is moved upwards to bend the strip about the nose-radius of the upper die. The simulation was carried out using frictionless conditions between the strip and the dies/mandrel. The plastically deformed strip with contours of the equivalent plastic strain is shown in Fig. 5-10 (b). Unlike Fig. 9b,c of Anand and Su (2005) which showed very distinct shear band formation in bending at a low homologous temperature, our Fig. 5-10 (b) for the high temperature bending shows that because of the high strain rate sensitivity of the material the equivalent plastic strain is distributed relatively evenly along the edges of the bent strip and changes gradually from the surface to the interior of the strip.

5.5.3 Micro-hot-embossing

As a final example we show the results of a numerical simulation of a micron-scale hot-embossing of the Pd-based glass at 556K. The feature to be embossed is a cylindrical pillar with a radius of 50 μm and a height of 75 μm. The axi-symmetric geometry of the finite element mesh for the workpiece and the rigid die used in the simulation is shown in Fig. 5-11 (a). The workpiece has a thickness of 75 μm and a radius of 150 μm, and is meshed using 5000 ABAQUS-CAX4R axi-symmetric elements. The bottom and right edges of the workpiece are fixed and not allowed to move. The surface

interaction between the die and the metallic glass is assumed to be frictionless. The die is pushed down to emboss the workpiece and its motion is reversed after $10\,\mu$m of travel. The plastically deformed workpiece with contour plots of equivalent plastic strain is shown in Fig. 5-11 (b). Fig. 5-11 (c) shows a three-dimensional view of the embossed pillar, and Fig. 5-11 (d) gives the die load-versus-displacement curve for the embossing process. At this high homologous temperature the simulation shows that the metallic glass is successfully embossed. The simulation also provides important information such as the final shape of the product, plastic strain distribution inside the material, and the force required to successfully emboss the material.

5.6 Concluding remarks

We have extended the elastic-viscoplastic constitutive model of Anand and Su (2005) for amorphous metals to the high homologous temperature regime, and specialized the constitutive equations appearing in this theory to model the response of metallic glasses in the temperature range $0.7\vartheta_g \lessapprox \vartheta \lessapprox \vartheta_g$ and strain rate range $[10^{-5}, 10^{-2}]\,\mathrm{s}^{-1}$. The new model has been implemented in the finite element program ABAQUS/Explicit (2004) by writing a user material subroutine, and representative examples of the numerical capability to simulate high temperature deformation processing operations has been demonstrated.

A particularly important characteristic of metallic glasses is their intrinsic homogeneity to the nanoscale because of the absence of grain boundaries. This characteristic, coupled with their unique mechanical properties (high strength, large elastic strain limit, respectable toughness, good corrosion resistance) make them ideal materials for fabricating nano- or micro-meter scale components, or high-aspect-ratio nano/micro-patterned surfaces for a variety of applications such as data storage technologies, optical and medical devices, and micro-electromechanical systems. We anticipate that an important future fabrication process for nano- or micro-meter scale components will be hot-embossing/forming in the supercooled liquid range $\vartheta_g \lessapprox \vartheta \lessapprox \vartheta_x$ where the metallic glasses are known to show superplastic behavior at sufficiently slow strain rates (schroers, 2005; Inoue, 2000). Special experimentally-verified con-

stitutive equations in this important temperature and strain rate range remain to be developed. The theory outlined in this paper should provide a solid foundation for the development of such special constitutive equations for important emerging applications of these materials at the small scale.

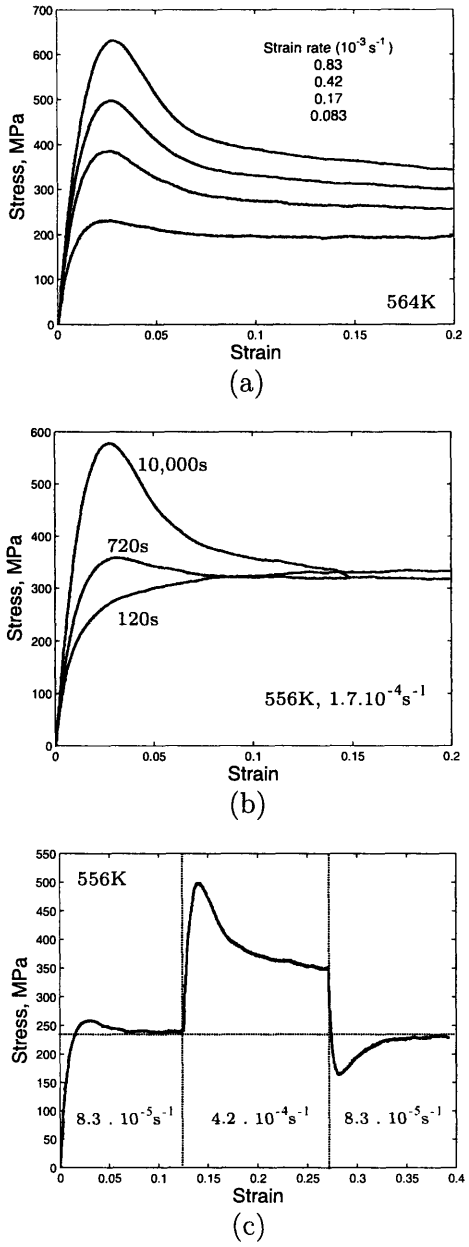

Figure 5-1: True stress-strain curves for $Pd_{40}Ni_{40}P_{20}$ from de Hey et al. (1998): (a) Pre-annealed at 564K for 5000 s, then tested at 564K at the different strain rates indicated in the figure. (b) Pre-annealed at 556K for 120, 720, and 10,000 seconds, respectively, then tested at 556K at a strain rate of $\dot{\epsilon} = 1.7 \times 10^{-4}\, s^{-1}$. (c) Pre-annealed at 556K for 3600 seconds, and then subjected to a strain rate increment-and-decrement experiment at 556K.

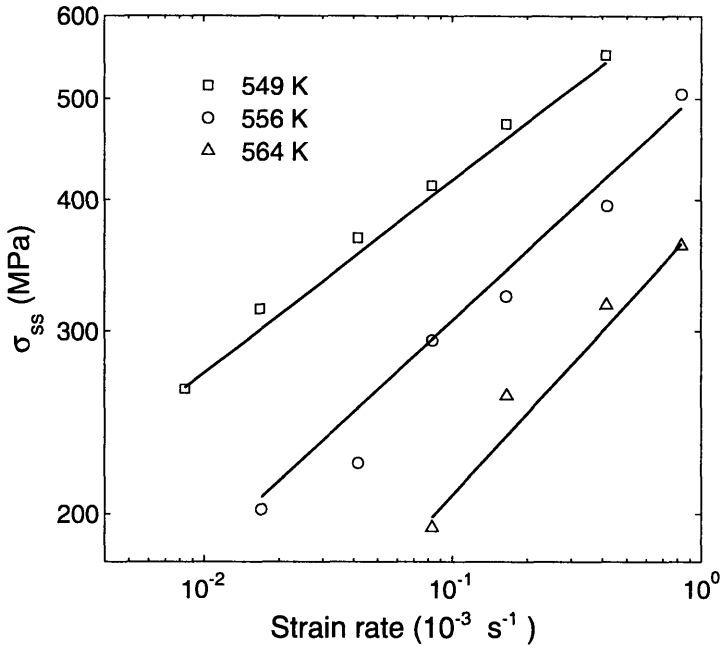

Figure 5-2: Steady state flow stress σ_{ss} as a function of strain rate $\dot{\epsilon}$ at three different temperatures. The symbols represent experimental results from de Hey et al. (1998), and the lines are from the model.

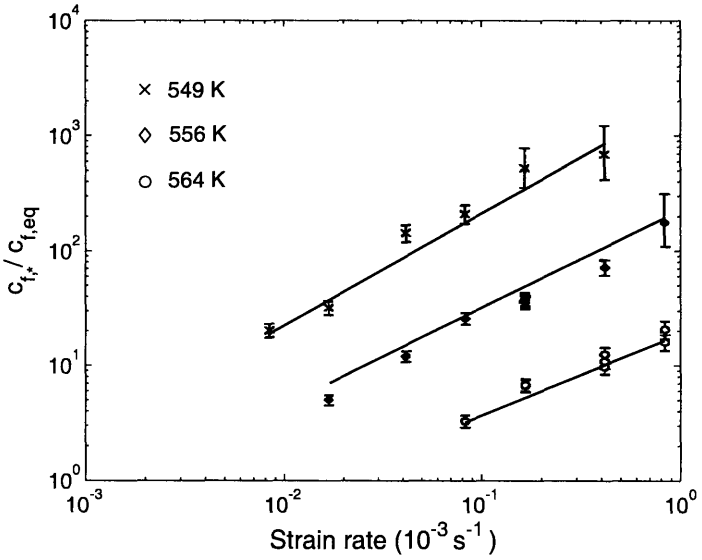

Figure 5-3: The normalized steady state flow defect concentration as a function of strain rate at three different temperatures. The symbols represent experimental results from de Hey et al. (1998), and the lines are from the model.

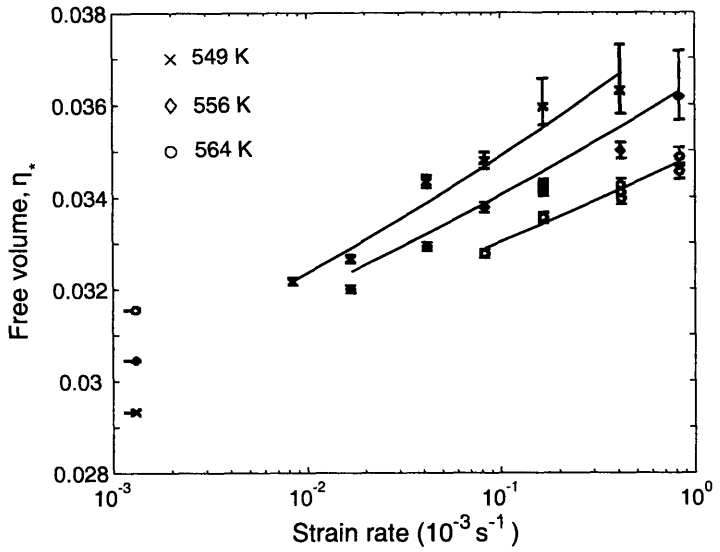

Figure 5-4: The steady state free volume η_*, as a function of strain rate at three different temperatures. The symbols represent experimental results from de Hey et al. (1998), and the lines are from the model.

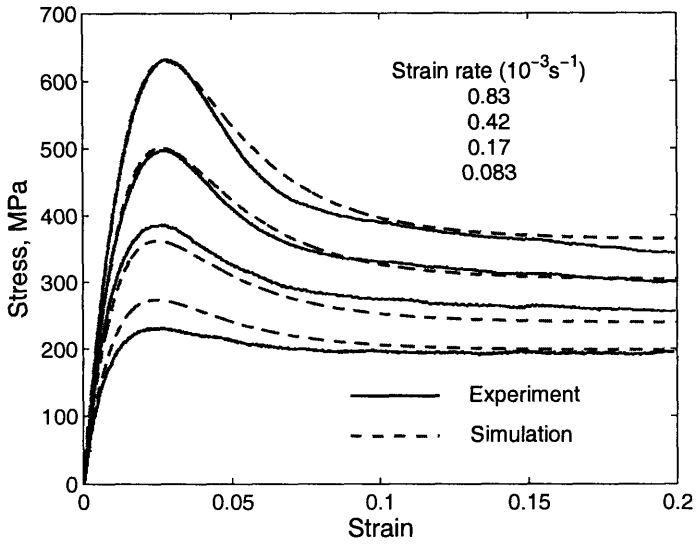

Figure 5-5: True stress-strain curves for $Pd_{40}Ni_{40}P_{20}$, pre-annealed at 564K for 5000 s, tested at 564K at different strain rates. The solid lines represent experimental results from de Hey et al. (1998), and the dashed lines are from the model.

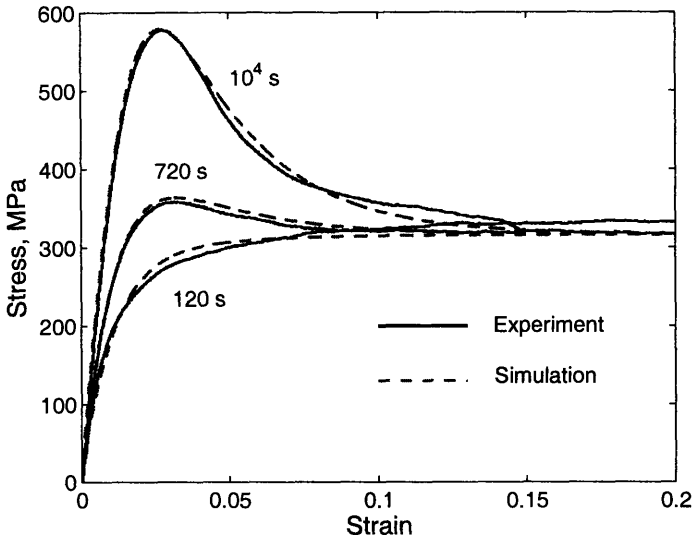

Figure 5-6: True stress-strain curves for $Pd_{40}Ni_{40}P_{20}$, pre-annealed at 556K for 120 s, 720 s, and 10,000 s, respectively, and tested at 556K and $\dot{\epsilon} = 1.7 \times 10^{-4}\, s^{-1}$. The solid lines represent experimental results from de Hey et al. (1998), and the dashed lines are from the model.

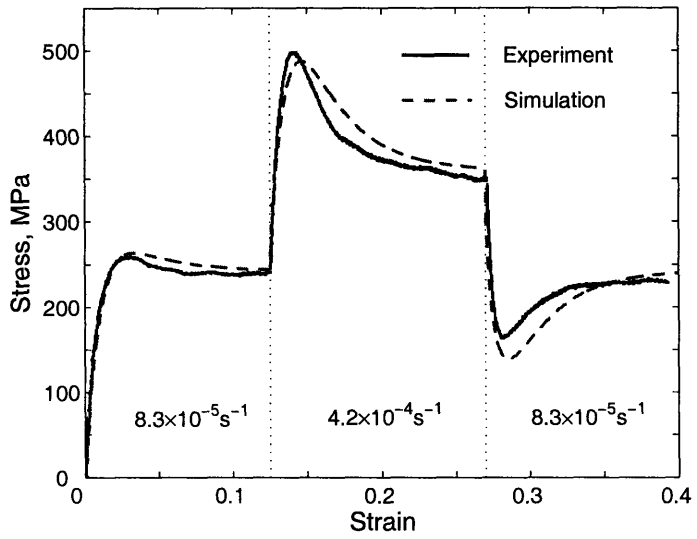

Figure 5-7: True stress-strain curves for $Pd_{40}Ni_{40}P_{20}$, pre-annealed at 556K for 3600 seconds, and then subjected to a strain rate increment-and-decrement experiment at 556K. The solid lines represent experimental results from de Hey et al. (1998), and the dashed lines are from the model.

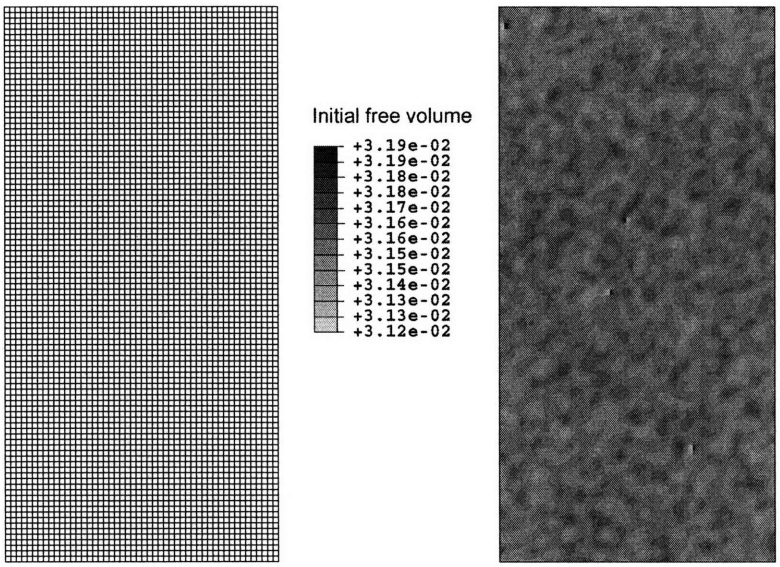

(a) (b)

Figure 5-8: (a) Finite element mesh consisting of 5000 ABAQUS-CPE4R elements for the two-dimensional plane strain tension simulation. (b) Contour plot of the distribution of the initial free volume.

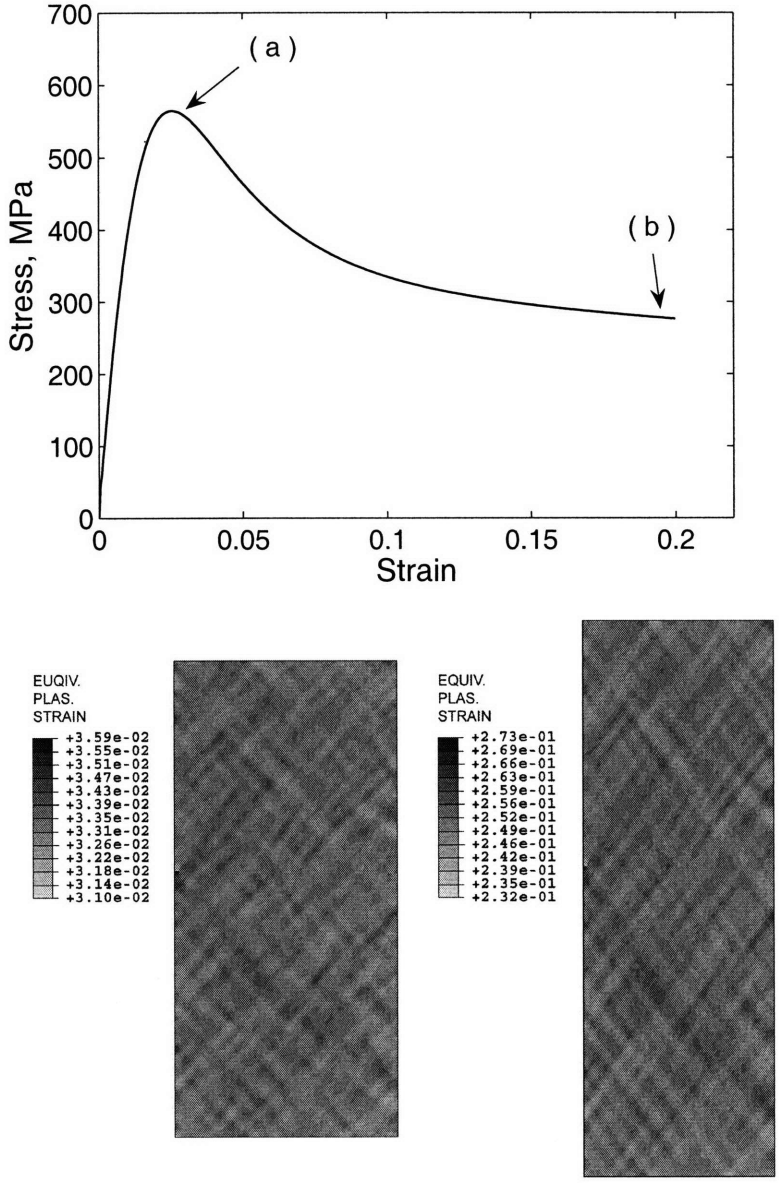

Figure 5-9: Engineering stress-strain curve from a two-dimensional plane strain tension simulation. Contour plots of the equivalent plastic strain keyed to two points on the stress-strain curve are also shown: (a) in the vicinity of the stress peak; (b) when the stress reaches the steady state value.

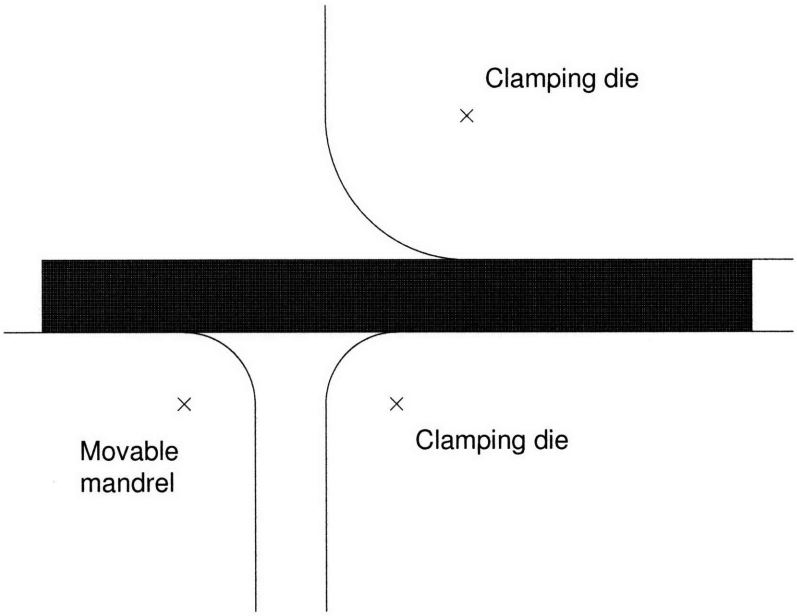

(a)

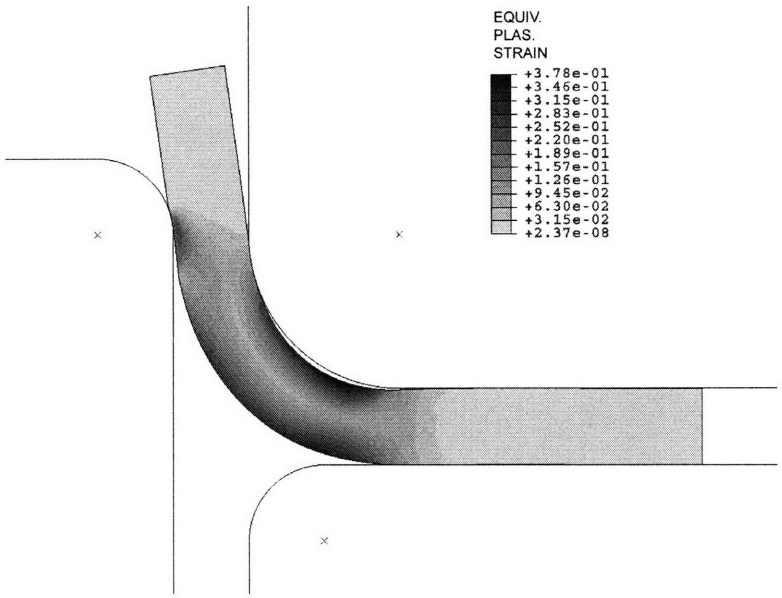

(b)

Figure 5-10: Simulation of bending of a strip of a Pd-based metallic glass at 556K. (a) The strip is clamped between a pair of rigid dies, and then the rigid mandrel is moved upwards to bend the strip about the radius of the upper die. (b) Deformed strip showing contour plots of the equivalent plastic strain.

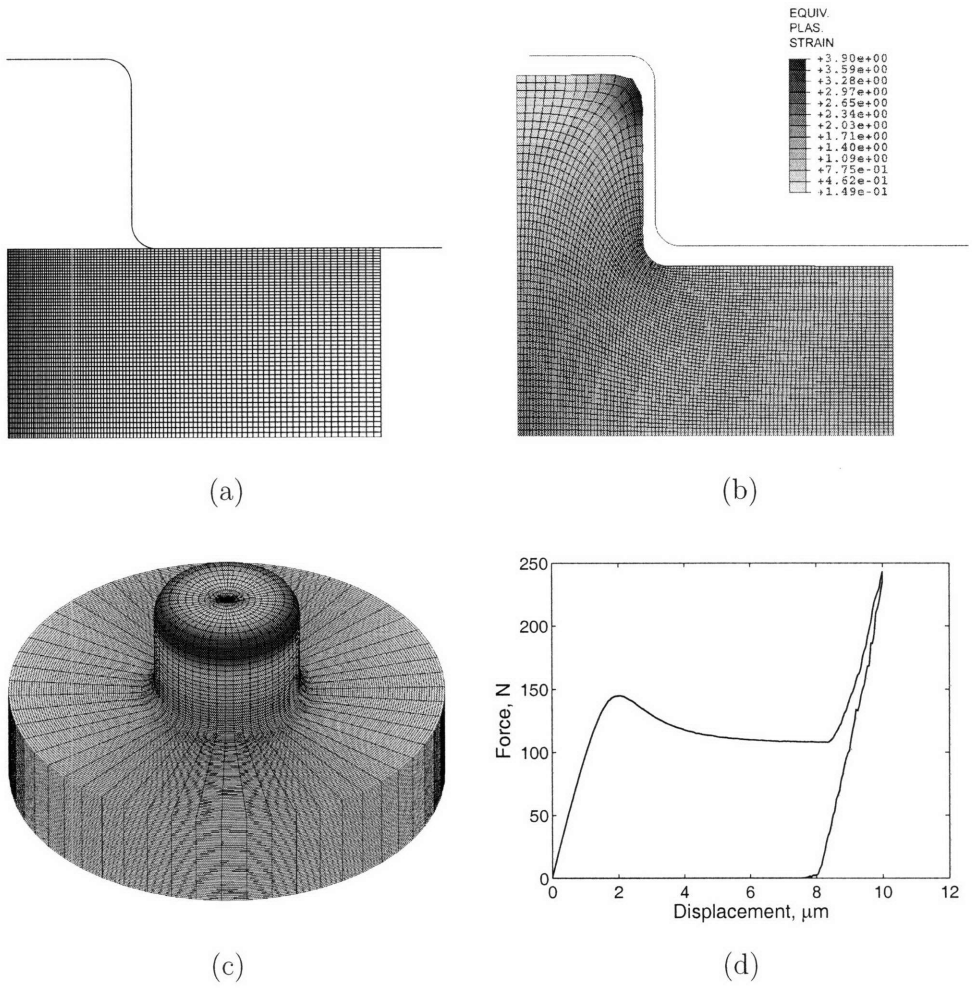

Figure 5-11: (a) Initial finite element mesh for the axi-symmetric micro hot-embossing simulation. (b) Deformed mesh after the die is reversed. Contour plot of the equivalent plastic shear strain is also shown. (c) A three-dimensional view of the embossed pillar. (d) Die load versus displacement during embossing. Observe the sharp increase of the load when the material fully fills the die.

Chapter 6

A computational study of the mechanical behavior of a prototypical amorphous grain-boundary

6.1 Introduction

Nanocrystalline metals are polycrystalline metallic materials with grain sizes typically less than 100 nm. These materials have been the subject of intense, world-wide research over the past two decades, and due to this research activity the micromechanisms governing their macroscopic mechanical behavior are now beginning to be better understood (e.g., Gleiter, 2000; Weertman, 2002). Recent reviews on the topic, and references to the vast amount of literature, may be found in Kumar et al. (2003) and Wolf et al. (2005). Nanocrystalline metals contain a high volume fraction of "grain-boundary"-intercrystalline regions. For example, idealizing a unit cell containing a crystalline grain interior and an intercrystalline grain-boundary region as a sphere of diameter d, with an intercrystalline shell of thickness δ and a crystalline core of diameter $d - 2\delta$, the volume fractions of grain-boundary regions for a fixed value of $\delta \sim 0.5\,\text{nm}$, and grain sizes d of 10 nm and 40 nm are 27.1 % and

7.3 %, respectively. Thus, a substantial fraction of the atoms in nanocrystalline materials lie in the intercrystalline grain-boundary regions, and these regions play an increasingly significant role as the grain size decreases below the 100 nm level. The nature of the intercrystalline grain-boundary regions depends on how the material has been processed. High-resolution transmission electron microscopy (TEM) studies on nanocrystalline materials show that while many grain boundaries appear sharp and well-defined, others show considerable disorder, with the maximum disordered region (measured perpendicular to grain boundaries) being approximately 2 to 3 lattice spacings; i.e., less than 1 nm (Ranganathan et al., 2001).

As reviewed in (Kumar et al., 2003; Wolf et al., 2005), much of the understanding of the micromechanisms operative during the inelastic deformation of nanocrystalline materials has been obtained from large-scale molecular dynamics (MD) studies published in the past few years. Although MD methods of studying atomic-level mechanical response of materials are useful for gaining valuable insight, these methods are at present not suitable for carrying out simulations of deformation and failure under conditions similar to those under which physical experiments on nanocrystalline materials are carried out: i.e., macroscopic-sized specimens with complicated boundary conditions, involving realistic strain rates. MD simulations are inherently limited to small, idealized microstructures and extremely high strain rates, typically $> 10^7$/s, which corresponds to a strain of 1% in 1 ns.

In contrast to MD methods, finite-element methods (FEM) for simulation of micromechanical interactions and prediction of local as well as overall response of materials have been effectively used to study the mechanical response of variety of composite material systems in recent years, and such methods do not possess the major limitations of the MD methods listed above. However, use of continuum-mechanical-based FEM methods is contingent upon the assumptions of continuum mechanics — suitable smoothness of displacement fields, the notion of stress, and balance laws of linear and angular momentum — continuing to hold at the nanoscale. Further, just as the results from MD simulations depend crucially on the reliability of the interatomic potentials used in such studies, the results of FEM simulations depend crucially on the reliability of the continuum-level constitutive equations used in such

analyses. While the concepts of continuum elasticity are expected to be approximately applicable at small scales approaching the nano-level, the concepts of classical continuum plasticity being applicable at this scale are highly questionable. Nevertheless, based on a *pragmatic engineering approach*, and bolstered by the success of (length-scale-independent) crystal-plasticity theories and attendant FEM simulation methodologies to represent grain-scale shear localization phenomena and texture evolution (cf., e.g, Anand and Kalidindi, 1994), a few investigators have recently carried out continuum-level FEM simulations of the inelastic deformation and failure response of nanocrystalline materials (cf., e.g, Wei and Anand, 2004; Warner et al., 2006). Although in their infancy, such FEM-based simulations also provide valuable insights on the deformation and failure response of nanocrystalline materials; insights which cannot solely be obtained from atomistic simulations or physical experiments.

For example, Wei and Anand (2004) coupled a single-crystal plasticity constitutive model for the grain interior, with a cohesive interface constitutive model to account for grain-boundary sliding and separation phenomena. They recognized that a standard crystal plasticity model for the grain-interior deformation, which implicitly assumes enough dislocation nucleation and multiplication to result in a sufficiently smooth macroscopic response, is inadequate to represent the limited amount of inelastic deformation due to emission and eventual absorption of the relatively fewer (partial or complete) dislocations from grain boundaries in nanocrystalline materials. However, since elastic anisotropy and crystallographic texture effects are still important in nanocrystalline materials, and since the few dislocations in these materials are still expected to move on slip systems, the mathematical structure of a continuum crystal plasticity theory is still useful as an *indicator* of the limited inelasticity due to crystalline slip within the nanocrystalline grains. Their cohesive interface model for grain boundaries accounts for both reversible elastic, as well irreversible inelastic sliding-separation deformations at the grain boundaries prior to failure. The tensile and shear properties of the cohesive grain boundaries were estimated by fitting results of numerical simulations to experimentally-measured stress-strain curves for nanocrystalline electrodeposited Ni. Unfortunately, such a fitting procedure makes it difficult to unambiguously characterize the grain-boundary properties, and they

used a value for the shear strength of the grain boundaries which was very similar in magnitude to the tensile strength of the boundaries; as is clear from the recent atomistic simulations of grain-boundary response by Sansoz and Molinari (2004), this assumption is clearly unrealistic. Also, Wei and Anand (2004) restricted their models for the grain interiors and grain boundaries to be completely rate-independent.

Warner et al. (2006), following the methodology of Wei and Anand (2004), have also used a continuum FEM method to model the plastic deformation of nanocrystalline copper by using crystal plasticity for the grain interiors and cohesive elements for grain boundaries. For the traction-separation relations for the grain boundaries, they obtained estimates for the shear and normal response of the boundaries from quasi-continuum atomistic calculations. Since their atomistic calculations were carried out at 0 K, they had to use a *large* ad-hoc *thermal-correction* (cf., their eq. (8)) to estimate the shear strength for the grain boundaries in Cu at room temperature.

As is clear from our brief review, continuum-level FEM simulations of the inelastic deformation and failure response of nanocrystalline materials are still in their infancy. Much needs to be done to refine the constitutive models, specially for the the traction-separation relations in approaches using cohesive elements to represent grain-boundaries.

Motivated by the fact that *amorphous metals are the ultimate limit for nanocrystalline metals, as the crystal grain size decreases to zero*, in this chapter, we develop a slightly modified version of the continuum theory for amorphous metals which accounts for cavitation and related failure phenomena to represent the intercrystalline grain-boundary regions. With the continuum amorphous theory, we carry out a FEM computational study of the mechanical behavior of an amorphous grain-boundary region in nanocrystalline metals.

The plan of this chapter is as follows. In §6.2 we expand the amorphous constitutive model to account for the cavitation mechanism and related failure phenomena driven by the principal and hydro-static stresses. In §6.3 we simulate the behavior of an amorphous grain-boundary region in nanocrystalline metals. We close in §6.4 with some final remarks.

6.2 Constitutive theory

6.2.1 The cavitation mechanism

To account for the cavitation mechanism, we expand the evolution equation for $\mathbf{F}^p$ as

$$\dot{\mathbf{F}}^p = \mathbf{D}^p \mathbf{F}^p, \quad \mathbf{D}^p = \mathbf{D}^{p\top}, \quad \text{with} \quad \mathbf{D}^p = \mathbf{D}^p_s + \mathbf{D}^p_c, \tag{6.1}$$

where the plastic stretching $\mathbf{D}^p$ is taken to arise from a shearing contribution $\mathbf{D}^p_s$ controlled by the local shear stresses, and a cavitating/volumetric contribution $\mathbf{D}^p_c$ controlled by the local tensile principal stresses and the local mean normal stress. The shearing contribution is the same as we have discussed in Chapter 2. And the constitutive equation for cavitating/volumetric contribution $\mathbf{D}^p_c$ to the plastic stretching is taken to be given by

$$\left.\begin{aligned} &\mathbf{D}^p_c = \sum_{i=1}^{3} \nu_c^{(i)} (\hat{\mathbf{e}}_i \otimes \hat{\mathbf{e}}_i), \quad \text{with} \quad \nu_c^{(i)} = \begin{cases} \nu_0 \left\{ \dfrac{\sigma_i}{\sigma_{cr}} \right\}^{1/m} & \text{if } \sigma_i > 0, \\ 0 & \text{if } \sigma_i \leq 0, \end{cases} \\ &\sigma_{cr} = c_1 - c_2 \bar{\sigma}_h > 0, \end{aligned}\right\} \tag{6.2}$$

where $\bar{\sigma}_h = (1/3)(\sigma_1 + \sigma_2 + \sigma_3)$ is the mean normal stress (hydrostatic tension), and c_1 and c_2 are material parameters. In this model the contribution $\nu_c^{(i)}(\hat{\mathbf{e}}_i \otimes \hat{\mathbf{e}}_i)$ to $\mathbf{D}^p_c$ is zero if the principal stress σ_i is zero or negative. When σ_i is positive, its value relative to the value of a parameter $\sigma_{cr} = \hat{\sigma}_{cr}(\bar{\sigma}_h)$, which depends on the hydrostatic tension, controls the magnitude of $\nu_c^{(i)}$. The value of σ_{cr} is taken to decrease linearly as the hydrostatic tension $\bar{\sigma}_h$ increases. For simplicity, the reference strain rate ν_0, and the rate sensitivity parameter m in (6.2) are taken to be the same as that in (2.77). Note that (6.2) predict a *spherical* inelastic cavitation only when all the principal stresses are equal to each other, $\sigma_1 = \sigma_2 = \sigma_3$. In situations where the principal stresses are unequal, the "cavitation" is predominantly in the direction of the maximum principal stress σ_1 because of the power-law nature of the relation (6.2).

6.2.2 Modeling damage and failure in the cavitation mechanism

We use the following simple critical-strain-based criteria to model damage and failure in the cavitation mechanism. Let $\tilde{\epsilon}^p = |\mathbf{D}_c^p|$ define a volumetric strain rate, and

$$\epsilon^p \stackrel{\text{def}}{=} \int_0^t \tilde{\epsilon}^p(\xi)\, d\xi, \tag{6.3}$$

define a volumetric plastic strain. Then, as a simple model for damage by inelastic cavitation, we introduce a damage variable D defined by

$$D \stackrel{\text{def}}{=} \begin{cases} 0 & \text{if } \epsilon^p \leq \epsilon_{cr}^p, \\ \dfrac{(\epsilon^p - \epsilon_{cr}^p)}{(\epsilon_f^p - \epsilon_{cr}^p)} & \text{if } \epsilon_{cr}^p < \epsilon^p < \epsilon_f^p, \\ 1 & \text{if } \epsilon^p \geq \epsilon_f^p, \end{cases} \tag{6.4}$$

whose value is zero for ϵ^p less than a critical value ϵ_{cr}^p, and thereafter $D = (\epsilon^p - \epsilon_{cr}^p)/(\epsilon_f^p - \epsilon_{cr}^p)$, so that the damage variable evolves linearly towards a value of unity as ϵ^p evolves to a failure value ϵ_f^p. Correspondingly, the σ_{cr} in (6.2) is decreased linearly towards a value of zero $\sigma_{cr} = \{c_1 - c_2\bar{\sigma}_h\} \times (1 - D)$. Further, to account for damage to the elastic properties, the elastic shear and bulk moduli G and K are replaced by $G \times (1 - D)$ and $K \times (1 - D)$ when damage occurs. As D approaches unity, the material is deemed to have "failed" by cavitation, and it is "removed" from the finite element calculation; in actual numerical implementation, in order to avoid numerical singularities, failure due to cavitation is deemed to have occurred when the damage parameter D reaches a suitably large number, say ~ 0.995. The damage model outlined above is quite rudimentary, and much work needs to be done to develop more realistic models for the transition from shear plasticity, to damage and final fracture.

6.3 Behavior of a prototypical amorphous grain-boundary

In this section we consider the deformation and failure response of a prototypical "grain-boundary" as modelled by our theory for amorphous materials. Fig. 6-1 a shows a finite-element model of an amorphous grain-boundary region "GB" sandwiched between elastic layers "A". The bottom edge of the sandwiched layer is held fixed, while $\underline{\mathbf{u}}$ denotes the displacement of the top edge. Several material parameters are required in the constitutive model to describe the mechanical behavior of an amorphous grain-boundary. These include the elastic shear moduli G and K, the cohesion c, the frictional coefficient μ, the viscoplasticity parameters ν_0 and m; the critical strains for cavitation failure $\epsilon_{c,cr}$ and $\epsilon_{c,f}$, and the parameters c_1 and c_2 controlling the evolution of cavitation resistance σ_{cr}. In this section we have chosen representative values to qualitatively demonstrate the mechanical response of a grain-boundary. In order to model the *heterogeneity* of the grain boundaries, the initial value of the cohesion c for each grain-boundary element was randomly assigned a value from a list which had values of c uniformly distributed between 510 and 590 MPa. Fig. 6-1 b shows a contour plot of the initial value of c in the grain-boundary region.

We first simulated the deformation of such an interface region to macroscopic simple shear, Fig. 6-2 a. In this simulation we *suppressed* the cavitation mechanism. The nominal shear stress versus shear strain response of the grain-boundary region using representative values of material parameters for the amorphous layer is shown in Fig. 6-2 b. A contour plot of the equivalent plastic strain, exhibiting inhomogeneous deformation involving "shear bands" in the grain-boundary region after a nominal macroscopic shear strain of 50% is shown in Fig. 6-2 c.

Next, cavitation failure in grain-boundary elements is also allowed. The top edge of the sandwich layer, cf. Fig.6-1, was given displacements $\underline{\mathbf{u}}_{90}$, $\underline{\mathbf{u}}_{45}$, and $\underline{\mathbf{u}}_{0}$, respectively. Figs. 6-3 a and b, respectively, show the resulting normal traction versus normal strain, and tangential traction versus tangential shear strain curves from the three simulations. Fig. 6-3 c shows the failure pattern corresponding to the point "X" marked on the normal traction versus normal strain curve in Fig. 6-3a for the case

$\underline{\mathbf{u}}_{90}$. Cavities initiate in the grain-boundary region, grow and coalesce very quickly, and result in a progressive drop of the traction in the normal direction. Fig. 6-3 d shows the failure pattern corresponding to the point "X" marked on the normal traction versus normal strain curve in Fig. 6-3a for the case $\underline{\mathbf{u}}_{45}$. Finally, Fig. 6-3 e shows the failure pattern corresponding to the point "a" marked on the tangential traction versus shear strain curve in Fig. 6-3b for the case $\underline{\mathbf{u}}_{0}$. The tangential traction versus shear strain curve shown in Fig. 6-3 b indicates that even though there is some damage which initiates in the highly constrained regions, Fig. 6-3 c, the shear strength of the grain-boundary decreases only slightly in simple shear.

6.4 Concluding remarks

We extended our amorphous constitutive theory by adding in a cavitation mechanism to model the failure phenomenon caused by the principal and hydro-static stresses. With the revised theory we studied the response of a prototypical amorphous grain-boundary. Coupled with appropriate crystal-plasticity constitutive model to represent the grain interior, the result obtained in this chapter is applied to study the deformation and failure behavior of nanocrystalline fcc metals (Wei, Su, and Anand, 2006).

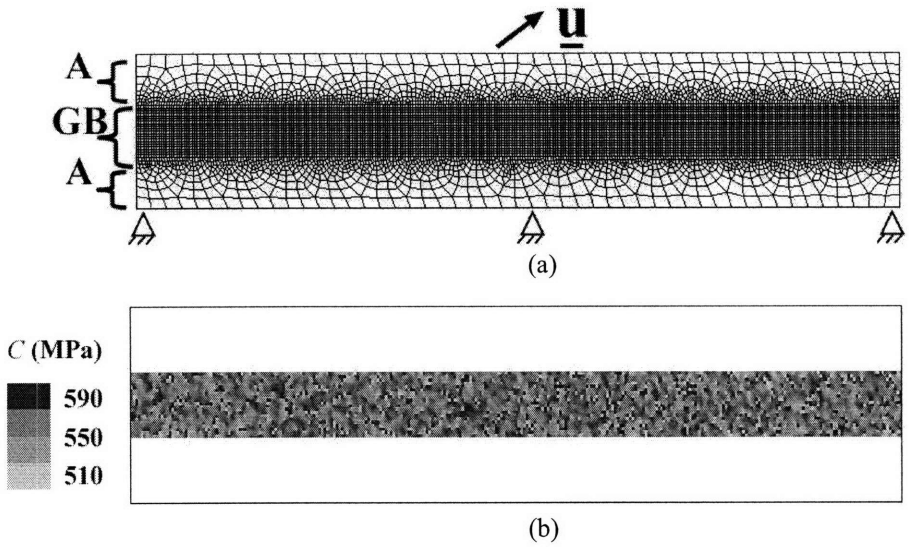

Figure 6-1: (a) An amorphous grain-boundary region "GB" sandwiched between elastic layers "A". The bottom edge of the sandwiched layer is held fixed, while $\underline{\mathbf{u}}$ denotes the displacement of the top edge (b) A contour plot of the initial cohesion c assigned to the grain-boundary elements before deformation; the initial value of c for each grain-boundary element was randomly assigned a value from a list which had values of c uniformly distributed between 510 and 590 MPa.

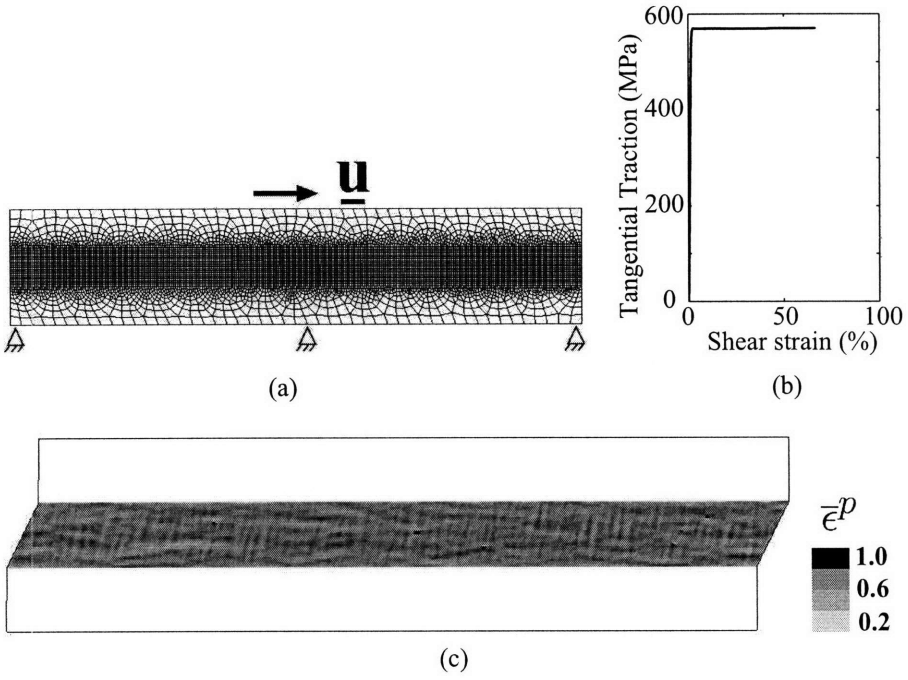

Figure 6-2: (a) Shear response of an amorphous grain-boundary region. The bottom edge of the sandwiched layer is held fixed, while the top edge is displaced by $\underline{\mathbf{u}}$ to produce a simple shear deformation. (b) Nominal shear stress versus shear strain response of the grain-boundary region in simple shear, using representative values of material parameters for the amorphous layer. (d) A contour plot of the equivalent plastic strain, showing inhomogeneous deformation in grain-boundary region after a shear strain of 50%.

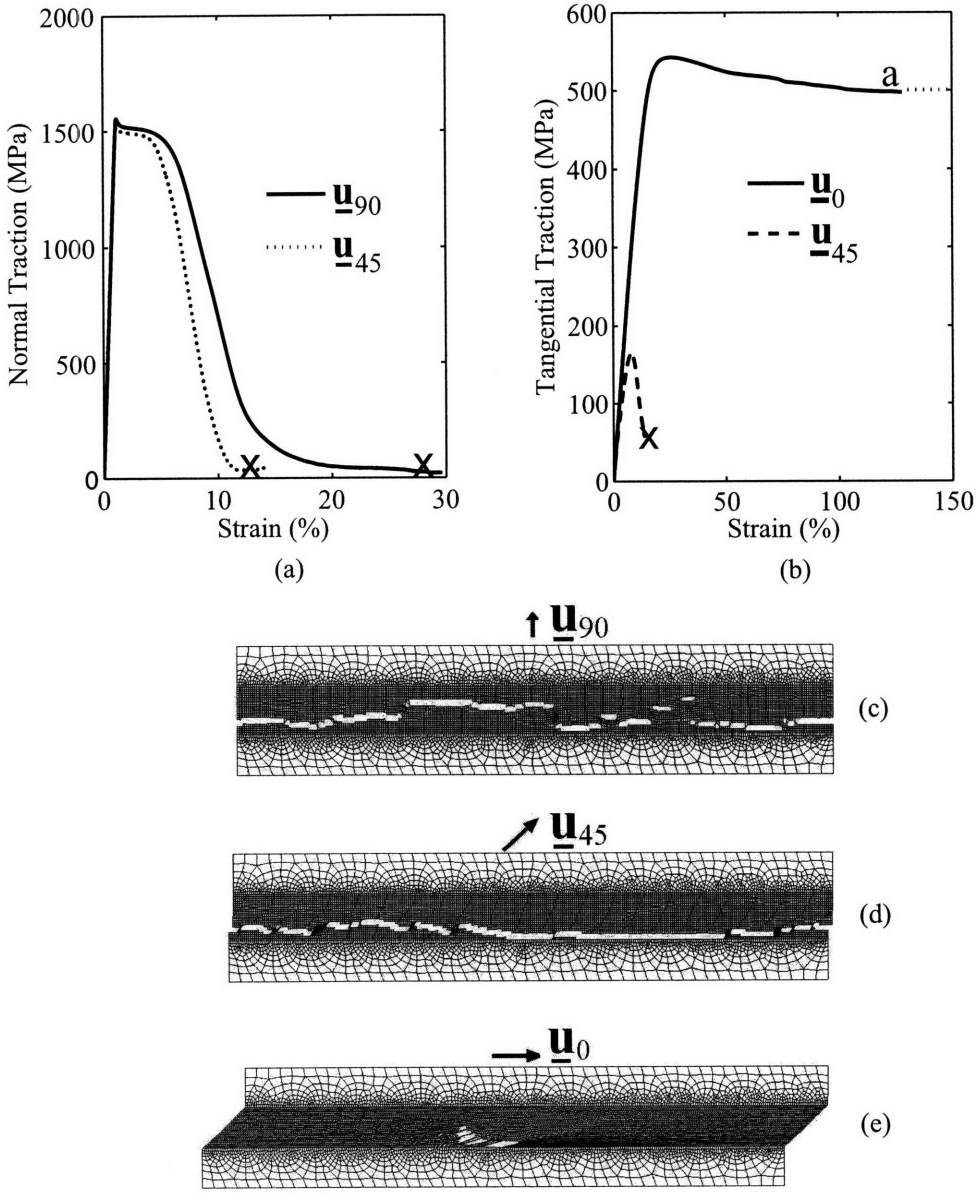

Figure 6-3: (a) Normal traction versus nominal normal strain of the amorphous layer for $\underline{\mathbf{u}}_{90}$ and $\underline{\mathbf{u}}_{45}$. (b) Tangential traction versus nominal shear strain of the amorphous layer for $\underline{\mathbf{u}}_0$ and $\underline{\mathbf{u}}_{45}$. (c) Failure pattern of the amorphous grain-boundary region subject to normal displacement $\underline{\mathbf{u}}_{90}$. (d) Failure pattern for $\underline{\mathbf{u}}_{45}$. (e) Failure pattern for $\underline{\mathbf{u}}_0$.

Appendix A

An elastic-plastic interface constitutive model : application to adhesive joints

An interface constitutive model which accounts for both reversible elastic, as well as irreversible inelastic separation-sliding deformations at the interface prior to failure has been developed and implemented in a finite-element computer program. A set of experiments has been conducted to determine the constitutive parameters in the interface model for adhesively-bonded components made from an aluminum alloy and a ductile polymeric adhesive. The constitutive model and the computational capability are shown to reasonably well predict the macroscopic deformed geometries and the load-displacement curves in (a) T-peel experiments; (b) four-point bend experiments on bonded bi-layer edge-notch specimens; and (c) lap-shear experiments.

A.1 Introduction

Cohesive interfaces between bodies in natural and man-made systems are ubiquitous, and the initiation and development of fracture by sliding and separation at such interfaces is widely observed. Common examples are (i) at the geological scale, the boundaries between the plates on the surface of the earth are cohesively bonded at asperity

contacts, and the initiation and development of relative sliding between plate boundaries often results in earthquakes; (ii) at the scale of engineering structures, many systems are built by adhesively bonding different components, and the mechanical failure of such systems often occurs because of the failure of the bonded interfaces; and (iii) at the microscopic level, in metallic, ceramic and rock-like polycrystalline materials, fracture initiation and propagation due to grain boundary interface failure is also a relatively common occurrence.

Cohesive interface modelling of fracture started more than 40 years ago with the work of Barenblatt (1959) and Dugdale (1960). In recent years, cohesive surface models have been widely used to numerically simulate fracture initiation and growth by the finite-element method (cf., e.g., Needleman (1990); Xu and Needleman (1994); Camacho and Ortiz (1996)); for a recent review see Hutchinson and Evans (2000). Typically, a set of cohesive surfaces are introduced in the finite element discretization by the use of special interface elements which obey a non-linear interface traction-separation constitutive relation which provides a phenomenological description for the complex microscopic processes that lead to the formation of new traction-free crack faces. The loss of cohesion, and thus of crack nucleation and extension, occurs by the progressive decay of interface tractions. The interface traction-separation relation usually includes a cohesive strength and cohesive work-to-fracture. Once the local strength and work-to-fracture criteria across an interface are met, decohesion occurs naturally across the interface, and traction-free cracks form and propagate along element boundaries. An important characteristic of this methodology for modelling fracture initiation and propagation is that macroscopic fracture criteria, based on elastic or elastic-plastic analyses, such as $K_I = K_{IC}$ or $J_I = J_{IC}$, are not needed, because material strength and toughness, and crack nucleation and propagation, are all characterized by the local traction-separation relation and the cohesive surface methodology.

Although substantial progress has been made in recent years, there are still several key issues that need to be addressed in the cohesive surface modelling of fracture. Specifically, (i) Most previous interface models are of the *non-linear reversible elastic* type. For example, in Xu and Needleman (1994), with $\boldsymbol{\delta}$ denoting the displacement

jump across the cohesive surface, and $\mathbf{t}$ the work-conjugate traction vector on the surface, the constitutive equation for the cohesive surfaces is expressed in terms of a potential function φ, such that the traction $\mathbf{t} = \partial\varphi/\partial\boldsymbol{\delta}$. The specific form for φ chosen by Xu and Needleman (1994) is history- and rate-independent, and this leads to a traction-displacement relation which is fully reversible. It appears that the interface constitutive model of Xu and Needleman (1994) is intended to represent the cohesive behavior of *initially defect free* interfaces, and thus in some sense to describe the *ideal strength* of solids. There exists a need to develop interface constitutive models which allow for *inelasticity* at the interface prior to failure, much in the spirit of elastic-plastic constitutive equations which govern the deformation of the bulk material.[1] (ii) While it is relatively straightforward to construct a traction-separation relation for normal separation across an interface to model mode I conditions, elastic-plastic traction-separation relations for combined opening and sliding, together with the experimental methods needed to determine the parameters that might enter such coupled interface constitutive relations, are not well-developed.[2]

The purpose of this paper is to present a continuum-level interface constitutive model which accounts for both reversible elastic, as well irreversible inelastic separation-sliding deformations at the interface prior to failure. We have implemented our constitutive model in the finite-element computer program ABAQUS/Explicit (2004) by writing a USER INTERFACE subroutine. As a first application of our model we consider the widely studied problem of modelling the behavior of adhesively-bonded components.[3] We show that our new model, when suitably calibrated against a set of experiments to determine the constitutive parameters for aluminum components bonded by a polymeric adhesive, is able to reasonably well predict the macroscopic load-displacement curves of three different verification experiments using (a)

[1] Camacho and Ortiz (1996) do allow for a form of inelasticity. They consider interface constitutive equations in which the initial cohesive response is rigid, and there is a finite traction at which softening occurs; they also allow loading/unloading irreversibility, with linear unloading to the origin.

[2] This is true even for two-dimensional problems, and this issue is expected to be substantially more complicated in three dimensions.

[3] Cohesive interface models have been widely used to investigate interfacial failure of bi-material systems, e.g., Tvergaard and Hutchinson (1992, 1996), and Thouless and co-workers (Yang et al. (1999, 2000, 2001), Kafkalidis and Thouless (2002)). The major difference between these previous studies and the present work is the use of our new interface constitutive model.

T-peel specimens, (a) four-point bending of bi-layer edge-notch specimens, and (b) lap-shear specimens.

The plan of this chapter is as follows. In §A.2 we develop our interface constitutive model. In §A.3 we describe our experiments to calibrate the material parameters in the model for aluminum components bonded by a polymeric adhesive, and verify the predictive capabilities of our constitutive model and computational procedures for the deformation and fracture response of adhesively-bonded components. We close in §A.4 with some final remarks.

A.2 Interface constitutive model

We consider two bodies $\mathcal{B}^+$ and $\mathcal{B}^-$separated by an interface $\mathcal{I}$ (Fig. A-1). Let $\{\hat{\mathbf{e}}_1, \hat{\mathbf{e}}_2, \hat{\mathbf{e}}_3\}$ be an orthonormal triad, with $\hat{\mathbf{e}}_1$ aligned with the normal $\mathbf{n}$ to the interface, and $\{\hat{\mathbf{e}}_2, \hat{\mathbf{e}}_3\}$ in the tangent plane at the point of the interface under consideration.

Let $\boldsymbol{\delta}$ denote the displacement jump across the cohesive surface, and $\mathbf{t}$ the power-conjugate traction, such that $\mathbf{t} \cdot \dot{\boldsymbol{\delta}}$ gives the power per unit area of the interface in the reference configuration.

We assume that the displacement jump may be additively decomposed as

$$\boldsymbol{\delta} = \boldsymbol{\delta}^e + \boldsymbol{\delta}^p, \tag{A.1}$$

where $\boldsymbol{\delta}^e$ and $\boldsymbol{\delta}^p$, respectively, denote the elastic and plastic parts of $\boldsymbol{\delta}$. Then,

$$\mathbf{t} \cdot \dot{\boldsymbol{\delta}} = \mathbf{t} \cdot \dot{\boldsymbol{\delta}}^e + \mathbf{t} \cdot \dot{\boldsymbol{\delta}}^p. \tag{A.2}$$

Let φ denote a free-energy per unit surface area in the reference configuration. We consider a purely mechanical theory based on the following local energy imbalance that represents the first two laws of thermodynamics under isothermal conditions,

$$\dot{\varphi} \leq \mathbf{t} \cdot \dot{\boldsymbol{\delta}}. \tag{A.3}$$

Then, using (A.2), the field

$$\Gamma = \mathbf{t} \cdot \dot{\boldsymbol{\delta}}^e + \mathbf{t} \cdot \dot{\boldsymbol{\delta}}^p - \dot{\varphi} \geq 0 \tag{A.4}$$

represents the **dissipation** per unit area.

We assume that the free-energy φ is given by

$$\varphi = \hat{\varphi}(\boldsymbol{\delta}^e). \tag{A.5}$$

Then, using standard arguments, (A.4) gives

$$\mathbf{t} = \frac{\partial \hat{\varphi}(\boldsymbol{\delta}^e)}{\partial \boldsymbol{\delta}^e} \tag{A.6}$$

and

$$\Gamma = \mathbf{t} \cdot \dot{\boldsymbol{\delta}}^p \geq 0. \tag{A.7}$$

We are concerned with interfaces in which the elastic displacement jumps are small. For these conditions we assume a simple quadratic free-energy φ

$$\varphi = \frac{1}{2} \boldsymbol{\delta}^e \cdot \mathbf{K} \boldsymbol{\delta}^e, \tag{A.8}$$

with $\mathbf{K}$, the interface elastic stiffness tensor, positive definite. In this case (A.6) gives

$$\mathbf{t} = \mathbf{K}\boldsymbol{\delta}^e = \mathbf{K}(\boldsymbol{\delta} - \boldsymbol{\delta}^p). \tag{A.9}$$

We consider an interface model which is *isotropic* in its tangential response, and take $\mathbf{K}$ to be given by

$$\mathbf{K} = K_N \mathbf{n} \otimes \mathbf{n} + K_T(\boldsymbol{\mathcal{I}} - \mathbf{n} \otimes \mathbf{n}), \tag{A.10}$$

with $K_N > 0$ and $K_T > 0$ normal and tangential elastic stiffness moduli.

The interface traction $\mathbf{t}$ may be decomposed into normal and tangential parts, $\mathbf{t}_N$

and $\mathbf{t}_T$, respectively, as

$$\mathbf{t} = \mathbf{t}_N + \mathbf{t}_T, \quad \mathbf{t}_N \equiv (\mathbf{n} \otimes \mathbf{n})\, \mathbf{t} = (\mathbf{t} \cdot \mathbf{n})\, \mathbf{n} \equiv t_N\, \mathbf{n}\,, \quad \mathbf{t}_T \equiv (\boldsymbol{\mathcal{I}} - \mathbf{n} \otimes \mathbf{n})\, \mathbf{t} = \mathbf{t} - t_N\, \mathbf{n}. \tag{A.11}$$

The quantity t_N represents the *normal stress* at the interface. We denote the magnitude of the tangential traction vector $\mathbf{t}_T$ by

$$\bar{\tau} \equiv \sqrt{\mathbf{t}_T \cdot \mathbf{t}_T}\,, \tag{A.12}$$

and call it the *effective tangential traction*, or simply the *shear stress*.

We take the elastic domain in our elastic-plastic model to be defined by the interior of the intersection of two convex yield surfaces. The yield functions corresponding to each surface are taken as

$$\Phi^{(i)}(\mathbf{t}, s^{(i)}) \leq 0, \qquad i = 1, 2, \tag{A.13}$$

and henceforth we indentify the index $i = 1$ with a "normal" mechanism, and the index $i = 2$ with a "shear" mechanism. The scalar internal variable $s^{(1)}$ represents the deformation resistance for the normal mechanism, and $s^{(2)}$ represents the deformation resistance for the shear mechanism. In particular, we consider the following simple specific functional form for the yield functions:

$$\Phi^{(1)} = t_N - s^{(1)} \leq 0, \qquad \Phi^{(2)} = \bar{\tau} + \mu t_N - s^{(2)} \leq 0, \tag{A.14}$$

where μ represents a *friction coefficient*. The surface $\Phi^{(i)} = 0$ denotes the ith yield surface in traction space, and

$$\mathbf{n}^{(1)} = \frac{\partial \Phi^{(1)}}{\partial \mathbf{t}} = \mathbf{n}, \qquad \mathbf{n}^{(2)} = \frac{\partial \Phi^{(2)}}{\partial \mathbf{t}} = \frac{1}{\sqrt{1+\mu^2}} \left(\frac{\mathbf{t}_T}{\bar{\tau}} + \mu \mathbf{n} \right) \tag{A.15}$$

denote the outward unit normals to the yield surface at the current point in traction space; see Fig. A-2.

The equation for $\dot{\boldsymbol{\delta}}^p$, the *flow rule*, is taken to be representable as a sum of the

contribution from each mechanism

$$\dot{\boldsymbol{\delta}}^p = \sum_{i=1}^{2} \nu^{(i)} \mathbf{m}^{(i)}, \qquad \nu^{(i)} \geq 0, \qquad \nu^{(i)} \Phi^{(i)} = 0, \quad \text{with} \tag{A.16}$$

$$\mathbf{m}^{(1)} = \mathbf{n}, \qquad \mathbf{m}^{(2)} = \frac{\mathbf{t}_T}{\bar{\tau}}. \tag{A.17}$$

Note that since $\mathbf{m}^{(2)} \neq \mathbf{n}^{(2)}$, we have a *non-normal* flow rule for the shear response.

The evolution equations for the internal variables $s^{(i)}$ are taken as a pair of ordinary differential equations

$$\dot{s}^{(i)} = \sum_{j=1}^{2} h^{(ij)} \nu^{(j)}, \tag{A.18}$$

where the coefficients $h^{(ij)}$ denote hardening/softening moduli.

Finally, during inelastic deformation, an active mechanism must satisfy the *consistency condition*

$$\nu^{(i)} \dot{\Phi}^{(i)} = 0 \qquad \text{when} \qquad \Phi^{(i)} = 0. \tag{A.19}$$

The consistency condition serves to determine the inelastic deformation rates $\nu^{(i)}$ when inelastic deformation occurs. Straightforward calculations using (A.9) – (A.18) give

$$\dot{\Phi}^{(i)} = \mathbf{n}^{(i)} \cdot \mathbf{K} \dot{\boldsymbol{\delta}} - \sum_{j} \left[\mathbf{n}^{(i)} \cdot \mathbf{K} \mathbf{m}^{(j)} + h^{(ij)} \right] \nu^{(j)}.$$

For $\nu^{(i)} > 0$, when $\Phi^i = 0$ the consistency condition requires that $\dot{\Phi}^{(i)} = 0$. This gives the following system of linear equations for $\nu^{(i)} > 0$:

$$\sum_{j=1}^{2} A^{(ij)} \nu^{(j)} = b^{(i)}, \qquad A^{(ij)} = \mathbf{n}^{(i)} \cdot \mathbf{K} \mathbf{m}^{(j)} + h^{(ij)}, \qquad b^{(i)} = \mathbf{n}^{(i)} \cdot \mathbf{K} \dot{\boldsymbol{\delta}}. \tag{A.20}$$

We assume that *the matrix A is invertible*, so that the $\nu^{(j)}$ are uniquely determined.

A.2.1 Specific form for the evolution equations

Let

$$\gamma^{(1)} \stackrel{\text{def}}{=} \int_0^t \nu^{(1)}(\xi)\, d\xi, \tag{A.21}$$

$$\gamma^{(2)} \stackrel{\text{def}}{=} \int_0^t \nu^{(2)}(\xi)\, d\xi, \tag{A.22}$$

define equivalent relative plastic displacements for the two individual mechanisms, and

$$\bar{\gamma} \stackrel{\text{def}}{=} \sqrt{(\gamma^{(1)})^2 + \alpha\,(\gamma^{(2)})^2} \tag{A.23}$$

define a combined *equivalent relative plastic displacement*, where α represents a *coupling parameter* between the normal and shear mechanisms.

A simple set of evolution equations for $s^{(1)}$ and $s^{(2)}$ which represent strain-hardening response until a critical value of $\bar{\gamma} = \bar{\gamma}_c$ is reached, and a *softening response* thereafter is

$$s^{(1)} = \hat{s}^{(1)}(\bar{\gamma}), \qquad \text{with} \qquad \hat{s}^{(1)}(\bar{\gamma}) = \begin{cases} \hat{s}^{(1)}_{hard}(\bar{\gamma}) & \text{if } \bar{\gamma} \le \bar{\gamma}_c, \\ \hat{s}^{(1)}_{soft}(\bar{\gamma}) & \text{if } \bar{\gamma} > \bar{\gamma}_c \text{ and } s^{(1)} > 0. \end{cases} \tag{A.24}$$

Similarly,

$$s^{(2)} = \hat{s}^{(2)}(\bar{\gamma}), \qquad \text{with} \qquad \hat{s}^{(2)}(\bar{\gamma}) = \begin{cases} \hat{s}^{(2)}_{hard}(\bar{\gamma}) & \text{if } \bar{\gamma} \le \bar{\gamma}_c, \\ \hat{s}^{(2)}_{soft}(\bar{\gamma}) & \text{if } \bar{\gamma} > \bar{\gamma}_c \text{ and } s^{(2)} > 0. \end{cases} \tag{A.25}$$

In this case

$$\dot{s}^{(1)} = \frac{\partial \hat{s}^{(1)}}{\partial \bar{\gamma}}\, \dot{\bar{\gamma}} = \frac{1}{\bar{\gamma}}\, \frac{\partial \hat{s}^{(1)}}{\partial \bar{\gamma}} \left(\gamma^{(1)} \nu^{(1)} + \alpha \gamma^{(2)} \nu^{(2)} \right), \tag{A.26}$$

$$\dot{s}^{(2)} = \frac{\partial \hat{s}^{(2)}}{\partial \bar{\gamma}}\, \dot{\bar{\gamma}} = \frac{1}{\bar{\gamma}}\, \frac{\partial \hat{s}^{(2)}}{\partial \bar{\gamma}} \left(\gamma^{(1)} \nu^{(1)} + \alpha \gamma^{(2)} \nu^{(2)} \right), \tag{A.27}$$

so that

$$h^{(11)} = \frac{\gamma^{(1)}}{\bar{\gamma}} \frac{\partial \hat{s}^{(1)}}{\partial \bar{\gamma}}, \quad h^{(12)} = \frac{\alpha\gamma^{(2)}}{\bar{\gamma}} \frac{\partial \hat{s}^{(1)}}{\partial \bar{\gamma}}, \quad h^{(21)} = \frac{\gamma^{(1)}}{\bar{\gamma}} \frac{\partial \hat{s}^{(2)}}{\partial \bar{\gamma}}, \quad h^{(22)} = \frac{\alpha\gamma^{(2)}}{\bar{\gamma}} \frac{\partial \hat{s}^{(2)}}{\partial \bar{\gamma}}. \tag{A.28}$$

A.2.2 Summary of time-integration procedure

Let $\{\hat{\mathbf{e}}_1(0), \hat{\mathbf{e}}_2(0), \hat{\mathbf{e}}_3(0)\}$ be an orthonormal triad, with $\hat{\mathbf{e}}_1(0) = \mathbf{n}$ aligned with the normal to the interface in the reference configuration, and $\{\hat{\mathbf{e}}_2(0), \hat{\mathbf{e}}_3(0)\}$ be in the tangent plane at the point of the interface under consideration. Let $\{\hat{\mathbf{e}}_1(t), \hat{\mathbf{e}}_2(t), \hat{\mathbf{e}}_3(t)\}$ be the same basis in the current configuration, with $\mathbf{e}_i(t) = \mathbf{R}(t)\mathbf{e}_i(0)$, where $\mathbf{R}(t)$ is the rotation that determines $\mathbf{e}_i(t)$. Then, the traction and the total relative displacement

$$\mathbf{t}(t) = \sum_i t_i(t)\hat{\mathbf{e}}_i(0), \quad \boldsymbol{\delta}(t) = \sum_i \delta_i(t)\hat{\mathbf{e}}_i(0), \tag{A.29}$$

may be transformed into the current configuration as

$$\tilde{\mathbf{t}}(t) = \mathbf{R}(t)\mathbf{t}(t) = \sum_i t_i(t)\hat{\mathbf{e}}_i(t), \tag{A.30}$$

$$\tilde{\boldsymbol{\delta}}(t) = \mathbf{R}(t)\boldsymbol{\delta}(t) = \sum_i \delta_i(t)\hat{\mathbf{e}}_i(t), \tag{A.31}$$

We consider that we are given

1. $\tilde{\mathbf{t}}(t) = t_1(t)\hat{\mathbf{e}}_1(t) + t_2(t)\hat{\mathbf{e}}_2(t) + t_2(t)\hat{\mathbf{e}}_3(t)$,
2. $s^{(i)}(t)$,
3. $\gamma^{(1)}(t)$, $\gamma^{(2)}(t)$
4. $\Delta\tilde{\boldsymbol{\delta}} = \Delta\delta_1\hat{\mathbf{e}}_1(t) + \Delta\delta_2\hat{\mathbf{e}}_2(t) + \Delta\delta_3\hat{\mathbf{e}}_3(t)$,
5. $\Delta t = \tau - t$, and
6. $\mathbf{R}(t)$ which determines $\hat{\mathbf{e}}_i(t) = \mathbf{R}(t)\hat{\mathbf{e}}_i(0)$.

We need to calculate $\left\{\mathbf{t}(\tau), s^{(i)}(\tau), \gamma^{(1)}(\tau), \gamma^{(2)}(\tau), \right\}$, and march forward in time.

Step 1. Calculate the trial stress at the end of the step

$$t_1^*(\tau) = t_1(t) + K_N \Delta\delta_1 \tag{A.32}$$

$$t_2^*(\tau) = t_2(t) + K_T \Delta\delta_2 \tag{A.33}$$

$$t_3^*(\tau) = t_3(t) + K_T \Delta\delta_3 \tag{A.34}$$

$$\tilde{\mathbf{t}}_T^*(\tau) = t_2^*(\tau)\hat{\mathbf{e}}_2(t) + t_3^*(\tau)\hat{\mathbf{e}}_3(t) \tag{A.35}$$

$$\bar{\tau}^*(\tau) = \sqrt{\tilde{\mathbf{t}}_T^*(\tau) \cdot \tilde{\mathbf{t}}_T^*(\tau)} = \sqrt{(t_2^*(\tau))^2 + (t_3^*(\tau))^2} \tag{A.36}$$

Step 2. Calculate $b^{(i)}$

$$b^{(1)} = \left\{ t_1^*(\tau) - s^{(1)}(t) \right\} \tag{A.37}$$

$$b^{(2)} = \left(\bar{\tau}^*(\tau) + \mu t_1^*(\tau) - s^{(2)}(t) \right) \tag{A.38}$$

Step 3. Calculate $A^{(ij)}$

$$A^{(11)} = \left[K_N + h^{(11)}(t) \right] > 0 \tag{A.39}$$

$$A^{(12)} = \left[h^{(12)}(t) \right] \tag{A.40}$$

$$A^{(21)} = \left[K_N \mu + h^{(21)}(t) \right] \tag{A.41}$$

$$A^{(22)} = \left[K_T + h^{(22)}(t) \right] > 0 \tag{A.42}$$

Step 4. Calculate the plastic relative displacement increments

(a) If $b^{(1)} > 0$ and $b^{(2)} \leq 0$ then

$$x^{(1)} = \frac{b^{(1)}}{A^{(11)}} \tag{A.43}$$

$$x^{(2)} = 0 \tag{A.44}$$

(b) If $b^{(1)} \leq 0$ and $b^{(2)} > 0$ then

$$x^{(1)} = 0 \tag{A.45}$$

$$x^{(2)} = \frac{b^{(2)}}{A^{(22)}} \tag{A.46}$$

(c) If $b^{(1)} > 0$ and $b^{(2)} > 0$ then first calculate A^{-1}; recall that we have assumed that the matrix A is invertible. Then solve for the plastic strain increments

$$x^{(i)} = \sum_j (A^{-1})^{(ij)} b^{(j)} \tag{A.47}$$

Check if $x^{(i)} > 0$ then accept this solution. However, if $x^{(1)} > 0$ and $x^{(2)} < 0$ then

$$x^{(1)} = \frac{b^{(1)}}{A^{(11)}}, \qquad x^{(2)} = 0, \tag{A.48}$$

or if $x^{(2)} > 0$ and $x^{(1)} < 0$ then

$$x^{(2)} = \frac{b^{(2)}}{A^{(22)}}, \qquad x^{(1)} = 0. \tag{A.49}$$

Step 5. Update the traction

$$t_1(\tau) = t_1^*(\tau) - K_N \, x^{(1)} \tag{A.50}$$

$$\bar{\tau}(\tau) = \bar{\tau}^*(\tau) - K_T \, x^{(2)} \tag{A.51}$$

$$\tilde{\mathbf{t}}_T(\tau) = \frac{\bar{\tau}(\tau)}{\bar{\tau}^*(\tau)} \, \tilde{\mathbf{t}}_T^*(\tau) = \frac{\bar{\tau}(\tau)}{\bar{\tau}^*(\tau)} \, \{t_2^*(\tau)\hat{\mathbf{e}}_2(t) + t_3^*(\tau)\hat{\mathbf{e}}_3(t)\} \tag{A.52}$$

$$t_2(\tau) = \frac{\bar{\tau}(\tau)}{\bar{\tau}^*(\tau)} \, t_2^*(\tau) \tag{A.53}$$

$$t_3(\tau) = \frac{\bar{\tau}(\tau)}{\bar{\tau}^*(\tau)} \, t_3^*(\tau) \tag{A.54}$$

$$\tilde{\mathbf{t}}(\tau) = t_1(\tau)\hat{\mathbf{e}}_1(t) + t_2(\tau)\hat{\mathbf{e}}_2(t) + t_3(\tau)\hat{\mathbf{e}}_3(t) \tag{A.55}$$

$$\mathbf{t}(\tau) = \mathbf{R}(t)^\top \, \tilde{\mathbf{t}}(\tau) = t_1(\tau)\hat{\mathbf{e}}_1(0) + t_2(\tau)\hat{\mathbf{e}}_2(0) + t_3(\tau)\hat{\mathbf{e}}_3(0) \tag{A.56}$$

Step 6. Update the state variables

$$s^{(1)}(\tau) = s^{(1)}(t) + h^{(11)}(t)x^{(1)} + h^{(12)}(t)x^{(2)} \tag{A.57}$$

$$s^{(2)}(\tau) = s^{(2)}(t) + h^{(21)}(t)x^{(1)} + h^{(22)}(t)x^{(2)} \tag{A.58}$$

Step 7. Update $\gamma^{(1)}$ and $\gamma^{(2)}$:

$$\gamma^{(1)}(\tau) = \gamma^{(1)}(t) + x^{(1)} \tag{A.59}$$

$$\gamma^{(2)}(\tau) = \gamma^{(2)}(t) + x^{(2)} \tag{A.60}$$

The model, using this time-integration, has been implemented in the finite element program ABAQUS/Explicit (2004) by writing a user-interface subroutine.

A.3 Application to adhesively-bonded components

In this section we consider the application of our model to predict the deformation and failure response of adhesively-bonded components. In particular, we shall consider components made from the aluminum alloy 6061-T6, bonded by the ductile polymeric adhesive Hysol EA 9361.[4]

The aluminum alloy was modeled as a rate-independent isotropic elastic-plastic material using the classical J_2-flow theory of the plasticity. A Young's modulus of 62.50 GPa, a Poisson's ratio of 0.33, an initial yield strength of 300 MPa, were used, and the strain-hardening characteristics of the aluminum were extracted from an experimentally-measured stress-strain curve shown in Fig. A-3.

To calibrate the interface model we have conducted three sets of experiments to measure the normal and tangential response of an Al/Hysol/Al interface: (a) Direct tension experiments on butt-jointed specimens to calibrate the tension response. (b) Double-shear experiments on double-lap specimens to calibrate the shear response,

[4]Surfaces of the components to be bonded were first roughened with medium-grit emery paper, degreased with acetone, and thoroughly cleaned in alcohol, as recommended by the adhesive manufacturer. The interface between the adhesively-bonded components was controlled to a nominal thickness of 100 μm by inserting a wire of this diameter between the adherends while preparing the bond.

and (c) Peel experiments to estimate the strain-softening response of the interface (more on this below).

Fig. A-4(a) and (c) show schematics of the direct tension and the double-lap shear specimens used to measure the normal and shear response, respectively. A non-contacting optical extensometer system was used to measure the relative opening and sliding displacements in the two experiments.[5] Fig. A-4(b) shows the traction-separation curve for the interface in the normal direction. The result shows the interface failed at a total relative normal separation of $\approx 22\,\mu m$ when the stress reaches a peak value of $\approx 24\,\mathrm{MPa}$. Fig. A-4(d) shows the the traction-separation curve for the interface in shear; the maximum shear stress is $\approx 20 MPa$, and the total relative shear displacement at failure is $\approx 44\ \mu m$, twice that of the tensile response. Note that shear response shows significant "strain-hardening" prior to failure.

Referring back to equations (A.24) and (A.25), the experimental results for the *hardening portion* of the traction-separation curves were fit to the following special form of the evolution for the two resistances $s^{(i)}$:

$$\dot{s}^{(i)}_{hard} = h_0 \left\{ 1 - \frac{s^{(i)}}{s^{*(i)}} \right\}^{a^{(i)}} \dot{\bar{\gamma}}, \quad \text{with initial values} \quad s^{(i)}(0) = s^{(i)}_0, \quad \text{for} \quad \bar{\gamma} \leq \bar{\gamma}_c, \tag{A.61}$$

with $s^{*(i)} \geq s^{(i)}$. Recall that we have defined the *equivalent relative plastic displacement* by

$$\bar{\gamma} = \sqrt{(\gamma^{(1)})^2 + \alpha\,(\gamma^{(2)})^2}.$$

We choose a value for the coupling parameter α by *assuming* that $\bar{\gamma}$ has the same critical value $\bar{\gamma}_c$ when the interface starts to soften in any combination of tension or shear. Thus, choosing the tension value as reference, that is $\bar{\gamma}_c = \gamma^{(1)}_c = 22\mu\mathrm{m}$, and

[5]Before an experiment, two reference points are marked on either side of the interface on the surfaces of the aluminum plates. A CCD camera takes pictures of the region of the specimen surface which includes the reference points during the experiment at an appropriate frequency, and the images are transferred to a personal computer through an image-acquisition board. The digital image files are then processed numerically to measure the relative positions of the two marks on either side of the interface. The optical extensometer system that we have used has a sub-micron resolution.

noting that $\gamma_c^{(2)} = 44\mu$m, we obtain

$$\alpha = 0.25,$$

for the Al/Hysol/Al interface. The numerical fit to the "hardening" portion of the experimental traction-separation curves for pure tension and shear is also shown in Fig. A-4(b) and Fig. A-4(d), respectively. The interface elastic stiffnesses used in the fit are

$$K_N = 18.9\,\text{GPa/mm}, \qquad K_T = 7.1\,\text{GPa/mm}$$

and the inelastic parameters for the interface used in the fit are listed in Table A-1.

	s_0 (MPa)	h_0 (MPa/mm)	s^* (MPa)	a	$\bar{\gamma}_c$ (μm)	h_{soft} MPa/mm	$\bar{\gamma}_{fail}$ (μm)
Tension	20.0	10000	25.0	1.6	22	2400	32
Shear	1.00	1700	24.0	1.0	22	2000	32

Table A-1: Parameters for inelastic response of interface.

The interface softening response beyond the peak stresses is not measurable in the direct tension and shear experiments described above, because the large amount of elastic energy stored in the aluminum plates causes an unloading instability which masks the true constitutive response of the interface during softening. In our numerical simulations we allow for a softening branch to the interface traction-separation response, by *assuming* a simple linear softening from $\bar{\gamma}_c$ to a failure value $\bar{\gamma}_{fail}$:

$$\dot{s}_{soft}^{(i)} = -h_{soft}^{(i)}\dot{\bar{\gamma}} \quad \text{for} \quad \bar{\gamma}_c < \bar{\gamma} \leq \bar{\gamma}_{fail}. \tag{A.62}$$

The values of $h_{soft}^{(i)}$ and $\bar{\gamma}_{fail}$ were *estimated* from a set of peeling experiments in which, because the adherends are thin sheets, the load-displacement curves show a gradually softening response before failure. The geometry for the L-peel specimens used in our study is shown in Fig. A-5(a). The specimen was made from a 1.59 mm (1/16 inch) thick Al 6061-T6 sheet adhered to an Al 6061-T6 block. The experiments were

carried out under displacement control at a cross-head-displacement rate of 4×10^{-3} mm/sec.

The geometry of the L-peel specimens was modelled using 1250 ABAQUS CPE4R elements for the thin sheet part interacting with a rigid surface. The constitutive response for the sheets was specified using the implementation of isotropic J_2-flow theory in ABAQUS/Explicit and the material parameters for Al6061-T6. The hardening parameters for the interface model listed in Table 1 were used in the simulations, and the softening parameters $h^{(i)}_{soft}$ were *adjusted* in the simulations to obtain a reasonable match with the measured load-displacement curve for the L-peel experiment. The best-fit values for $h^{(i)}_{soft}$ and $\bar{\gamma}_{fail}$ so obtained are also listed in Table 1, and the corresponding softening portions of the traction-separation curves are shown in Fig. A-4(b) and Fig. A-4(d), respectively. Fig. A-5(b) and Fig. A-5(c) compare the numerically-calculated (outline only) and experimentally-observed deformation of the L-peel specimen. A comparison between the experimentally-measured load-displacement curves and those from the simulations using the parameters listed in Table 1 is shown in Fig. A-5(d). As is clear from this figure, the numerical calculations accurately reproduce all the major features of the experimentally-measured load-displacement curve, and also capture all the major features of the macroscopic deformed shape including the large plastic strains of the aluminum sheets.

With the material parameters for the Al/Hysol/Al interface and the aluminum plates calibrated, in the sections below we check the capability of our model to predict the deformation and fracture response of adhesively-bonded components in three other important configurations. In these simulations we shall use the material parameters obtained from the calibration experiments described above.

A.3.1 T-peel test

T-peeling tests was carried out to further investigate the predictive capability of the interface constitutive model. The geometry for the symmetrical T-peel test is shown in Fig. A-6(a). T-peel specimens were made with two different thicknesses of the adherend Al 6061-T6 sheets, 1.59 mm (1/16 inch) and 0.80 mm(1/32 inch), respectively. The two different sheet thicknesses were chosen to investigate the effects

of different amounts of plastic deformation in the adherends on the macroscopic load-displacement curves. The experiments were carried out under displacement control at a cross-head-displacement rate of 4×10^{-3} mm/sec.

The geometry of the adherends was modeled using 2500 ABAQUS CPE4R elements. Fig. A-6(b) and Fig. A-6(c) compare the numerically-predicted (outline only) and experimentally-observed deformation of the specimens made from the 1.59 mm-thick sheets. The numerical calculations capture all the major major features of the macroscopic deformation, including the large plastic strains of the adherends. A comparison between the experimentally measured load-displacement curves and those predicted from the simulations is shown in Fig. A-6(d). As is clear from this figure, the numerical predictions accurately reproduce all the major features of the experimentally-measured load-displacement curves, and also quantitatively capture the effects of adherend thickness on the peel forces.

A.3.2 Edge-notch four-point bending specimens

As shown in Fig. A-7a, three plates of Al 6061-T6, one of which was nominally 350 mm long and the other two 175 mm long, and each of 50 mm width and 5 mm thickness, were adhesively bonded,[6] to produce a specimen with an "edge-notch" of width 100 μm and depth 5 mm.[7] Such specimens were tested in a four-point bend configuration at a constant displacement rate of 4×10^{-3} mm/sec. Because of the symmetry of the problem, one-half of the geometry was meshed using 1250 ABAQUS CPE4R elements.

Fig. A-7(b) shows a photograph of the experiment after debonding has occurred in the specimen, while Fig. A-7(c) shows a magnified image (2X) of the deformed finite element mesh in a region near the debond. The load vs displacement curves from two nominally identical experiments are shown in Fig. A-7(d). Initially, the system behaves linearly, then nonlinearity associated with the *plastic deformation of the aluminum plates sets in*, and finally debonding of the interface occurs at a load of $\approx$

[6]The interface was prepared in a manner identical to that used in the calibration experiments described in the previous section.

[7]Specimens of this type, but of much smaller dimensions, are widely used to test the adhesion and debonding of thin-film structures, c.f., e.g., Duskardt et al. (1998, 2000).

3.2KN; the load plateau is associated with a stable propagation of the debonding along the interface. Fig. A-7(d) also shows that the corresponding numerically-predicted load-displacement curve is in good accord with the experiments.

A.3.3 Lap-shear test

The geometry for our special lap-shear test is shown in Fig. A-8(a). The geometry consists of two sheets of Al 6061-T6 adhesively-bonded to a 5 mm thick 25.4 mm square piece of the same aluminum alloy, to produce two interfaces. The specimens were made with two different thicknesses of the Al 6061-T6 sheets, 1.59 mm (1/16 inch) and 0.80 mm(1/32 inch), to investigate the effects of different amounts of plastic deformation in the sheets on the macroscopic load displacement curves. As the figure shows, there is an offset between the loading axes of the two sheets; this offset will generate a moment which will rotate the middle block, and this rotation will cause the interface to separate in a combined tension and shear mode. The experiments were carried out under displacement control at a cross-head-displacement rate of 10^{-3} mm/sec.

The geometry of the adherends was modelled using 2250 ABAQUS CPE4R elements. Fig. A-8(b) and Fig. A-8(c) compare the numerically-predicted (outline only) and experimentally-observed deformation of the specimens made from the 1.59 mm thick sheets. The numerical calculations capture all the major features of the macroscopic deformation, including the large plastic strains of the adherends and the accompanying rotations.[8] A comparison between the experimentally-measured load-displacement curves and those predicted from the simulations is shown in Fig. A-8(d). The numerical predictions accurately reproduce all the major features of the experimentally measured load-displacement curves, and also quantitatively capture the effects of the thickness of the aluminum sheets on the macroscopic force displacement curves.

[8]Ideally, the two interfaces on either side of the middle block will have identical properties and will be identically loaded because of geometrical symmetry, so that they should fail in a similar fashion during the test, which is what actually happens in the numerical simulation. However, in the actual experiment, because of various possible minor variations, one interface always starts to fail earlier than the other.

A.4 Concluding Remarks

We have developed a continuum-level phenomenological interface constitutive model which accounts for both reversible elastic, as well irreversible inelastic separation-sliding deformations at the interface prior to failure. We have implemented our constitutive model in the finite-element computer program ABAQUS/Explicit (2004) by writing a user interface subroutine.

We have applied the model and the numerical capability to predict the failure response of adhesively-bonded components made from the aluminum alloy 6061-T6 bonded by the ductile polymeric adhesive Hysol EA 9361. We have shown that our new model, when suitably calibrated against a set of experiments to determine the constitutive parameters, is able to reasonably well predict the macroscopic deformed geometries and the load-displacement curves in (a) T-peel experiments, (b) four-point bend experiments on bonded bi-layer edge-notch specimens; and (c) lap-shear experiments.

The constitutive model and the computational procedures presented here provide a new capability for the simulation and design of structures with bonded components which may be undergoing large inelastic deformations in both the adherents and the adhesives.

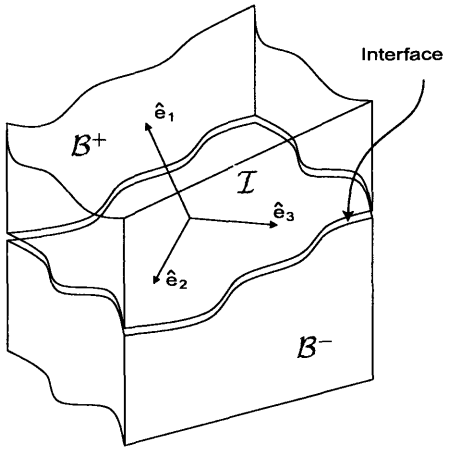

Figure A-1: Schematic of interface between two bodies $\mathcal{B}^+$ and $\mathcal{B}^-$.

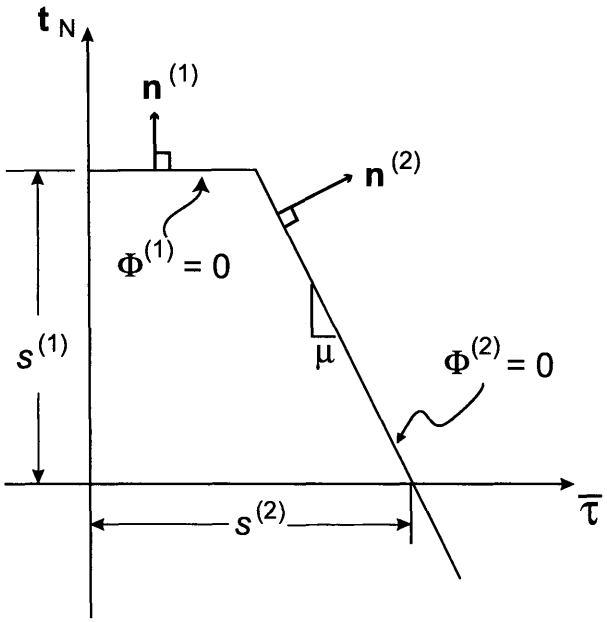

Figure A-2: Schematic of yield surfaces for the normal and shear mechanisms.

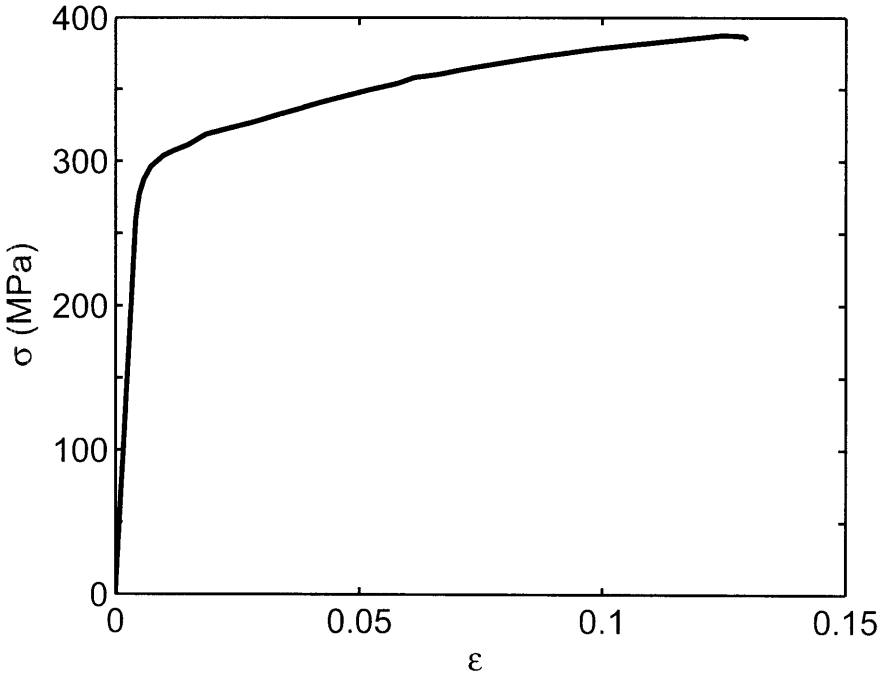

Figure A-3: True stress-strain curve for aluminum alloy 6061-T6.

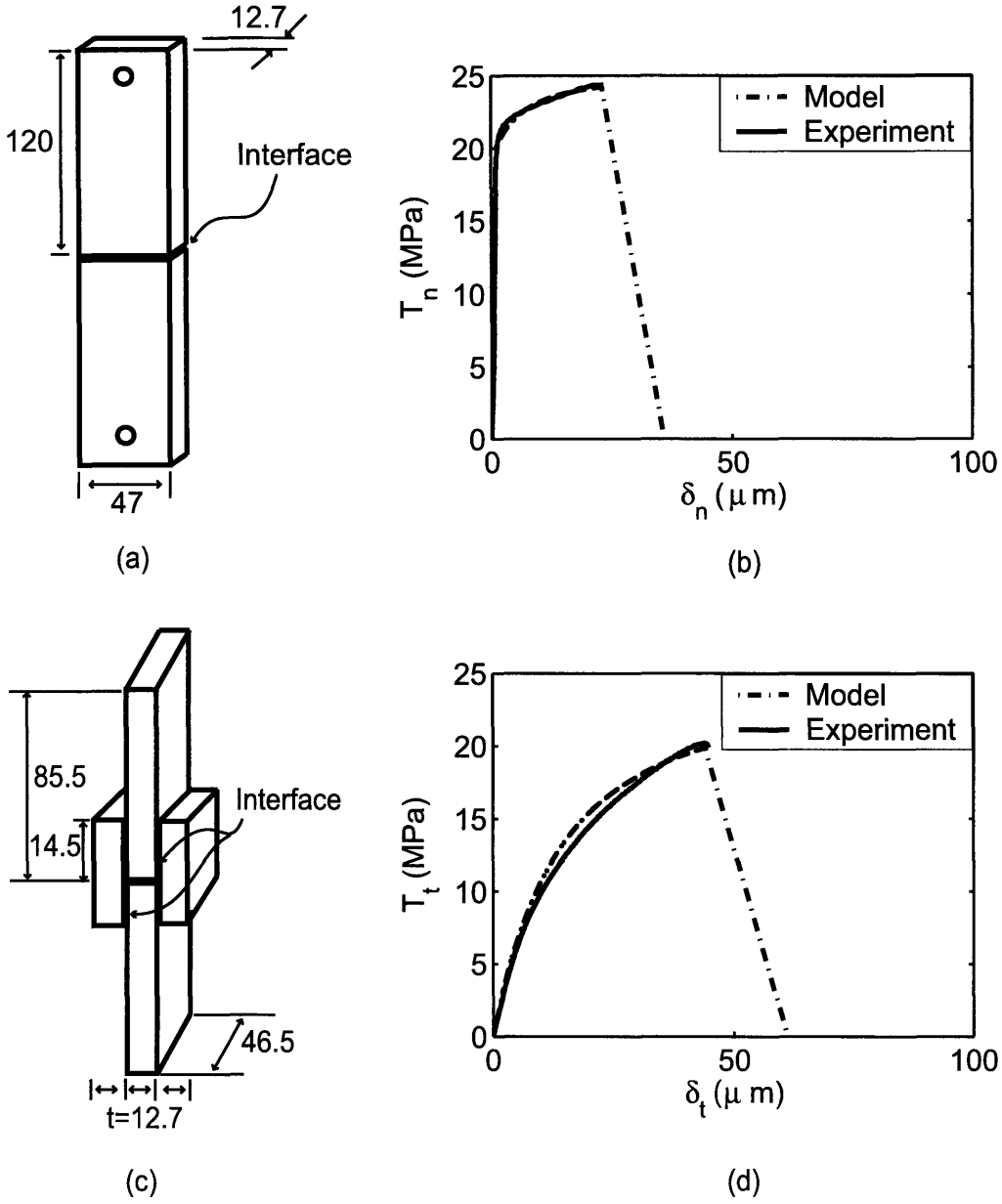

Figure A-4: Calibration of Al/Hysol/Al interface response. (a): Geometry of the specimen used for measuring the traction-separation response in the direction normal to the interface; all dimensions are in mm. (b): Traction-separation curve in the normal direction from experiment, as well as the curve-fit used in subsequent simulations. (c): Geometry of the specimen used for measuring the interface traction-separation response in shear; all dimensions are in mm. (d): Traction-separation curve in the shear direction from the experiment, as well as the curve-fit used in subsequent simulations.

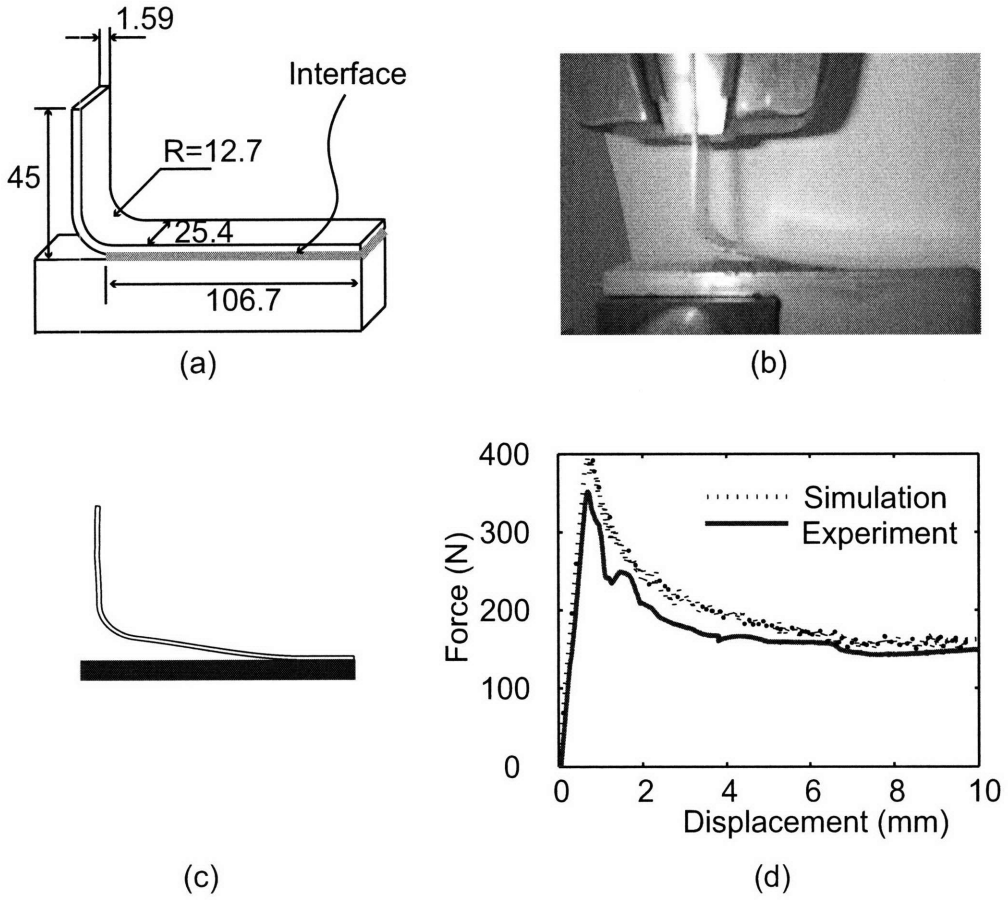

Figure A-5: L-peel experiments: (a): Geometry of the specimen; all dimensions are in mm. (b): Photograph of a deformed specimen in an experiment. (c): Deformed mesh in a corresponding numerical simulation (outline only). (d): Force versus displacement curves from the experiments conducted at a constant displacement rate of 4×10^{-3} mm/sec, compared with the corresponding result from the numerical simulation.

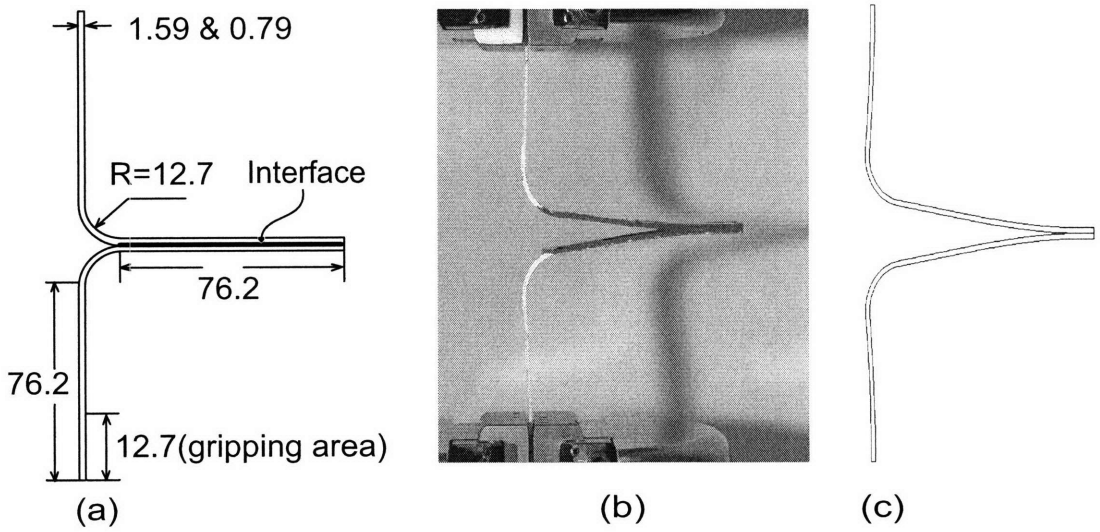

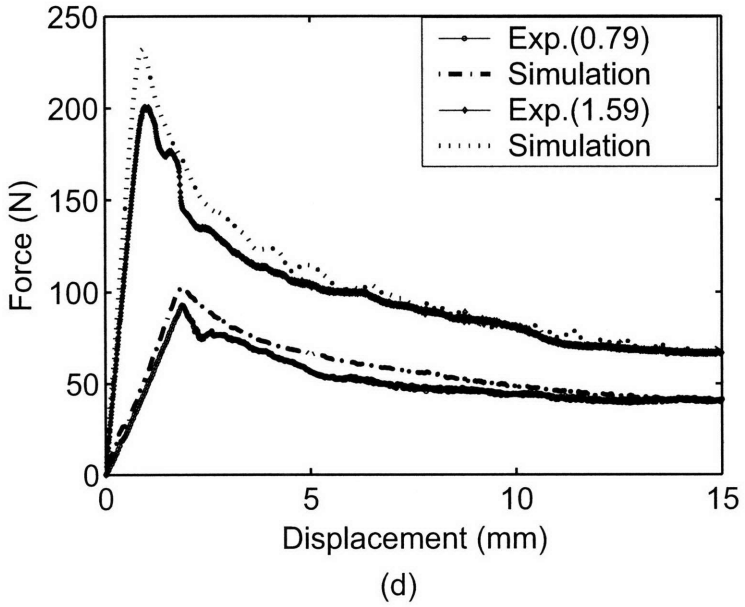

Figure A-6: T-peel experiments: (a): Geometry of the specimen; all dimensions are in mm. (b): Photograph of a deformed specimen in an experiment. (c): Deformed mesh in a corresponding numerical simulation (outline only). (d): Force versus displacement curves from the experiments conducted at a constant displacement rate of 4×10^{-3} mm/sec, compared with the corresponding result from the numerical simulation for sheet thicknesses of 1.59 mm and 0.79 mm.

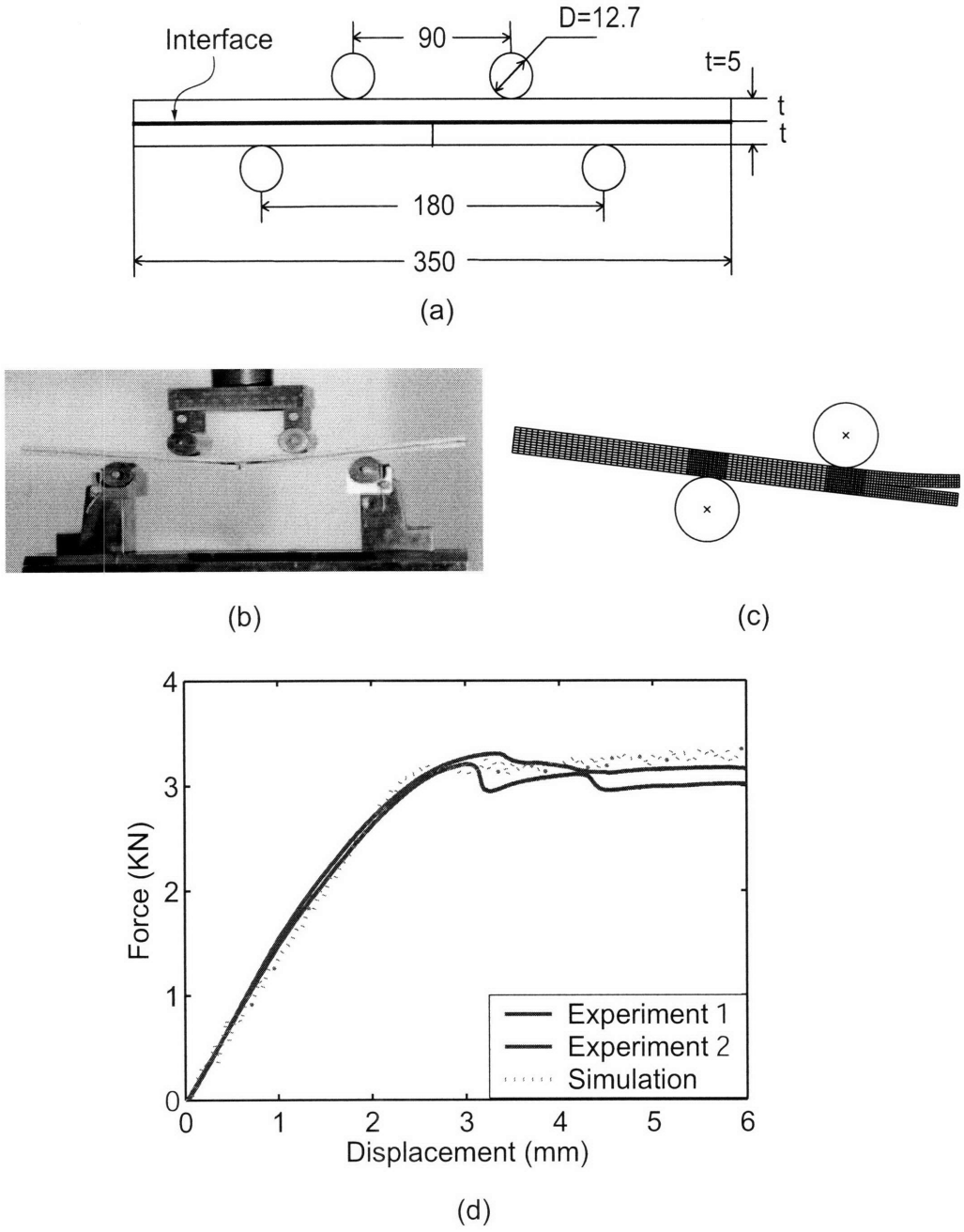

Figure A-7: Four-point bend experiments on bonded bi-layer edge-notch specimens: (a): Geometry of the specimen and the four-point bend configuration; all dimensions are in mm. (b): Photograph of a deformed specimen in an experiment. (c): Deformed mesh in a corresponding numerical simulation (magnified 2). (d): Force versus displacement curves from the experiments conducted at a constant displacement rate of 4×10^{-3} mm/sec, compared with the corresponding result from the numerical simulation.

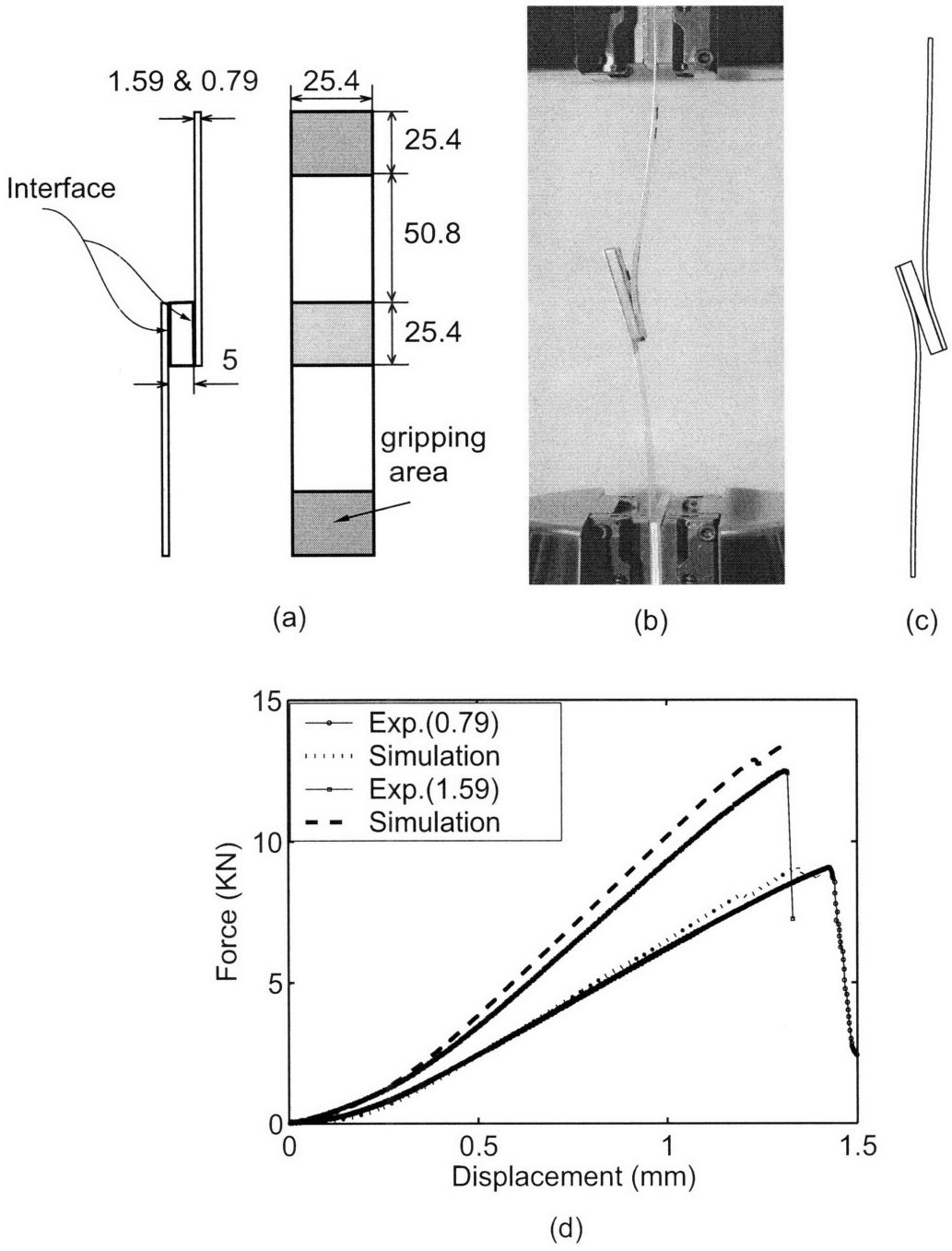

Figure A-8: Lap-shear experiments: (a): Geometry of the specimen; all dimensions are in mm. (b): Photograph of a deformed specimen in an experiment. (c): Deformed mesh in a corresponding numerical simulation (outline only). (d): Force versus displacement curves from the experiments conducted at a constant displacement rate of 10^{-3} mm/sec, compared with the corresponding result from the numerical simulation for sheet thicknesses of 0.80 mm and 1.59 mm.

Bibliography

ABAQUS, *Reference manuals*, Hibbit, Karlsson & Sorenson, Inc., Pawtucket, R.I., 2003.

Anand, L., On H. Hencky's approximate strain-energy function for moderate deformations, *ASME Journal of Applied Mechanics* **46** (1979) 78-82.

Anand, L., Plane deformations of ideal granular materials, *Journal of the Mechanics and Physics of Solids* **31** (1983) 105-122.

Anand L, Kalidindi SR. Mechanics of Materials 1994;17:223.

Anand, L., and Gu, C., Granular materials: constitutive equations and strain localization, *Journal of the Mechanics and Physics of Solids* **48** (2000) 1701-1733.

Anand, L., and Gurtin, M.E., A theory of amorphous solids undergoing large deformations, with applications to polymeric glasses, *International Journal of Solids and Structures*, **40** (2003) 1465-1487.

Anand, L., and Spitzig, W. A., Shear band orientations in plane strain, *Acta metallurgica*, **30**(1982) 553-561.

Anand, L., and Su, C., A theory for amorphous viscoplastic materials undergoing finite deformations, with application to metallic glasses, *Journal of the Mechanics and Physics of Solids*, **53** (2005) 1362.

Antoniou, A, Bastwros, AF, Lo, CCH, Biner, SB. Materials Science and Engineering A 2005;394:96.

Argon, A. S., Plastic deformation in metallic glasses, *Acta Metallurgica* **27** (1979) 47-58.

Argon, A. S., Inelastic deformation and fracture of glassy solids, *Materials Science and Technology* **6** (1993) 461-508.

Argon, A. S., Meguasar, J., and Grant, N. J., Shear band induced dilations in metallic glasses, *Scripta Metallurgica* **19** (1985) 591-596.

Barenblatt, G. I., The formation of equilibrium cracks during brittle fracture: general ideas and hypotheses, axially symmetric cracks,*Applied Mathematics and Mechanics (PMM)* **23** (1959) 622-636.

Bletry M, Guyot, P, Blandin, JJ, Soubeyroux, JL. Acta Materialia 2006;54:1257.

Bruck, H. A., Christman, T., Rosakis, A. J., and Johnson, W. L., Quasi-static constitutive behavior of $Zr_{41.25}Ti_{13.75}Ni_{10}Cu_{12.5}Be_{22.5}$ bulk amorphous alloys, *Scripta Materialia* **30** (1993) 429-434.

Cahn, R. W., Pratten, N. A., Scott, M. G., Sinning, H. R., and Leonardsson, Studies of relaxation of metallic glasses by dilatometry and density measurements, *Materials Research Society Symposium Proceedings* **28** (1984) 241-252.

Cohen MH, Turnbull D. J Chem Phys 1959;31:1164.

Coulomb, C. A., "In Mémories de Mathématique et de Physique," *Académie Royale des Sciences* **7** (1773) 343-382.

Conner, R. D., Johnson, W. L., Paton, N. E., and Nix, W. D., Shear bands and cracking of metallic glass plates in bending, *Journal of Applied Physics* **94** (2003) 904-911.

Davis LA, Chou CP, Tanner LE, Ray R. Scripta Metall 1976;10:937.

de Hey P, Sietsma J, van den Beukel A. Acta Metall 1998;46:5873.

Deng, D., and Lu, B., Density change of glassy $Pd_{77}Si_{16.5}Cu_{6.5}$ alloy during cold drawing, *Scripta Metallurgica* **17** (1983) 515-518.

Deng, D., Argon, A. S., and Yip, S., Simulation of plastic deformation in a two-dimensional atomic glass by molecular dynamics IV, *Philosophical Transactions of the Royal Society A* **329** (1989) 613-640.

Donovan, P. E., Compressive deformation of amorphous $Pd_{40}Ni_{40}Ni_{20}$, *Materials Science and Engineering* **98** (1988) 487-490.

Donovan, P. E., A yield criterion for $Pd_{40}Ni_{40}Ni_{20}$ metallic glass, *Acta Metallurgica* **37** (1989) 445-456.

Donovan, P. E., Plastic flow and fracture of $Pd_{40}Ni_{40}Ni_{20}$ metallic glass under an indentor, *Journal of Materials Science* **24** (1989) 523-535.

Dugdale, D. S., Yielding of steel sheets containing slits, *Journal of the Mechanics and Physics of Solids* **8** (1960) 100-104.

Duine PA, Sietsma J, van den Beukel A. Acta Metall Mater 1992;40:743.

Duskardt, R. H., and Lane, M. and Ma, Q and Krishna, N, Adhesion and debonding of multilayer thin-film structures, *Engineering Fracture Mechanics* **61** (1998) 141-162.

Lane, M., and Duskardt, R. H. Vainchtein, A., and Gao, H., Plasticity contributions to interface adhesion in thin-film interconnect structures, *Journal of Materials Research* **15** (2000) 2758-2769.

Ebrahami, F., Zhai, Q., and Kong, D., Deformation and Fracture of Electrodeposited Copper, *Scripta Materialia* **39** (1998) 315-321.

Ebrahami, F., Bourne, G. R., Kelly, M. S., and Matthews, T. E., Mechanical Properties of Nanocrystalline Nickel Produced by Electrodeposition, *Nanostructured Materials* **11** (1999) 343-350.

Gleiter, H., Nanocrystalline materials, *Progress in Materials Science* **33** (1989) 223-315.

Gleiter H. Acta Mater 2000;48:1.

Gouldstone A, Van Vliet KJ, Suresh S. Nature 2001;411:656.

Gurtin, M. E., A gradient theory of single-crystal viscoplasticity that accounts for geometrically necessary dislocations, *Journal of the Mechanics and Physics of Solids* **50** (2002) 5-32.

Hays, C. C., Kim, C. P., and Johnson, W. L., Microstructure controlled shear band pattern formation and enhanced plasticity in bulk metallic glasses containing *in situ* formed ductile phase dendrite disperisons, *Phyiscal Review Letters* **84** (2000) 2901-2904.

Hill, R., *The mathematical theory of plasticity*, Clarendon Press, Oxford, U.K., 1950.

Huang, R., Suo, Z., Prevost, J. H., and Nix, W. D., Inhomogeneous deformation in metallic glasses, *Journal of the Mechanics and Physics of Solids* **50** (2002) 1011-1027.

Hufnagel TC (ed.). Scripta Materialia 2006;54;317

Hutchinson, J. W. and Evans, A. G., Mechanics of materials: top-down approaches to fracture, *Acta Materialia* **48** (2000) 125-135.

Inoue, A., Stabilization of metallic supercooled liquid and bulk amorphous alloys, *Acta Materialia* **48** (2000) 279-306.

Inour, A., Kimura, H. M., and Zhang, T., High-strength aluminum- and zirconium-based alloys containing nanoquasicrystalline particles, *Materials Science & Engineering A* **294-296** (2000) 727-735.

Jana, S., Ramamurty, U., Chattopadhyay, K., and Kawamura, Y., Subsurface deformation during Vickers indentation of bulk metallic glasses, *Materials Science and Engineering A* **375-377** (2004) 1191-1195.

Ramamurty U, Jana S, Kawamura Y, Chattopadhyay K. Acta Materialia 2005;53:705

Jeong, D. H., Gonzalez, F., Palumbo, G., Aust, K. T., and Erb, U., The Effect of Grain Size on the Wear Properties of Electrodeposited Nanocrystalline Nickel Coatings, *Scripta Materialia* **44** (2001) 493-499.

Johnson, W. L., Bulk glass forming metallic alloys: science and technology, *MRS Bulletin* **24(10)** (1999) 7249-7251.

Johnson, W. L., Bulk glass forming metallic alloys: an emerging engineering materials, *Journal of Metals* **54 (3)** (2002) 40-43.

Kafkalidis, M. S. and Thouless, M. D., The effects of geometry and material properties on the fracture of single-lap-shear joints, *International Journal of Solids and Structures* **39** (2002) 4367-4383.

Kim, J. J., Choi, Y., Suresh, S., and Argon, A. S., Nanocrystallization during nanoindentation of a bulk amorphous metal alloy at room temperature, *Science* **295** (2002) 654-657.

Klement, W., Willens, R. H., and Duvez, P.,help, *Nature* **187** (1960) 869–??.

Kröner, E., Allgemeine kontinuumstheorie der versetzungen und eigenspannungen, *Archive for Rational Mechanics and Analysis* **4**(1960) 273-334.

Kumar, K. S., Suresh, S., Chisolm, M. F., Horton, J. A., and Wang, P., Deformation of electodeposited nanocrystalline nickel, *Acta Materialia* **51** (2003) 387-405.

Kumar KS, and Van Swygenhoven H, Suresh S. Acta Mater 2003;51:5743.

Lee, E. H., Elastic plastic deformation at finite strain, *ASME Journal of Applied Mechanics* **36** (1969) 1-6.

Lee, M. L., Li, Y., and Schuh, C. A. Effect of a controlled volume fraction of dendritic phases on tensile and compressive ductility in La-based metallic glass matrix composite, *Acta Materialia* **52** (2004) 4121-4131.

Legros, M., Elliot, B. R., Rittner, M. N., Weertman, J. R., and Hemker, K. J., Microsample Tensile Testing Of Nanocrystalline Metals, *Philosophical Magazine A* **80** (2000) 1017-1026.

Lewandowski, J. J., and Lowhaphandu, P., Effects of hydrostatic pressure on the flow and fracture of a bulk amorphous metal, *Philosophical Magazine A* **82** (2002) 3427-3441.

Lu, L., Sui, M. L., and Lu, K., Superplastic Extensibility of Nanocrystalline Copper at Room Temperature, *Science* **287** (2000) 1463-1466.

Lu, L., Li, S. X., and Lu, K., An Abnormal Strain Rate Effect on Tensile Behavior in Nanocrystalline Copper, *Scripta Materialia* **45** (2001) 1163-1169.

Lu, J., Ravichandran, G., Johnson, W. L., Deformation behavior of the $Zr_{41.2}Ti_{13.8}Cu_{12.5}Ni_{10}Be_{22.5}$ bulk metallic glass over a wide range of strain-rates and temperatures, *Acta Materialia* **51** (2003) 3429-3443.

Lund, A. C., and Schuh, C. A., Yield surface of a simulated metallic glass, *Acta Materialia* **51** (2003) 5399-5411.

McFadden, S. X., Mishra, R. S., Valiev, R. Z., Zhilyaev, A. P., and Mukherjee, A. K., Low-Temperature Superplasticity in Nanostructured Nickel and Metal Alloys, *Nature* **398** (1999) 684-686.

Mehrabadi, M. M., and Cowin, S. C., Initial planar deformation of dilatant granular materials, *Journal of the Mechanics and Physics of Solids* **26** (1978) 269-284.

Mohr, O., Welche umstände bedingen die elastizitätsgrenze und den brusch eines materials, *Zeitschrift des Vereines Deutscher Ingenieure* **44** (1900) 1524-1530.

Mukai, T., Nieh, T. G., Kawamura, Y, Inoue, A., and Higashi, K., Dynamic response of a $Pd_{40}Ni_{40}P_{20}$ bulk metallic glass, *Scripta Materialia* **46** (2002) 43-47.

Needleman, A., An analysis of decohesion along an imperfect interface, *International Journal of Fracture* **40** (1990) 21-40.

Nemat-Nasser, S., Mehrabadi, M. M., and Iwakuma, T., On certain macroscopic and microscopic aspects of plastic flow of ductile materials. In Nemat-Nasser, S. (ed.) *Three-dimensional constitutive relations and ductile fracture*, North-Holland, Amsterdam, (1981) 157-172.

Nieman, G. W., Weertman, J. R., and Siegel, R. W., Mechanical Behavior of Nanocrystalline Cu and Pd, *Journal of Materials Research* **6** (1991) 1012-1027.

Camacho, G. T. and Ortiz, M., Computational modeling of impact damage in brittle materials, *International Journal of Solids and Structures* **33** (1996) 2899-2938.

Ranganathan S, Divakar R, Raguṇathan VS. Scripta Mater 2001;44:1169.

Rudnicki, J. W., and Rice, J. R., Conditions for the localization of deformation in pressure sensitive dilatant materials, *Journal of The Mechanics and Physics of Solids*, **23** (1975) 371 – 394.

Sanders, P. G., Eastman, J. A., and Weertman, J. R., Elastic and Tensile Behavior of Nanocrystalline Copper and Palladium, *Acta Materialia* **45** (1997) 4019-4025.

Sansoz F, Molinari JF. Scripta Mater 2004;50:1283.

Saotome Y, Noguchi Y, Zhang T, Inoue A. Materials Science and Engineering A 2004;375-377:389.

Schroers, J. Journal of Metals 2005;May:35.

Schuh, C. A., and Nieh, T. G., A survey of instrumented indentation studies on metallic glasses, *Journal of Materials Research*, **19** (2004) 46-57.

Schuh, C., Nieh, T. G., and Yamasaki, T., Hall-Petch Breakdown Manifested in Abrasive Wear Resistance of Nanocrystalline Nickel, *Scripta Materialia* **46** (2002) 735-740.

Spaepen, F., A microscopic mechanism for steady state inhomogeneous flow in metallic glasses. *Acta Metallurgica* **25** (1977) 407-415.

Spencer, A. J. M., A theory of the kinematics of ideal soils under plane strain conditions, *Journal of the Mechanics and Physics of Solids* **12** (1964) 337-351.

Spencer, A. J. M., Deformation of ideal granular materials. In H. G. Hopkins and M. J. Sewell (eds) *Mechanics of Solids*, Pergamon Press, Oxford and New York, (1982) 607-652.

Su, C., Wei, Y. J., and Anand, L., An elastic-plastic interface constitutive model: application to adhesive joints, *International Journal of Plasticity* **20** (2004) 2063-2081.

Su, C., and Anand, L., Plane strain indentation of a Zr-based metallic glass: experiments and numerical simulation, *Acta Materialia* **54** (2006) 179-189.

Suryanarayana, C., Nanocrystalline Materials, *International Metallurgical Reviews* **40** (1995) 41-46.

Torre, F. D., Swygenhoven, H. V., and Victoria, M., Nanocrystalline electrodeposited Ni: microstructure and tensile properties, *Acta Materialia* **50** (2002) 3957-3970.

Tuinstra P, Duine PA, Sietsma J, van den Beukel A. Acta Metall Mater 1995;43:2815.

Tvergaard, V. and Hutchinson, J. W., The relation between crack growth resistance and fracture process parameters in elastic-plastic solids, *Journal of The Mechanics and Physics of Solids* **40** (1992) 1377-1397.

Tvergaard, V. and Hutchinson, J. W., Toughness of ductile adhesive joints, *Journal of The Mechanics and Physics of Solids* **44** (1996) 789-800.

Vaidyanathan, R., Dao, M., Ravichandran, G., and Suresh, S., Study of mechanical deformation in bulk metallic glass through instrumented indentation, *Acta Materialia* **49** (2001) 3781-3789.

Warner DH, Sansoz F, Molinari JF. Int J of Plasticity 2006;22:754.

Weertman JR. In: C Koch, Ed. Nanostructured Materials, Noyes, NY; 2002. p. 393.

Wei, Y.J., and Anand, L., Grain-boundary sliding and separation in polycrystalline metals: application to nanocrystalline fcc metals, *Journal of the Mechanics and Physics of Solids* **52** (2004) 2587-2616.

Wei, Y.J., Su, C., Anand, L., A computational study of the mechanical behavior of nanocrystalline fcc metals, *Acta Materialia* bf 54 (2006) 3177-3190.

Wolf D, Yamakov V, Phillpot SR, Mukherjee A, Gleiter H. Acta Mater 2005;53:1.

Xu, X. P. and Needleman, A., Numerical simulations of fast crack growth in brittle solids, *Journal of the Mechanics and Physics of Solids* **42** (1994) 1397-1434.

Yang, Q. D. and Thouless, M. D. and Ward, S. M., Numerical simulation of adhesively-bonded beams failing with extensive plastic deformation, *Journal of The Mechanics and Physics of Solids* **47** (1999) 1337-1353.

Yang, Q. D. and Thouless, M. D. and Ward, S. M., Analysis of the symmetrical 90-degree peel test with extensive plastic deformation, *Journal of Adhesion* **72** (2000) 115-132.

Yang, Q. D. and Thouless, M. D., Mixed-mode fracture analysis of plastically deforming adhesive joints, *International Journal of Fracture* **110** (2001) 175-187.

Zhang, H, Jing, X, Subhash, G, Kecskes, LJ, Dowding, RJ. Acta Materialia 2005;in press.

Zhang, Z. F., Eckert, J., and Schultz, L., Difference in compressive and tensile fracture mechanisms of $Zr_59Cu_{20}Al_{10}Ni_8Ti_3$ bulk metallic glass , *Acta Materialia* **51** (2003) 1167-1179.